AD-A153 860 ENVIRONMENTAL BACKGROUND MEASUREMENT PROGRAM(U) SCRIPPS INSTITUTION OF OCEANOGRAPHY LA JOLLA CA MARINE PHYSICAL LAB K M WATSON ET AL. 15 FEB 85 MPL-U-7/85 1/2

UNCLASSIFIED N00014-79-C-0983 F/G 8/10 NL

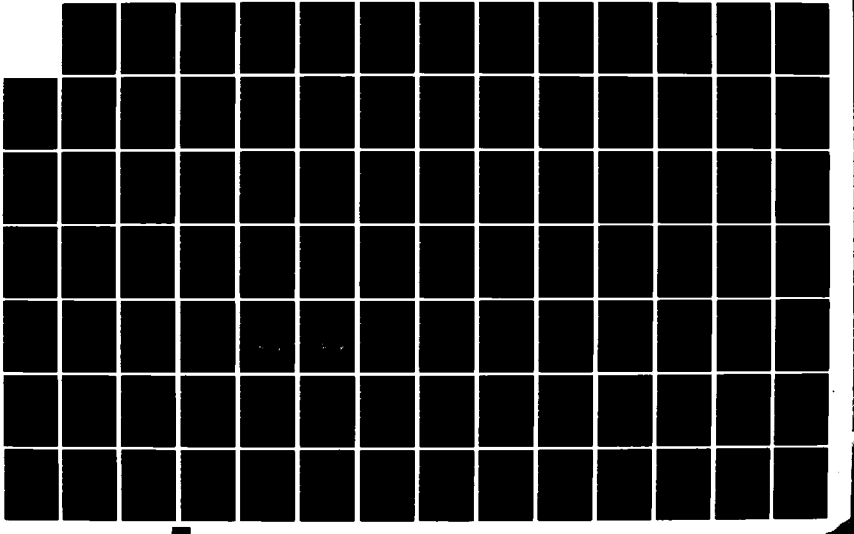

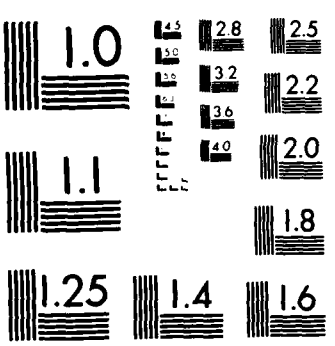

FINAL REPORT - ENVIRONMENTAL BACKGROUND MEASUREMENT PROGRAM

Principal Investigator: Kenneth M. Watson
Victor C. Anderson

Sponsored by
the Office of Naval Research
through
Naval Ocean Research & Development Activity
Code 541
Contract: N00014-79-C-0983
Total Amount of Contract: $1,014,100
Period of Award: September 15, 1979 thru September 30, 1984

Document cleared for public release; distribution unlimited.

February 15, 1985

MPL-U-7/85

MARINE PHYSICAL LABORATORY
of the Scripps Institution of Oceanography
San Diego, California 92152

SECURITY CLASSIFICATION OF THIS PAGE (When Data Entered)

REPORT DOCUMENTATION PAGE

READ INSTRUCTIONS BEFORE COMPLETING FORM

1. REPORT NUMBER: MPL-U-7/85	2. GOVT ACCESSION NO.: AD-A153860
3. RECIPIENT'S CATALOG NUMBER:	
4. TITLE (and Subtitle): FINAL REPORT - ENVIRONMENTAL BACKGROUND MEASUREMENT PROGRAM	5. TYPE OF REPORT & PERIOD COVERED: Final Report
	6. PERFORMING ORG. REPORT NUMBER: MPL-U-7/85
7. AUTHOR(s): Principal Investigators: Kenneth M. Watson, Victor C. Anderson	8. CONTRACT OR GRANT NUMBER(s): N00014-79-C-0983
9. PERFORMING ORGANIZATION NAME AND ADDRESS: University of California, San Diego, Marine Physical Laboratory of the Scripps Institution of Oceanography, San Diego, CA 92152	10. PROGRAM ELEMENT, PROJECT, TASK AREA & WORK UNIT NUMBERS:
11. CONTROLLING OFFICE NAME AND ADDRESS: Office of Naval Research, Department of the Navy, 800 North Quincy Street, Arlington, Virginia 22209	12. REPORT DATE: 1985
	13. NUMBER OF PAGES:
14. MONITORING AGENCY NAME & ADDRESS(if different from Controlling Office):	15. SECURITY CLASS. (of this report): Unclassified
	15a. DECLASSIFICATION/DOWNGRADING SCHEDULE:

16. DISTRIBUTION STATEMENT (of this Report)

Document cleared for public release; distribution unlimited.

17. DISTRIBUTION STATEMENT (of the abstract entered in Block 20, if different from Report)

18. SUPPLEMENTARY NOTES

19. KEY WORDS (Continue on reverse side if necessary and identify by block number)

seafloor work vehicles, doppler sonar, upper ocean wavefield, oceanographic instrumentation

20. ABSTRACT (Continue on reverse side if necessary and identify by block number)

From 1 October 1980 through 30 September 1984 a program of data analysis and interpretation was conducted at the Marine Physical Laboratory under the sponsorship of NORDA Code 500. The focus of this effort, termed the Environmental Background Measurement Program, was on the statistics of the fine scale shear and density fields in the sea. Special effort was placed on determining the degree of predictability of these fields, the degree to which linear internal wave theory could account for them, and the degree to which existing models of the wavefield were accurate. With additional support from ONR Codes 220 and 420, significant progress was achieved on these tasks.

DD FORM 1 JAN 73 1473 EDITION OF 1 NOV 65 IS OBSOLETE

S/N 0102-LF-014-6601

SECURITY CLASSIFICATION OF THIS PAGE (When Data Entered)

Another task completed under this contract was the hardware and software design of a digital control system for a seafloor work vehicle (RUM III). The digital control system for the vehicle will be used to enhance its usefulness as an operational sea floor work vehicle. The functional requirements, design constraints, and system configuration were first examined. A detailed description of the hardware systems and their corresponding software components are described in this report.

MPL also participated in the acquisition, adaptation and installation of a side-looking sonar system for use on the Advanced Unmanned Search System (AUSS) Testbed Program being developed at the Naval Ocean Systems Center, San Diego.

In support of an ocean optics measurement project conducted by NOSC personnel aboard the research platform FLIP, MPL modified and installed two aluminum truss booms (60 ft and 75 feet) from which the oceanographic instrumentation was suspended, resulting in successful data acquisition.

Table of Contents

ABSTRACT

From 1 October 1980 through 30 September 1984 a program of data analysis and interpretation was conducted at the Marine Physical Laboratory under the sponsorship of NORDA Code 500. The focus of this effort, termed the Environmental Background Measurement Program, was on the statistics of the fine scale shear and density fields in the sea. Special effort was placed on determining the degree of predictability of these fields, the degree to which linear internal wave theory could account for them, and the degree to which existing models of the wavefield were accurate. With additional support from ONR Codes 220 and 420, significant progress was achieved on these tasks.

Another task completed under this contract was the hardware and software design of a digital control system for a seafloor work vehicle (RUM III). The digital control system for the vehicle will be used to enhance its usefulness as an operational sea floor work vehicle. The functional requirements, design constraints, and system configuration were first examined. A detailed description of the hardware systems and their corresponding software components are described in this report.

MPL also participated in the acquisition, adaptation and installation of a side-looking sonar system for use on the Advanced Unmanned Search System (AUSS) Testbed Program being developed at the Naval Ocean Systems Center, San Diego.

In support of an ocean optics measurement project conducted by NOSC personnel aboard the research platform FLIP, MPL modified and installed two aluminum truss booms (60 ft and 75 feet) from which the oceanographic instrumentation was suspended, resulting in successful data acquisition.

FINAL REPORT - ENVIRONMENTAL BACKGROUND MEASUREMENT PROGRAM

I. ENVIRONMENTAL BACKGROUND MEASUREMENT PROGRAM

Principal Investigator: Robert Pinkel
Total Amount of Award: $650,000

From 1 October 1980 through 30 September 1984 a program of data analysis and interpretation was conducted at the Marine Physical Laboratory under the sponsorship of NORDA Code 500. The focus os this effort, termed the Environmental Background Measurement Program, was on the statistics of the fine scale shear and density fields in the sea. Special effort was placed on determining the degree of predictability of these fields, the degree to which linear internal wave theory could account for them, and the degree to which existing models of the wavefield were accurate.

With additional support from ONR Codes 220 and 420, significant progress was achieved on these tasks. Four documents were produced in the course of this work which described the results. These are presented as Appendices A through D of this report. In chronological order, the first work, "Doppler Sonar Observations of Internal Waves; Wavefield Structure" (Appendix A) demonstrates the propagating nature of the upper ocean shear field. The dominant, near inertial, shears can be predicted many days in advance as they propagate vertically in the sea.

The second work, "Doppler Sonar and CTD Observations of the Interrelationship Between Large and Small Scale Internal Waves" (Appendix B), attempts to reconcile observation of horizontal vs. vertical motion. It can't be done, at small scale and high frequency, using linear internal wave theory. "Doppler Sonar Observations of Internal Waves: The Wavenumber Frequency Spectrum" (Appendix C) provides a statistical description of the velocity field, for comparison with the Garrett-Munk spectral model. The disagreements between the measurements and the model are significant. This is perhaps not surprising given that the small scale motions do not appear to be linear internal waves. The discrepancies become particularly important is one is interested in small-scale, high frequency shear. This is discussed in Appendix D, "The Wavenumber Frequency Spectrum of Upper Ocean Shear".

These four works, accomplished under the sponsorship of NORDA Code 500, present a view of the small scale shear and temperature fields which differs radically

from pre-existing concepts. It is felt that the new viewpoint is much closer to reality. Given the established Navy need for information on these scales, the Environmental Background Measurement Program must be considered a successful and cost effective effort.

APPENDIX A

Reprinted from JOURNAL OF PHYSICAL OCEANOGRAPHY, Vol. 13, No. 5, May 1983
American Meteorological Society
Printed in U. S. A.

Doppler Sonar Observations of Internal Waves: Wave-Field Structure

R. PINKEL

Doppler Sonar Observations of Internal Waves: Wave-Field Structure

R. PINKEL

Marine Physical Laboratory, Scripps Institution of Oceanography, University of California, San Diego, La Jolla, CA 92093

(Manuscript received 7 June 1982, in final form 17 January 1983)

ABSTRACT

During May of 1980 an internal-wave-measurement experiment was conducted from the Research Platform FLIP off the California coast. This paper discusses an 18-day sequence of velocity profiles obtained during the experiment using a pair of Doppler sonars. The sonars profile to a depth of 700 m, with approximately 20 m depth resolution. Plots of the velocity and shear field indicate the dominance of near-inertial motions. Much of the near-inertial variance can be ascribed to a few identifiable wave groups. The progress of these groups can be tracked for many days. The shear at the base of the mixed layer is often dominated by near-inertial motions propagating vertically through the thermocline rather than wind-forced motions in the mixed layer itself. Power-spectral analysis suggests that the low-frequency component of the wave field is dominated by the near-inertial and tidal peaks and their harmonics. The wisdom in modeling the low-frequency wave field as an "equivalent continuum" is questioned.

1. Introduction

It has become the practice in the last decade to characterize the oceanic internal wave field by a spectrum continuous in wavenumber and frequency. Garrett and Munk (1972) introduced the formalism of an "equivalent continuum" in order to account for the energy levels and spatial coherence observed in a variety of experiments. Inspired by the success of this approach, theoreticians (e.g., McComas, 1977; McComas and Müller, 1981) began to apply resonant-nonlinear-interaction theory in an attempt to understand why the equivalent continuum spectrum has the form that it does. McEwan and Plumb (1977) cautioned that the spectrum is, at best, continuous on average. The constituents needed to form potential resonant triads are not necessarily in the same volume of ocean at the same time.

As an added complication, there is now evidence suggesting that the low-frequency spectrum may not even be continuous on average. Harmonics of the 12 h tide have been seen in the IWEX data set (Briscoe, 1975), in data from the MILE experiment (Davis, 1981), and in previous work from FLIP (Pinkel, 1981b). Of course, one can always force a discontinuous spectrum to appear continuous by averaging spectral estimates in the frequency domain. However, increasing the averaging across ensembles will not necessarily increase the smoothness of the spectrum if harmonics are present.

In May 1980 observations were made of the upper-ocean internal-wave field off the coast of California using the Research Platform FLIP. Of the many sensors used in this study, a pair of downward-slanting Doppler sonars provided information pertinent to the issues raised above. The sonar data are of interest in that they extend continuously down to 700 m, which is approximately seven vertical correlation lengths for the low-frequency internal-wave field. Sporadic patterns in either space or time that cannot be resolved with statistical certainty by space or time series measurements alone are clearly apparent in the combined space-time view. This paper will describe the wave field as measured by the sonars. Both depth/time and depth/frequency information will be presented. These data will be used to explore the issue of the discrete versus the continuous nature of the instantaneous wave field.

2. Description of experiment

On 25 April 1980 FLIP departed San Diego for a station at 31°N, 124°W, approximately 400 km offshore. From this position FLIP drifted slowly to the south for the next 30 days. The onboard instrumentation included a profiling array of current meters developed by R. Weller of Woods Hole Oceanographic Institution (Weller, 1981). These profiled from 5 to 150 m every hour. A profiling CTD (Pinkel, 1975) sampled between 4 and 400 m every 2 min. Approximately 12 000 CTD profiles were collected during the trip. In addition four Doppler sonars mounted on FLIP's hull profiled 1100 m horizontally and 700 m vertically (Fig. 1). Two large (1.6 m diameter) sonars, operating at 80 and 85 kHz, were used in the horizontal measurements. These were mounted at a depth of 85 m, at right angles azimuthally. Two smaller (1.5 m × 0.75 m) sonars were

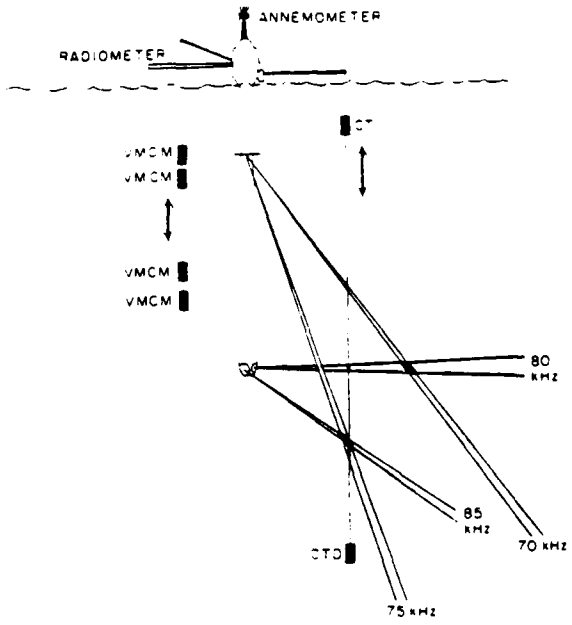

FIG. 1. Schematic diagram of the 1980 FLIP experiment. Sonar and profiling-CTD locations are indicated. The profiling current meter (VMCM) array was developed and operated by R. Weller. An array of surface-wave staffs is not shown in the figure.

mounted at a depth of 38 m, angled 45° downward, and operated at 70 and 75 kHz. This paper will discuss data from the downward-slanting sonars only (Fig. 2).

Data collection began on 3 May, after several days of testing the sonar equipment. Operations ceased on 22 May when FLIP's H.P. 21 MX computer failed. Approximately 18 days of continuous data were collected, with a one-day gap on 12–13 May for data-quality assessment. Prior to this gap 32 ms pings were transmitted every 2 s. The corresponding range resolution was 24 m. The associated depth resolution was 17 m for the slanting sonars. During the second, 11-day collection period, 40 ms pulses were transmitted every 1.5 s. These longer pulses improved the precision of the velocity estimates. The corresponding range and depth resolution were 30 and 21 m. The sonar echoes were complex-demodulated, filtered with a 100 Hz low-pass filter and sampled at 300 Hz. The Complex Covariance technique of Rummler (1968) was used to estimate Doppler velocity (Pinkel, 1981a). For subsequent analysis velocity estimates were averaged into 20 m range cells for the first data series, prior to the 12 May gap. Fifteen-meter range cells were used in the second data series. Velocity profiles were averaged over 6 min in time.

The time-series measurements from each sonar can be easily interpreted only if the azimuthal orientation of the sonar remains relatively constant throughout the measurement period. An automatic orientation-control system is used to regulate FLIP's heading. The system consists of a standard autopilot linked to the ship's gyro compass. The autopilot controls a set of hydraulically operated propellers mounted approximately 5 m off FLIP's hull axis. The system was able to maintain heading at 320° ± 20° true during the entire cruise. Typical heading stability was ±3°. However, squalls and major wind shifts produced the larger deviations.

During the second data-collection period a problem developed in the orientation system. A uniform oscillation of several degrees was introduced in the ship's azimuth at an 84 min period. The effect of this wobble is to introduce lines into the velocity spectra at even harmonics of the wobble frequency. This is apparent at some ranges in the power spectra to be presented.

A clear measure of sonar velocity precision was not available at sea. Independent tests conducted between two parallel sonars in November 1981 indicate that the measurements are uncertain to 1–2 cm s^{-1} after 2 min of pulse-to-pulse averaging. FLIP's response to individual wind gusts is of this order. A partially successful attempt to deal with wind-induced drift noise is described in the next section.

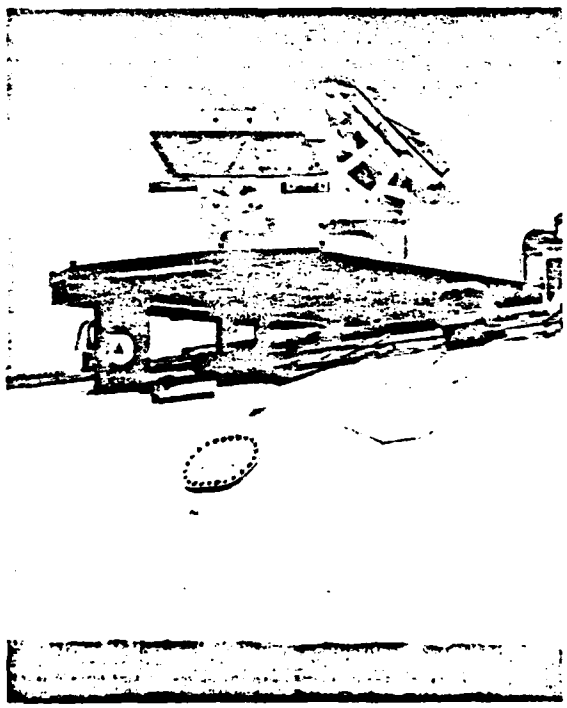

FIG. 2. The slant Doppler sonars. These were mounted at a depth of 38 m, angled 45° down. The beamwidth of these sonars is ~1° in the vertical and 2° in the horizontal. Pulses of 30–40 m duration were transmitted at a peak power level of 4–8 kW.

3. Ship drift

It is difficult to define an optimal coordinate system from which to observe wave propagation through an irregular, changing shear field. To drift with the average water velocity over the depth range of interest would seem to be a reasonable choice. FLIP's drift is determined by the flow in the upper 90 m of the sea and the wind. While this is far from ideal, it is felt that drifting provides a better frame of reference for observing internal waves than would be obtained by mooring the ship. The difference between FLIP's drift and the ideal is more critical in the present Doppler studies than in past CTD investigations (Pinkel, 1981b). Previous work was aimed at precise measurements of vertical velocity. Lateral drift contaminates these estimates in proportion to $\mathbf{u}_{\text{drift}} \cdot \nabla_H \eta$, where $\nabla_H \eta$ is the slope of the constant temperature surface being tracked. This slope is typically of order 0.02. In horizontal velocity measurements, the motion error adds directly to the signal, i.e.,

$$w_{\text{measured}} = w_{\text{true}} + \nabla_H \eta \cdot \mathbf{u}_{\text{drift}} \quad .$$

$$\mathbf{u}_{\text{measured}} = \mathbf{u}_{\text{true}} + \mathbf{u}_{\text{drift}} .$$

Fortunately, there is a method for estimating the drift error. Drift affects all ranges and depths identically. Thus it is a perfectly coherent source of noise. In contrast, internal waves become incoherent over 50–100 m in the vertical. As the measurements extend over 700 m in depth, the vertically averaged water velocity should be a reasonable estimate of FLIP's drift.

To check this method, the vertically averaged velocity from both sonars was time-integrated and a progressive-vector diagram was fabricated (Fig. 3). This represents FLIP's horizontal displacement with respect to a layer of "no motion" between 200 and 550 m. Also plotted on Fig. 3 are the Loran C navigation data. The discrepancy in these records represents the flow of the 200–550 m layer with respect to the sea floor. We find in retrospect that the layer has a mean motion of order 2 cm s^{-1} westward with respect to the bottom.

An attempt was made to estimate the rate of drift from minute to minute in order to remove it from the Doppler data. Both the Loran C and vertically integrated Doppler velocity data were tried. It was found that the Doppler data are more precise than the Loran C for this task. Loran C has a 20–100 m random position uncertainty off the California coast. In order to measure drift rate to 1 cm s^{-1} precision in 5 min, ~100 *independent* determinations of Loran position must be obtained. This is not feasible. On the other hand, Doppler velocity measurements must be integrated in time to determine position. In this process both random and systematic errors grow. Thus Loran C is a better long-term indicator of position while the Doppler measurements are a better indicator of short-term drift rate.

It should be noted that FLIP's motion, in addition to serving as a source of noise, Doppler-shifts the observed frequencies of internal waves. Attempts to "subtract out the drift" using navigation or other techniques can remove the velocity noise. However, these corrections will not remove the errors in the measured frequency of the waves induced by the drift.

4. Depth-time representation

A variety of techniques were used to examine the Doppler data prior to statistical analysis. The most graphic display was found to be a color contour map of slant velocity or shear versus depth and time. The shear map emphasizes shorter vertical scales and requires no correction for FLIP's drift. Since the dominant shears occur at low frequency, where horizontal wavelengths are long and vertical velocities are small, the slant-sonar information can be interpreted as a vertical profile of horizontal shear. These maps are presented in Figs. 4 and 5. The units are those of equivalent horizontal velocity and shear, i.e.,

$$\Delta u_H/\Delta z = (\Delta u_{\text{Doppler}}\sqrt{2})/(\Delta r/\sqrt{2}) = 2\Delta u_{\text{Doppler}}/\Delta r.$$

In excess of 4×10^5 six-minute-average velocity estimates were used in forming these maps. Gaps in the data are indicated by the horizontal bars visible in the maps. Velocity and shear components in the direction 055° are presented in the left map (70 kHz sonar) and 325° in the right map (75 kHz sonar). Positive shear (red) implies an increase in relative velocity in these directions with increasing depth. The data were smoothed with a rectangular lag window 1 h in time, 40 m in range.

In a preliminary plot, the data were scaled in a WKB sense using accurate measurements of the Brunt-Väisälä profile obtained from a Neil Brown CTD at the beginning and end of the cruise. It was found that in the top 250 m, the seasonal thermocline, the WKB depth stretching distorted the simple patterns of vertical phase progression which were apparent in the unstretched data. When a smoothed Brunt-Väisälä profile (the Garrett-Munk exponential profile) was used as a basis for the stretching, the distortion was reduced significantly.

As expected, the depth-time displays are dominated by near-inertial motions. It is interesting that a relatively small number of inertial-wave packets dominate the near-inertial-wave field. The sense of both group and phase propagation can be clearly seen when Fig. 5 is examined closely. At the start of the observations a packet is seen in the upper 200 m of the sea with upward-propagating crests. Its vertical wavelength is ~125 stretched meters. Less intense motions with larger vertical scales occupy the water column below. As the cruise progresses, the packet

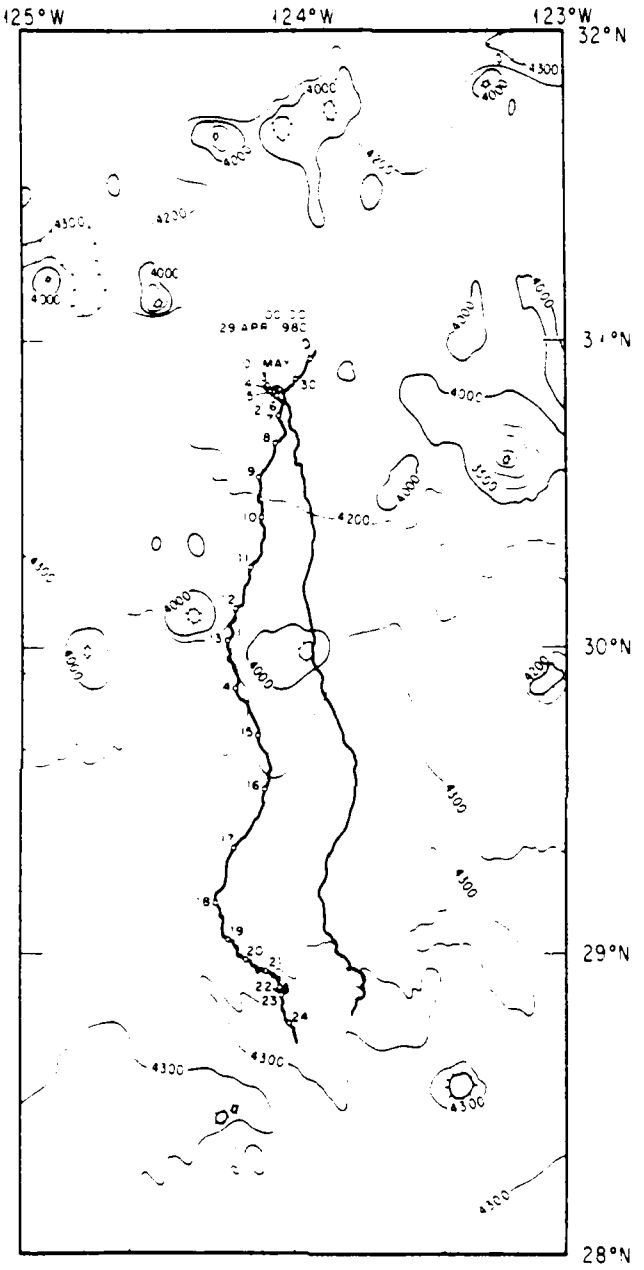

FIG. 3. A map of FLIP's drift. The left-most line represents the time series of FLIP's position as determined by Loran C. Numbered circles indicate the date. The right track is the progressive vector formed by time-integrating the 200–550 m depth-averaged Doppler velocities sensed by the sonars.

expands slowly downward. By 13 May it fills the entire depth range, having traveled ~550 m in 10 days. After 15 May, the near-surface crests weaken as this packet propagates downward out of the field of view. The broken line on the 70 kHz shear map indicates the downward expansion of the group.

An upward-propagating group (downward-propagating crests) is present from 11 May onward. The combined effect of these two groups produces a "herringbone" pattern in the shear data between 11 and 16 May. After this time both groups have passed out of view but remnants of the upward-propagating group remain.

The velocity map (Fig. 4) presents a more confused

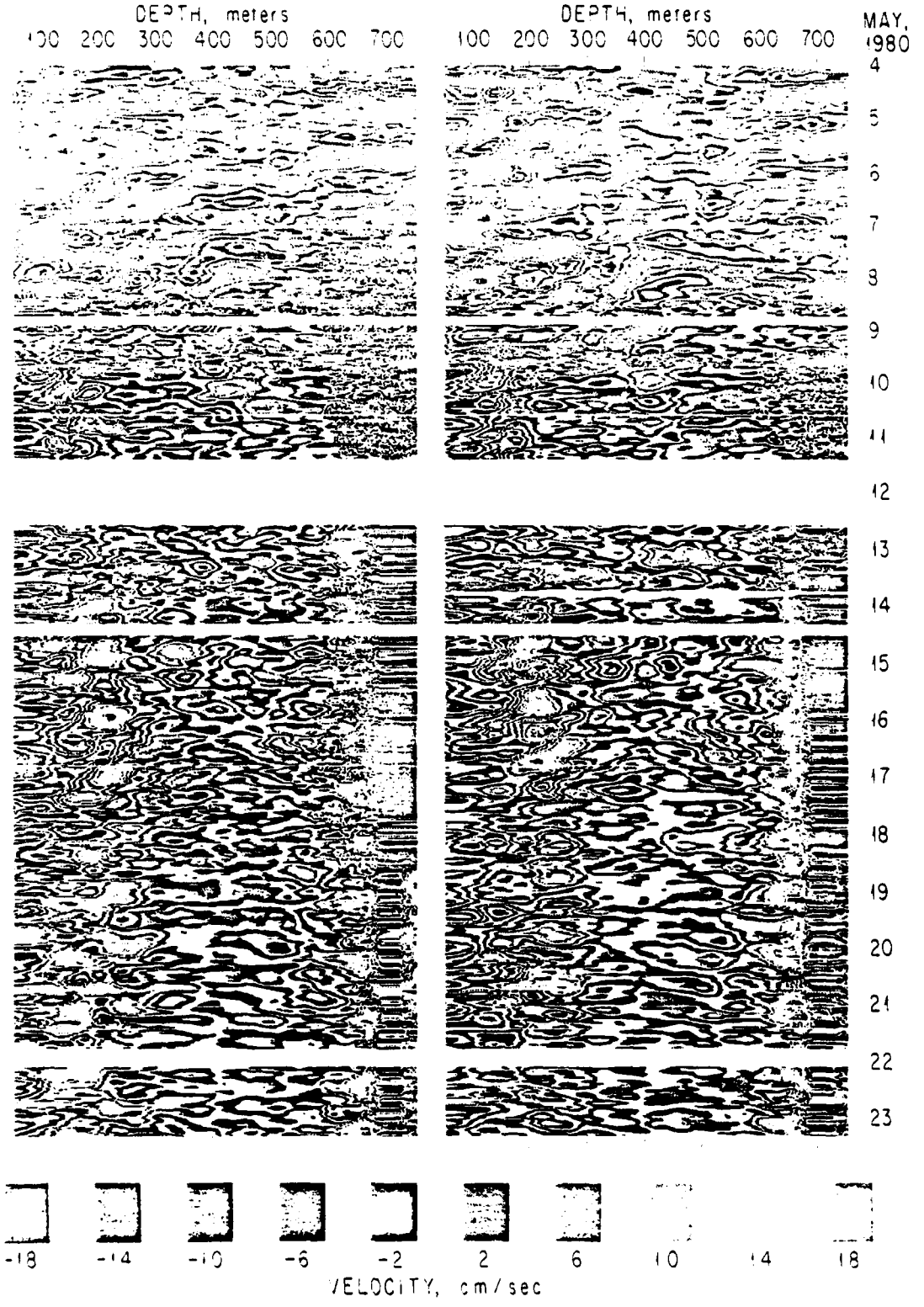

FIG. 4. A contour map of the observed velocity field. The 70 kHz (left) and 75 kHz (right) sonar velocities are positive toward 55°T and 325°T, respectively. In this plot the mean velocity in the layer 200–550 m has been removed, to minimize the effects of *FLIP*'s drift. *Gaps in the data are indicated by the horizontal white bands. The very fine scale structure at great* range is instrument noise.

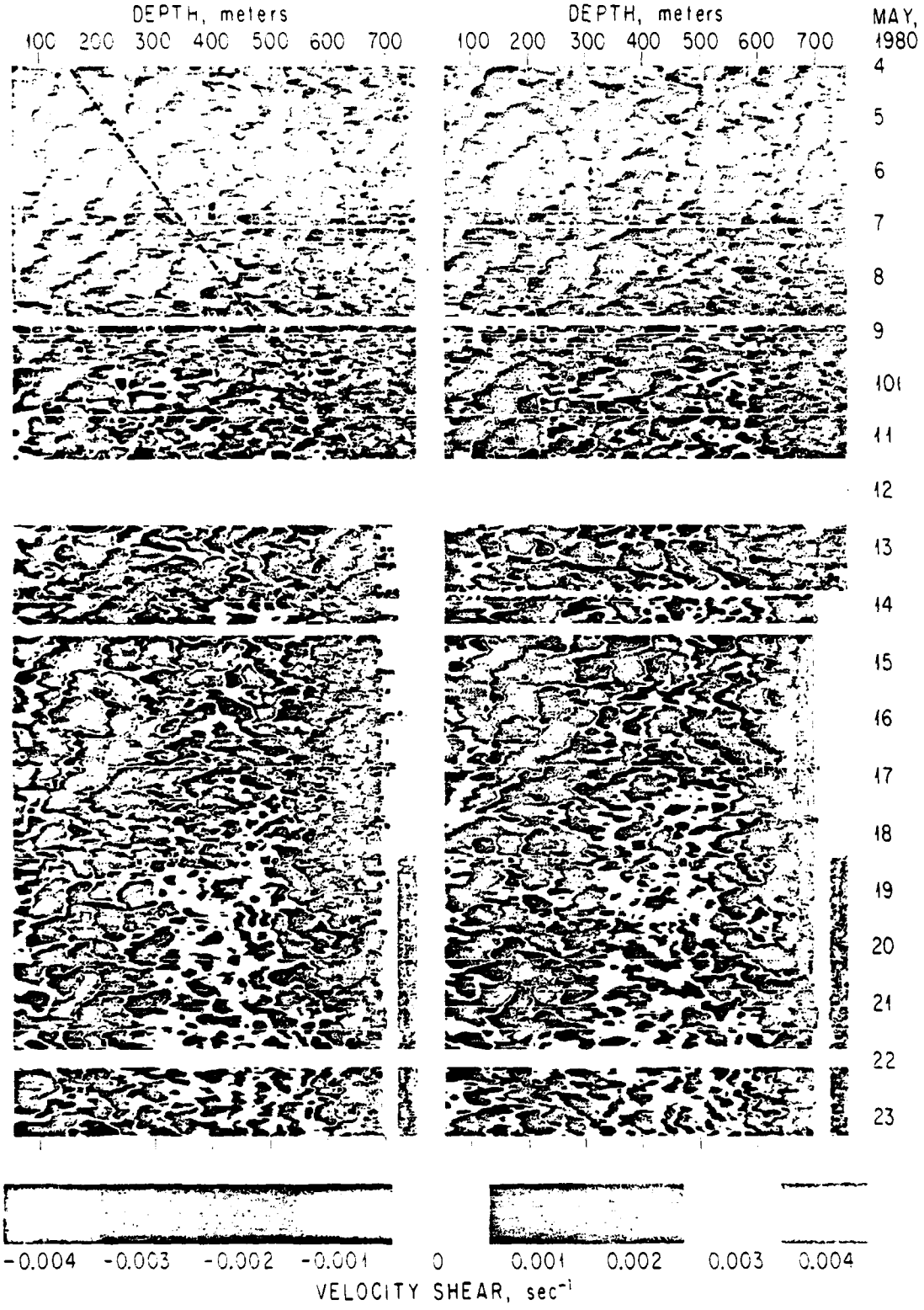

FIG. 5. A contour map of the observed shear field using the 70 and 75 kHz sonars as in Fig. 4. Positive shear implies velocity increasing toward 55°T (325°T) with increasing depth. The broken line on the 70 kHz plot indicates the downward expansion of a near-inertial group which dominates the shear field during the early part of the cruise.

picture than the shear map. The two groups mentioned previously can be identified. In addition, a third group, with a vertical wavelength of ~500 m, can be identified during the first four days, from 4–8 May. This group propagates downward. Note that the longer-vertical-wavelength groups are more easily identifiable in the velocity map.

5. Depth-time discussion

Depth-time plots that demonstrate near-inertial vertical propagation were first presented by Leaman and Sanford (1975). A number of things can be learned by inspection when data are presented in this format. For example, the propagation properties of near-inertial groups depend strongly on the small difference between the actual wave frequency and the local inertial frequency. One would like to be able to measure the frequency difference $(\omega - \omega_i)$. When spectral analysis techniques are used to determine wave frequency, time series that are long compared to $(\omega - \omega_i)^{-1}$ are necessary to achieve adequate frequency resolution. If the duration of the packet is less than this time $[\Delta\omega > (\omega - \omega_i)]$, the data are nonstationary. Estimates of wave frequency derived from time-series information will not be accurate. From a depth-time display, both the vertical phase speed and vertical wavelength of a near-inertial packet can be read directly. Wave frequency is given by the product $\omega = c_{p_z} k_z$. The accuracy in this estimate depends on the degree to which wave phases can be followed. The frequency bandwidth of the packet is the inverse of the time required for a packet to pass through a given depth. It can be inferred independently of the wave-frequency estimate. As examples, the near-inertial packets present in Figs. 4 and 5 can be examined. Consider the downward-propagating group with vertical wavelength ~125 stretched meters which is present from 7 to ~18 May (Fig. 5). The crests in this group propagate upward at a rate of ~700 m in 4.5 days, or 155 m day^{-1}. From the definition of the phase speed, $c_{p_z} = \omega/k_z$, we infer that the frequency of this group is ~1.24 cpd. Using the linear internal-wave-dispersion relation $k_z = k_H[(N^2 - \omega^2)/(\omega^2 - f^2)]^{1/2}$, the horizontal wavelength of the waves in this packet is estimated at 8.5 km, assuming a mean Brunt-Väisälä frequency of 2 cph. Also from linear theory (Phillips, 1977, Eq. 5.7.21), the vertical component of group velocity is

$$c_{g_z} = |\omega^2 - f^2|^{3/2}(N^2 - \omega^2)^{1/2}[k_H\omega(N^2 - f^2)]^{-1}.$$

For this packet, with upward-propagating crests, the vertical component of group velocity is of order 54 m day^{-1}, downward. This is in good agreement with the observed vertical advance of the group.

The vertical wavelength of the second, upward-propagating group is of order 225 m. Its downward vertical phase velocity is ~250 stretched meters per day. The corresponding frequency of the packet is 1.1 cpd. The waves in this packet have a horizontal wavelength of 25 km. The vertical component of group velocity is 43 m day^{-1} upward.

In addition to estimating wave-field parameters, the depth-time plot can be used to answer an existing air/sea-interaction riddle. It has recently been established (Weller, 1981; Davis *et al.*, 1981) that mixed-layer horizontal currents are highly coherent with the wind at the inertial frequency. However, the coherence is rapidly lost in the upper thermocline. The reason for this is clear on inspection of Figs. 4 and 5. In order for wind-generated near-inertial energy to propagate downward into the thermocline, the associated wave crests must propagate upward. Wave crests arriving in the upper thermocline can be traced back in time for 4–6 days. They can be followed in depth for 500 m. It would be fortuitous if variations in local wind occurred in concert with upper-thermocline motions that had been "on the road" upward for nearly a week.

6. Depth-frequency representation

The data of Figs. 4 and 5 can be regarded as a set of time series at successive depths and processed in a manner similar to that for conventional moored current measurements. It is expected that the power spectra of slant velocity will be dominated by the near-inertial motions so apparent in Fig. 5. At issue is whether the higher frequencies constitute a spectral continuum or are dominated by harmonics of the inertial and tidal signals (Pinkel, 1981b). The investigation is complicated by the fact that it is difficult to detect fine-scale structure in spectra which have a steep mean slope. To avoid this difficulty, spectra of the velocity series first-differenced in time over the 5 min sampling interval will be presented in this section. These are effectively slant acceleration spectra. They are related to the more familiar velocity spectrum by the factor $[2 - 2\cos(\pi\omega/\omega_N)]^{-1}$, where ω_N is the Nyquist frequency. A white acceleration spectrum implies an ω^{-2} velocity spectrum.

To form these spectra the data were divided into a 7- and an 11-day segment. These were separated by the down period on 12 May. Smaller gaps in the two data series were zero-filled. The first-differenced signals were then multiplied by a triangular data window and digitally Fourier transformed. Fourier coefficients were calculated at 0.10 cpd increments. The vertical mean of each Fourier coefficient over the depth interval 100–500 m was subtracted from the value at each depth, in an effort to remove the effects of FLIP's drift. The squared coefficients from both data segments were then averaged together and smoothed in frequency to increase the statistical stability of the spectral estimates.

A sequence of slant acceleration spectra from the 75 kHz sonar is presented in Fig. 6. The spectra rise 10–20 db at the inertial frequency and undulate ir-

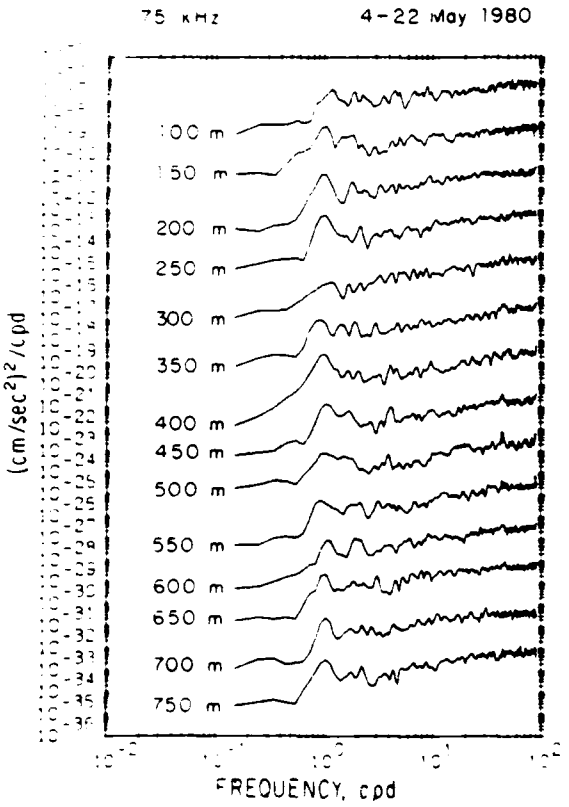

FIG. 6. Slant acceleration spectra from the 75 kHz sonar. The sonar was pointed in the direction 145°T. The spectra are estimated at approximately 8 degrees of freedom to 2.5 cpd, 24 degrees of freedom to 5 cpd. Above 5 cpd the spectral averaging is progressively increased, reaching approximately 1200 degrees of freedom between 10 and 100 cpd. The averaging was achieved by low-pass filtering the spectral estimate. Adjacent spectral points are not independent.

regularly up to 5–10 cpd. At this point a clear rise in spectral level is seen, with approximate slope $\omega^{2/3}$. At high frequency the spectra again become level. The level region extends to increasingly lower frequency at greater depths, indicating the decrease in Brunt-Väisälä frequency with depth. The leveling of these acceleration spectra correspond to the steepening in slope of velocity spectra above the local Väisälä frequency. The cut-off is not seen here to a greater extent because of noise introduced by zero-filling through periods of equipment malfunction, errors in removing FLIP motion, and so-called finestructure contamination.

An attempt was made to combine the data from both slanting sonars to form rotary spectra of clockwise and counterclockwise motion, as originally suggested by Gonella (1972). This effort is motivated by a desire to quantify the rotational patterns visible in Figs. 4 and 5. The procedure is suspect in that the orthogonal components are sensed in different volumes in space. At 700 m depth, the volumes are separated by 1 km. On the other hand, the expected difference in horizontal velocity over 1 km horizontally is on the order of 1–2 cm s^{-1}. Large errors are not anticipated, particularly at low frequency. With this caution, the rotary slant acceleration spectra at depths from 100–750 m are presented in Fig. 7. The clockwise (viewed from above) component spectra resemble the individual sonar spectra presented previously. They rise abruptly at the inertial frequency and oscillate irregularly up to 5–10 cpd. Above this frequency they rise slightly until 40–60 cpd where they level off. The counterclockwise spectra do not show the abrupt inertial rise. They maintain a gentle ω^{+1} form from inertial frequency to the "Väisälä leveling" region.

The spectra of Figs. 6 and 7 lack the statistical stability necessary to address the issue of the continuity of the low-frequency spectrum. It is necessary to improve the precision of the spectral estimates without smoothing out possible harmonic structure. This can be done by averaging over depth. Depth-averaged rotary spectra from the first and second data collection periods are presented in Fig. 8. The clock-

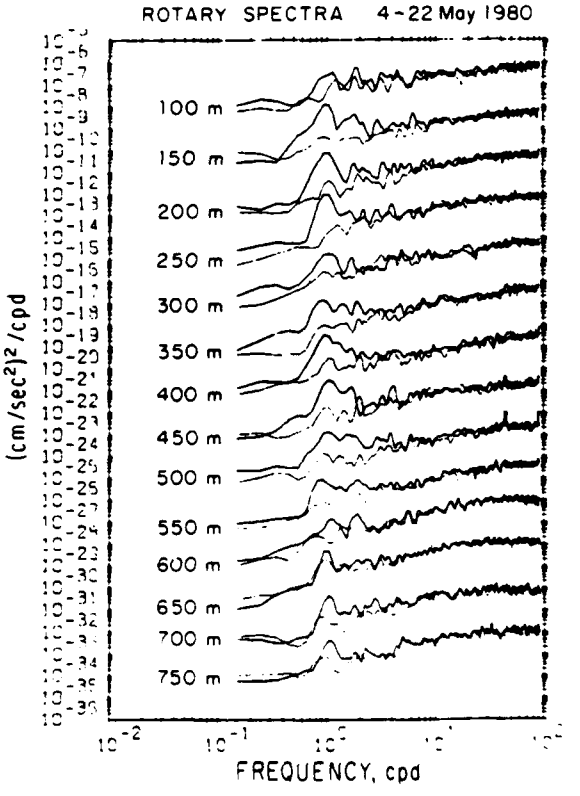

FIG. 7. Rotary slant-acceleration spectra. The clockwise spectra are indicated by the heavy line. The same smoothing is employed as in Fig. 6.

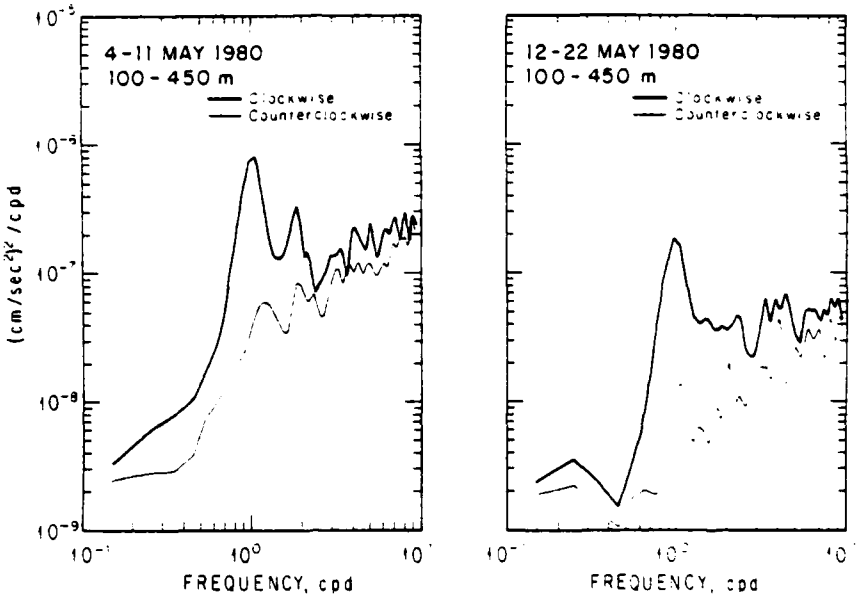

FIG. 8. Depth-averaged rotary slant-acceleration spectra, 4–11 May and 12–22 May 1980. Eight spectra, at 50 m intervals between 100 and 450 m, are combined to form each spectral estimate. There are nominally 64 degrees of freedom below 2.5 cpd, 192 degrees of freedom below 5 cpd. The actual statistical stability of this estimate is less than indicated by the number of degrees of freedom, as adjacent depths are not statistically independent. The clockwise spectra are indicated by the heavy lines.

wise depth-averaged spectra are presented again in Fig. 9, on a linear scale.

Slant coherence and phase are plotted in the lower sections of Fig. 9. Coherence is estimated at slant separations of 20 and 40 m for the first data segment, and 15 and 45 m for the second. Generally, high spectral levels correspond to high values of coherence. The overall coherence pattern is quite similar to the IWEX pattern shown by Briscoe (1975). There are several significant differences. These are spectra of slant rather than horizontal velocity/acceleration. The cross spectra have been averaged so as to maintain rather than smooth out the spectral peaks. Also, in the process of removing the "mean ship drift" from the Doppler measurements, an unknown amount of coherent internal-wave energy is removed. When drift is not removed, the coherence patterns are unchanged below 6–10 cpd. At higher frequencies the coherences are much higher in the uncorrected data. Drift acceleration is a significant part of the high-frequency signal.

The associated phase spectra are presented for the smaller of the two slant separations in Fig. 9 (bottom). During the first observation period the inertial peak and its harmonics indicate upward phase propagation and downward energy propagation. The tide and its first harmonic exhibit little sense of vertical propagation. In the less energetic second observing period significant anisotropy occurs only at the near-inertial frequency. Downward energy propagation is seen.

7. Depth-frequency discussion

The slight positive slope to these spectra is somewhat puzzling. Typically, moored temperature sensors produce displacement spectra of form ω^{-2} at frequencies between the M2 tide and a pre-cut-off shoulder at ~20 cpd (Briscoe, 1975; Pinkel, 1975). Theory suggests that the corresponding horizontal velocity spectra should also be of form ω^{-2}. Horizontal acceleration spectra should be white. Curiously, this is rarely found. Briscoe (1975) was the first to emphasize the discrepancy. His IWEX temperature spectra have the customary ω^{-2} form, but the velocity spectra have an $\omega^{-5/3}$ slope. A similar effect is seen in these slant acceleration spectra. They are nearly white, in agreement with the temperature spectra, up to ~5 cpd. Above this frequency the $\omega^{2/3}$ form implies an even whiter velocity spectrum than in the IWEX data. Part of this "excess" variance at high frequency is a consequence of measuring 45° slant velocity rather than horizontal. The contribution of vertical acceleration to these spectra is negligible at low frequency, but significant at high frequency. This effect can explain only part of the high-frequency increase. The basic discrepancy noted by Briscoe (1975) is supported by the Doppler data.

As anticipated, the depth-averaging did not significantly increase the "smoothness" of the spectral estimates. However this is not a strong indication of spectral harmonics. Even in a linear wave field, wave

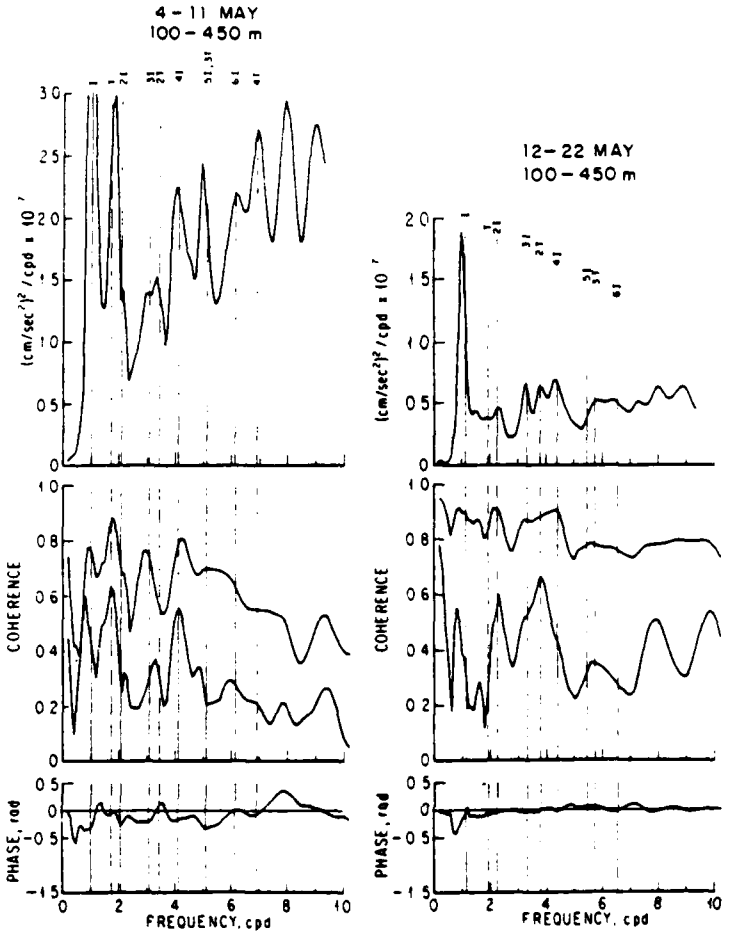

FIG. 9. Depth-averaged clockwise slant-acceleration spectra, slant coherence and phase, 100–450 m average. The power spectra are identical to those in Fig. 8, except plotted on linear scales. Note that the large inertial peak in the 4–11 May data has been truncated. It actually reaches a value of 9×10^{-4} $(cm/s^2)^2/cpd$. Coherences are plotted for slant separations of 20 and 40 m in the 4–11 May data, 15 and 45 m for the 12–22 May data. Coherence values at the smaller of these separations are slightly overestimated. This results from the finite length of the acoustic pulse, which averages over 30–40 m in space.

groups dominant at one depth can be expected to dominate at other depths. Wave energy is coherent in depth over greater scales than wave phase. This is a consequence of the ability of internal waves to propagate vertically.

In order to investigate the presence of harmonics further, a set of reference lines is drawn in Fig. 9 at suspected harmonic frequencies. In an effort to be objective, the spacing of these reference lines has been determined using only the positions of the suspected higher harmonic peaks. The case for harmonics is convincing to the extent that the inferred position of the fundamental reference line actually falls on the observed inertial or tidal peak. It is seen that the agreement is good, but not spectacular.

It should be noted that in the first observational period, both the inertial and tidal peaks are far stronger than in the second. Interestingly, the higher frequency "harmonics" are also stronger. The ratio of the harmonic spectral level to that of the fundamental is of order three or four to one. However, it is doubtful that acceleration spectra are the optimal statistical quantity to use in studying this phenomena. In Fig. 9b, the first harmonic of the tide appears to have more acceleration variance than the tide itself. This would not be the case in the associated velocity or slant displacement spectra.

It is somewhat disturbing that even in the vertically averaged spectra the demonstration of the harmonics is not unequivocal. It might be argued that Figs. 8

and 9 are simply irregular spectra, plotted so as to emphasize the irregularities. With so many distinct peaks and so many harmonic combinations possible some agreement is likely. However this sort of low-frequency structure is being found in a great many studies. Davis *et al.* (1981) and Pinkel (1981b) report significant harmonic structure in northeast Pacific data. Paulson (personal communication, 1982) reports harmonics in JASIN data from the northeast Atlantic. Harmonic structure of "marginal statistical significance" is often found, if properly looked for. Detection depends on the averaging of the data in a manner consistent with the space–time patterns of the near-inertial and tidal groups that dominate the low-frequency end of the spectrum.

An additional issue is whether the harmonics represent the truly dynamic phenomenon of forced waves or are a kinematic manifestation of the way in which the wave field is observed. Phillips (1971) noted that if a background step-like temperature profile is advected sinusoidally in the vertical past a fixed depth sensor, the sensor output is a square wave. The associated power spectrum of the temperature series consists of a sequence of peaks at the fundamental frequency and its odd harmonics. Is this the effect responsible for the observed spectral patterns? Early simulations indicated that the contamination would be important only at high frequency, where there was little natural signal. The dominance of the tidal and inertial signal at low frequency was not anticipated in these studies.

From the sonar data alone, which is presumably finestructure contaminated, it is not possible to distinguish between the kinematic and dynamic hypotheses. However, the CTD profiling measurements taken in conjunction with the sonar observations can discriminate between these effects. Profiling data can be analyzed in terms of temperature time series at fixed depth, vertical-velocity series at fixed depth, or isotherm-displacement time series. The first of these approaches is fine-structure contaminated. The second, while Eulerian, is not. The isotherm-displacement method is, in a sense, semi-Lagrangian. The vertical motion of a constant temperature surface is tracked. These too should not be contaminated. Spectra of these three quantities have been calculated from the same set of May 1980 profiles. All show harmonic structure. It is thus doubtful that finestructure contamination is the source of these harmonics.

8. Summary

The near-inertial field during the 18 days of observations is dominated by a few groups at any one time. The difference in horizontal wavenumbers of the groups is sufficiently large that the horizontal correlation scale of the motions is less than the likely horizontal extent of any of the constituent groups. Shear events in the upper thermocline are predictable from deeper measurements as much as five days in advance. Near-inertial motions in the upper thermocline will have little coherence with mixed-layer motions and the local wind as they are more directly related to deeper, upward-propagating wave phases. This picture is not inconsistent with the wind generation of these motions.

Off the coast of California the so-called continuum region of the wave spectrum (from 2 to 5 cpd) is dominated by harmonics of the tide and inertial peaks. When these fundamental frequencies are increased in energy, the "continuum" levels are also higher. The harmonic peaks are generally associated with maxima in the slant coherence. It is likely that they are not just an artifact of fine-structure contamination.

The existence of these highly irregular spectra is curious given recent theoretical developments by McComas (1977) and McComas and Müller (1981). These indicate that isolated spectral peaks will tend to diffuse into the "background spectrum" very rapidly, as a result of resonant nonlinear interactions. Significant amounts of energy must be provided to the wave field at discrete frequencies in order to maintain the observed peaks. Alternatively, the nonlinear models overestimate the energy-transfer rates within the spectrum.

Acknowledgments. The author would like to thank L. Occhiello, Eric Slater, Lee Tomooka and W. Whitney for designing, developing and operating the Doppler sonar system on FLIP. W. Davy led the MPL development group in constructing the eight tons of sonar equipment involved. DeWitt Efird, the captain of FLIP, accommodated this equipment on his vessel and operated it safely for the duration of the operation. Discussions with Russ Davis, W. Hodgkiss, Walter Munk and Lloyd Regier were particularly helpful in the development of this work. This program is funded by ONR Code 220, ONR Code 200, and NORDA Code 540. Contribution of the Scripps Institution of Oceanography, new series.

REFERENCES

Briscoe, M. B., 1975: Preliminary results from the tri-moored internal wave experiment (IWEX). *J. Geophys. Res.*, **80**, 3872–3884.

Davis, R. E., R. de Szoeke and P. Niiler, 1981: Variability in the upper ocean during MILE. Part II: Modeling the mixed layer response. *Deep Sea Res.*, **28A**, 1453–1475.

Garrett, C. J. R., and W. H. Munk, 1972: Space-time scales of internal waves. *Geophys. Fluid Dyn.* **2**, 225–264.

Gonella, J., 1972: A rotary-component method for analyzing meteorological and oceanographic vector time series. *Deep Sea Res.*, **19**, 833–846.

Leaman, K. D., and T. B. Sanford, 1975: Vertical energy propagation of inertial waves: A vector spectral analysis of velocity profiles. *J. Geophys. Res.*, **80**, 1975–1978.

McComas, C. H., 1977: Equilibrium mechanisms within the oceanic internal wave field. *J. Phys. Oceanogr.*, **7**, 836–845.

——, and P. Müller, 1981: Time scales of resonant interactions among oceanic internal waves. *J. Phys. Oceanogr.*, **11**, 139–147.

McEwan, A. D., and R. A. Plumb, 1977: Off-resonant amplification of finite internal wave packets. *Dyn. Atmos. Oceans*, **2**, 83–105.

Phillips, O. M., 1971: On spectra measured in an undulating layered medium. *J. Phys. Oceanogr.*, **1**, 1–6.

——, 1977: *The Dynamics of the Upper Ocean*. 2nd ed. Cambridge University Press, 336 pp.

Pinkel, R., 1975: Upper ocean internal wave observations from FLIP. *J. Geophys. Res.*, **80**, 3892–3910.

——, 1981a: On the use of Doppler sonar for internal wave measurements. *Deep Sea Res.*, **28A**, 269–289.

——, 1981b: Observations of the near-surface internal wavefield. *J. Phys. Oceanogr.*, **11**, 1248–1257.

Rummler, W. D., 1968: Introduction of a new estimator for velocity spectral parameters. Tech. Memo. MM-68-4141-5, Bell Telephone Laboratories, Red Bank, NJ, 24 pp.

Weller, R. A., 1981: Observations of the velocity response to wind forcing in the upper ocean. *J. Geophys. Res.*, **86**, 1969–1977.

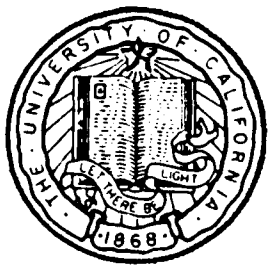

MPL TECHNICAL MEMORANDUM 359

Doppler Sonar and Profiling CTD Observations of the Interrelationship Between Large and Small Scale Internal Waves

by Robert Pinkel

Project Report for
Naval Ocean Research and Development Activity
Contract N00014-79-C-0983
Code 540

14 February 1984

MPL-U-29/83

MARINE PHYSICAL LABORATORY
of the Scripps Institution of Oceanography
San Diego, California 92152

Doppler Sonar and Profiling CTD Observations of the Interrelationship between Large and Small Scale Internal Waves

PROJECT REPORT

NORDA, Code 540

Rob Pinkel

University of California, San Diego
Marine Physical Laboratory of the
Scripps Institute of Oceanography
La Jolla, California 92093

Introduction

Over the past decade enormous progress has been made in the measurement of the various classes of motions in the sea. Specialized techniques have been developed to measure small scale turbulence, fine structure, internal waves, mesoscale eddies, and other phenomena. A current objective of considerable importance to both the Naval and the research communities is to understand the interrelationships and interaction between these various scales of motions. The ideal would be to be able to predict the occurance and evolution of small scale motions in the presence of the larger scale backgrounds.

At the Marine Physical Laboratory, two instrument systems have been developed for the purpose of bridging the gap between large and small scales. A profiling CTD was constructed in the early 1970's. This senses the vertical displacements in the sea by tracking the depths of isothermal or isopycnal surfaces. Vertical scales of

1 m to 400 m are resolved by the system. In the late 1970's Doppler sonar technology was developed. Sonars provide the capability to profile in directions other than vertical. Ranges in excess of 1 km can be sampled. However, the sonar range resolution is worse than the CTD, being approximately 20 m. The history of sonar development at MPL and a detailed description of the system are presented in Pinkel 1981a.

During May 1980 an upper ocean experiment was conducted using these systems on the Research Platform FLIP. Eighteen days of sonar and CTD data were collected as FLIP drifted slowly southward in the California current, approximately 400 km offshore. Support was obtained from Norda Code 540 to intercompare the data from these different sensing systems. Of particular interest is how these systems respond to the large scale shears in the upper ocean and how they measure the smaller scale wave motions which must propagate through these shears.

This report will document the view of the upper ocean as seen by the Doppler sonar and the CTD systems. Data from the May 1980 operation, as well as from earlier FLIP operations will be presented. Examples of depth-time series and power spectra will be presented for both systems. Combined wavenumber-frequency spectra will be used to demonstrate the relative amplitudes of the large scale-low frequency versus the small scale high frequency signals. Emphasis will be placed on the types of motions which are missed as well as measured by these two systems, as well as on disagreements in the measurements obtained.

Description of Experiment

On 25 April 1980 FLIP departed San Diego for a station at 31°N, 124°W, approximately 400 km offshore. From this position FLIP drifted slowly to the south for the next 30 days. The onboard instrumentation included a profiling array of current

meters developed by R. Weller of Woods Hole Oceanographic Institution (Weller, 1981). These profiled from 5 m to 150 m every hour. The profiling CTD (Pinkel, 1975, Occhiello and Pinkel, 1976) sampled between 4 and 400 m every two minutes. Approximately twelve thousand CTD profiles were collected during the trip. In addition four Doppler sonars mounted on FLIP's hull profiled 1100 m horizontally and 700 m vertically (Fig. 1). Two large (1.6 m diameter) sonars, operating at 80 and 85 kHz, were used in the horizontal measurements. These were mounted at a depth of 85 m, at right angles azimuthally. Two smaller (1.5 x 0.75 m) sonars were mounted at a depth of 38 m, angled 45° downward, and operated at 70 and 75 kHz. This paper will discuss data from the downward slanting sonars only (Fig. 2).

Data collection began on 3 May, after several days of testing the sonar equipment. Operations ceased on 22 May when FLIP's H.P. 21 MX computer failed. Approximately 18 days of continuous data were colected, with a one-day gap on 12-13 May for data quality assessment. Prior to this gap 32 ms pings were transmitted every two seconds. The corresponding range resolution was 24 m. The associated depth resolution was 17 m for the slanting sonars. During the second, 11-day collection period, 40 ms pulses were transmitted every 1.5 seconds. These soner pulses improved the precision of the velocity estimates. The corresponding range and depth resolution is 30 and 21 m. The sonar echoes were complex demodulated, filtered with a 100 Hz lowpass filter and sampled at 300 Hz. The Complex Covariance technique of Rummler (1968) was used to estimate Doppler velocity. Velocity profiles were averaged over 5 minutes in time.

The time series measurements from each sonar can be easily interpreted only if the azimuthal orientation of the sonar remains relatively constant throughout the measurement period. An automatic orientation control system is used to regulate FLIP's heading. The system consists of a standard autopilot linked to the ship's

gyro compass. The autopilot controls a set of hydraulically operated propellers mounted approximately 5 m off FLIP's hull axis. Ths syster was able to maintain heading at $320^{\circ} \pm 20^{\circ}$ true during the entire cruise. Typical heading stability was $\sim 3^{\circ}$. Larger deviations resulted from passing squalls and frontal systems.

Velocity and Shear Spectra

The downward slanting Doppler sonars provide profiles of 45° slant velocity as a function of depth. (Fig. 3). These can be differentiated with respect to range to provide an estimate of the shear field. The differentiation cannot be done arbitrarily, however. The sonar profiles have finite range resolution (20 - 30 m for the May 1980 data). Taking the velocity difference with range over an interval shorter than this would tend to give an artificially small result. To investigate the effect of the differencing interval, several different intervals were tried. Power spectra of the shear calculated at two different intervals are presented in Fig. 4. The spectra are only moderately smoothed, hence they appear very irregular. Spectral slope varies between ω^{-2} and ω^{-1}. Note that as the differencing interval is increased the form of the shear spectrum approaches that of the classical ω^{-2} velocity spectrum. This is a consequence of the mathematics behind the analysis. If we consider two signals $u_1(t)$, $u_2(t)$ with power spectra $\langle u_1^2 \rangle (\omega)$, $\langle u_2^2 \rangle (\omega)$, the power spectrum of the <u>difference</u> between the two signals is just

$$\langle |(u_1 - u_2)|^2 \rangle (\omega) = \langle u_1^2 \rangle (\omega) + \langle u_2^2 \rangle (\omega)$$

$$-2\mathrm{Re} \langle u_1 u_2^* \rangle (\omega)$$

The difference spectrum is equal to the <u>sum</u> of the individual signal spectra minus twice the cospectrum, $C(\omega) = \mathrm{Re} \langle u_1 u_2^* \rangle$, between the signals. The magnitude of the cospectrum depends on the degree to which the two signals are coherent and are in phase. If the signals are perfectly coherent and in phase, the cospectrum between the two signals will equal the spectrum of either (identical) signal. If the coherent signals are 180° out of phase, the cospectrum will be the negative of the individual power spectra. If the signals are perfectly coherent but plus or

minus ninety degrees in phase, the cospectrum will vanish. Here the so-called quadrature spectrum

$$Q(\omega) \equiv \mathrm{Im} \langle u_1 u_2^* \rangle (\omega)$$

will be large. The quadrature spectrum plays no role in the discussion of shear estimation, however. It is important to note that, as the two signals become less coherent, the magnitude of the cospectrum will be reduced. In the limit of zero coherence the spectrum of the difference between two signals is just the sum of the spectra of the individual signals.

With the sonar data, the relevant signals are the velocity time series at various ranges. If ranges too close together are used, the signals will be perfectly coherent, and the shear spectrum will be zero. The finite range resolution of the sonars tends to make nearby velocity series look identical. Thus, it is important not to use signals which are spatially separated by less than the resolution distance of the sonar. However, if series too far apart are used in the shear estimation, the signals will be incoherent. The resulting spectrum will be the sum of the individual velocity spectra. Nothing new will be learned about the ocean by taking their difference.

The shear spectra of Fig. 4 are typical of unsmoothed shear spectra obtained by other means. Two noteworthy aspects are that the dominant shear is at low frequency, and that the spectra are dominated by noise at frequencies above 2 cph.

It is difficult to assess the significance of the many irregularities in the shear spectra. It has been found useful to first difference these data in time prior to Fourier transformation to produce spectra which are 'white' in frequency. Significant irregularities are easier to detect against a flat spectral background.

Smoothed plots of the resulting acceleration (of velocity, not shear) spectra are presented in Fig. 5. These are formed by combining data from the two downward slanting sonars so as to obtain rotary spectra. The dark line corresponds to clockwise motion (viewed from above) while the lighter line to the counterclockwise motion. The spectra are plotted for two time periods during the May 1980 cruise. During the period 4-11 May both tidal and inertial signals were quite strong. These are seen in the left hand spectrum of Fig. 5. They dominate the low frequency portion of the clockwise spectrum. Higher frequency irregularities in the spectrum can be identified with harmonics of these low frequency peaks. The correspondence between spectral peaks and the theoretical position of harmonic lines is less than perfect. During the period 12-22 May 1980 the tidal and inertial signals are much weaker. Interestingly, the higher frequency bands of the spectrum are smaller also. Note the apparent harmonics of the inertial peak in the counter clockwise spectrum.

The drawback with the May 1980 Doppler data is that they are too noisy to resolve the highest frequency motions in the internal wavefield. The spectra sink into noise at about the frequency of the Vaisala cut off. Subsequent improvements to the sonar system have significantly reduced the noise levels. However there is little useful information on the high frequency waves in the May 1980 acoustic data. Fortunately, the CTD system employed during the cruise measured the wavefield from a different perspective. This system has the accuracy to observe high frequency waves. In subsequent sections, the CTD data will be described and the sonar and CTD views of the wavefield will be compared.

Repeated CTD Profiling

As an alternative to measuring the velocity field directly, measurements of the oceanic temperature or density field are often used to infer motions in the sea. Both large scale displacements and small scale distortions of the temperature or

density profiles are of interest. The CTD (conductivity, temperature, depth) instrument is typically used for these measurements. Special purpose CTD's have been constructed for use from FLIP to monitor the small scale motion field. These employ sensors which are more rugged and less expensive than a convential CTD (Occhiello Pinkel, 1976). The vertical resolution is approximately 1 m in temperature and conductivity, five meters in density. The sensors are cycled vertically through 400 m some 700 times a day in the course of a fine scale study of the upper ocean. During the May 1980 trip approximately 12,000 CTD profiles were obtained.

A representative sequence of profiles, obtained over a 24 hour period, is presented in Fig. 6. To avoid visual clutter, only every third profile obtained is plotted. These are separated by 6.6 minutes, rather than the originals 2.2 minute separation. The small scale features in the profiles are termed fine structure. They are, in part, the signature of the vertical straining of the sea by the internal wavefield. Fine structure also results from the horizontal advection or intrusion of water masses of differing temperature and salinity (but similar density) from one region to the next. The difficulty in interpreting temperature measurements is that there is no way to distinguish between the signatures of small scale vertical straining and large scale lateral advection. The former is of direct interest to the O.M.P., the latter is of less interest.

The profiles in Fig. 6 were selected from the larger May 1980 data set because of the diverse phenomena which are illustrated. Note that there are two mixed layers at the start of the observations. The first extends down to 40 m and is colder (and presumably less salty) than the underlying water. The second mixed layer extends to appoximately 90 m. The interface between the two varies in a most intriguing matter during the 24 hour observation period. In the thermocline, between 90 and 200 m there is a strong fine structure signal. During the first few

hours of observations, the water is isothermal (zero temperature gradient) over several depth intervals. At depths below 200 m the fine structure signal is much less apparent. This is not due to a reduction in the number of intrusion or the amount of wave straining. The reduction in the visible signal is a consequence of the fact that the mean gradient which is being distorted is much smaller at great depth.

Repeated profile information has become available only recently. Previously the time evolution of the temperature field was observed only from moored temperature sensors. These produced a far different view of the upper ocean temperature field. In Figure 7 the profile data of Fig. 6 have been used to synthesize a set of fixed depth temperature time series. These are the time histories of temperature as it would have been measured by a thermistor chain with sensors every 6 meters in the vertical.

The irregular temperature fluctuations in Fig. 7 result from the vertical advection of the temperature profile past the reference (sensor) depths. The fluctuations do not look sinusiodal even though the vertical displacement of the wavefield varies much more smoothly in space and time. The irregularity is due to small scale variations in the mean profile. These cause a varying temperature signal ΔT for a given vertical displacement ΔZ. The very fine structure which is the signal in Fig. 6 serves to 'contaminate' the internal wave signal in Fig. 7.

It's interesting to note several quasi-horizontal lines which persist in the Fig. 7 record. These are the signatures of the isothermal layers noted in Fig. 6. Although the layers are advected vertically by the wavefield, their temperature changes but slowly (presumably due to lateral advective effects). Close inspection of the horizontal lines shows that they are actually made up of a variety of short line segments. For example, as a layer is lifted vertically by the wavefield, a

sensor which was reading constant temperature within the layer will find itself outside the layer. Its output will begin to vary in response to wave motion. However a new sensor at the next depth up will now find itself in the zero gradient region. It will assume the constant output, at the same temperature reported by the previous sensor. Thus the constant temperature lines appear as signatures of zero temperature gradient regions. It is easy to see this sort of effect in Fig. 7 because the temperature time series were generated at depths which were closely spaced compared to the typical thickness of the isothermal layers. With very sparse vertical data, as is typically obtained by moored chains or discrete instruments, it is not always possible to unambiguously interpret the data.

A more effective way to use the repeated profile data of Fig. 6 is to follow the depth variations of selected isotherms. Such a plot is presented in Fig. 8. Here, a series of 120 isotherms, each separated by approximtely .1 ^{o}C, are tracked. The dark areas of Fig. 8, where many isotherms are congregated, are regions of high vertical temperature gradient. Where the isotherms are well separated in depth the temperature gradient is small. The isothermal regions in Figs. 6, 7, manifest themselves as the large gaps between isotherms in Fig. 8. Note the gradual transfer of isotherms from below to above the low gradient region centered at 300 m between hours 16 and 24. This indicates a slow temperature decrease of this layer. The water itself is presumably not being cooled. Water of a cooler temperature is being laterally advected under *FLIP* during this period. Another example of this phenomena is seen at 125 m depth between hours one and fifteen.

Away from these regions of intrusive activity the isotherms serve as excellent tracers of the vertical displacement of the internal wavefield. Both low (several cycles per day) and high (several cycles per hour) frequency motions are present. The lower frequency motions have the greatest displacements. The higher frequen-

cies, while smaller, stand out in Fig. 8 due to their remarkable persistance with depth. It has been found that while many internal wave modes might contribute to the low frequency wave field, the first-mode completely dominates the high frequency motions.

The propagation of internal waves is strongly influenced by the distribution of stability (the profile of Vaisala frequency) in the sea. At any given depth, propagating motions can only exist at frequencies below the local Vaisala frequency. Over the 400 m vertical extent of Fig. 8 the Vaisala profile varies from approximately 10 cph (at 100 m) down to 4 cph (at 400 m). The highest frequency waves should be constrained to the upper portions of Fig. 8. An example of this is the very high frequency wave packet which is centered at hour 2 between depths of 140 and 200 m. These die out at depths below 200 m, while the isolated lower frequency 'lump' which occurs at hour 3 penetrates right down to 400 m.

Many other illustrations of this effect can be seen in Fig. 8. The point to emphasize is that the CTD, in contrast with the Doppler sonar, has little difficulty seeing the highest frequency large scale-internal waves which can exist in the sea. It should be cautioned that very small scale motions (1-50 cm) might co-exist with these larger scale motions and still be beyond the CTD's view. However the low frequency view of the wavefield is contaminated by the effects of lateral intrusions. The sonar provides superior information here. It would seem reasonable to combine the two types of sensing systems to get the best possible view of the motions in the upper ocean.

Isotherm Vertical Velocity Spectra

One can process the time series of Fig. 8 in a manner analogous to the Doppler velocity time series to produce power spectra. It is convenient to plot spectra of

vertical velocity rather than vertical displacement. The vertical velocity spectra, like the slant acceleration spectra, are of nearly ω^0 form. Small irregularities in the form are thus easier to see. A representative example is given in Fig. 9. The spectrum is logarithmically averaged, with 18 degrees of freedom in the lowest frequency band, 200 degrees in the highest. It is seen that the spectral variance is confined between the local Vaisala and inertial frequencies. The spectrum is essentially flat between tidal frequency and 1 cph, with a series of irregular peaks that are of marginal statistical significance. Properly recolored, this spectrum would correspond to a displacement spectrum of ω^{-2} form between tidal frequency and 1 cph. Above 1 cph the spectrum rises to a pre-cutoff peak. This corresponds to the high-frequency waves visible in Fig. 8. With only a few crests per group in the time domain, $\Delta \omega / \omega$ is of order 1 in the frequency domain. It is thus not surprising to see that this high frequency peak at 3 cph is $\simeq$ 3 cph wide

It is worthwhile to compare velocity spectra over many depths, as in Fig. 10. Here nine spectra from depths 147-193 m are plotted. The scale is appropriate for the shallowest spectrum. Deeper spectra are offset by successive -5 dB increments. The regularity of the lowest three spectral peaks is striking. The first peak is the semidiurnal tide. The second peak is at the sum of tidal and inertial frequencies. The third peak is the first harmonic of the tide. Note that the power in the internal tide increases by a factor of 10 over the 46 m between the upper and lower measurements.

It is also important to emphasize that the lowest frequency peak in Fig. 10 is not the same low frequency peak which dominates the Doppler velocity spectra. The Doppler spectra are dominated by near inertial motions with a period of nearly 24 hr (at 30°N) while the CTD measurements are dominated by the 12.4 hour tide. Since most of the shear in the sea is at near inertial frequencies, the shear signal is

largely missed by the CTD measurements. The reason for this is not mysterious: the ratio of horizontal to vertical motion in the internal wavefield is a function of frequency. At near inertial frequencies the motion becomes almost purely horizontal. There is no vertical displacement signal for the CTD to detect. At frequencies approaching the Vaisala frequency the motion becomes almost purely vertical. This provides a strong signal for the CTD. Very accurate sonars should be able to detect this high frequency signal also. However, since the high frequency wave velocities are less than approximately 1 cm/sec, the present generation of sonars is unable to resolve them.

Wavenumber-Frequency Spectra of Slant Velocity and Shear

The real strength of repeated profiling data, whether it be doppler acoustic or CTD, is that the observed motions can be filtered/described in terms of their spatial as well as temporal frequencies. Variations of wave energy with frequency might well be different for short waves than for long waves. Changes in wave energy with changing wave length might be different for low frequency waves than for high. The combined wavenumber-frequency spectrum is the appropriate statistical descriptor of these effects. Two dimensional spectral estimates are obtained by Fourier transforming the profile data in both space and time. The squared Fourier coefficients, properly averaged and normalized, constitute the spectral estimate.

Slant wavenumber-frequency spectra for the 45° slant component of velocity in the direction 55° - 235° are presented in Fig. 11. The May 1980 Doppler data were used to form these spectra. The left spectrum gives the distribution of wave energy with wavenumber and frequency for waves with energy propagating upward. The right spectrum describes describes the waves with downward propagating energy. The spectrum is estimated at frequencies from 3×10^{-2} cph, below the inertial frequency, to

1 cph. The wavenumber variations are measured from just below 1 cycle per slant kilometer (one cycle per 700 m vertical) to one cycle per 30 meters. The spectra peak at the near inertial frequency at low wavenumber. Peak values are approximately 10^7 $(cm/sec)^2$ / (cph·cpm). The point to emphasize with these spectra is that the noise level is approximately 10^3 $(cm/sec)^2$ / (cph·cpm). Not only is the large scale near inertial peak well measured but motions at small scale or high frequency, which are a factor of ten thousand times less energetic, also stand out above the noise. This illustrates the enormous capabilities of the acoustic approach for tracking the evolution of small scale less energetic features in the presence of an energetic large scale low frequency shear. Sadly, the highest frequency internal waves have energy levels even smaller than are visible with this system. Improvements made to the Doppler system since the May 1980 cruise will hopefully reduce the spectral noise levels further.

The two dimensional spectra are dominated by a series of ridges at the inertial and tidal frequencies and their harmonics. At low wavenumbers, they have approximately ω^{-1}, to ω^{-2} spectral forms. At low frequency, the wavenumber dependence is approximately k^{-1} out to 1 cycle per 100 m. Beyond that point the spectrum drops extremely rapidly. The slope approaches k^{-6} in the near inertial band! This high wavenumber cutoff in the spectrum is one of the most significant discovereis of the program to date.

The cutoff is better visualized when the spectra are heavily smoothed in frequency, so as to remove the effect of the harmonic ridges. A smoothed version of Fig. 11 is presented in Fig. 12. Here the near inertial cutoff at low frequency is seen to merge continuously with a higher frequency spectral shoulder. The high wavenumber cut off suggests that waves of vertical scale less than 60 m (slant scale less than 100 m) do not exist as either free or force motions in the sea. There are

a variety of possible explanations for this phenomena, none of which are certain. The cutoff is perhaps a key clue in the mystery of how small scale motions interact with large. A proper physical interpretation of this feature is vital.

From the wavenumber frequency spectrum of velocity, a wavenumber frequency spectrum of shear can be obtained. Such a spectrum is presented in Fig. 13. The shear spectrum has the same frequency dependence as the velocity spectrum. The wavenumber dependence, however, is boosted by a factor of approximately k^2 relative to the velocity spectrum. This has the effect of emphasizing the largest wavenumbers. At low frequency, up to 10^{-1} cph, the May 1980 shear spectrum is band limited in wavenumber. Shear variance is concentrated at slant wavelengths between 100 m and 1 km. At high frequencies the shorter scales progressively dominate the spectrum. This high wavenumber dominance at high frequency stands in direct contrast to the observation in Fig. 8 that the lowest mode (longest length scales) dominate the high frequency wavefield. The source of this high wavenumber shear variance is not currently understood. It is seen in measurements from conventional current meters as well as Doppler sonars. Traditionally it is ascribed to fine structure contamination in the velociy data. (Muller, Olbers Willebrand, 1978). Understanding this source of high wavenumber shear variance represents a major research goal.

The Isotherm Wavenumber Frequency Spectrum

To emphasize the discrepancy between the velocity and isotherm displcement series at high frequency, a wavenumber-frequency spectrum of isotherm vertical velocity is presented in Fig 14. January 1977 data is used to form this estimate. Here both upward and downward propagating motions are presented together, at positive and negative vertical wavenumbers. Zero vertical wavenumber corresponds to the average vertical velocity signal over the 342 m depth interval analyzed here. At all

frequencies the zero wavenumber band has the dominant energy. This is particularly true for frequencies below the 12.4 hour tide. The slow drift of the temperature sensors affects the readings at all depths similarly. Hence it makes a large contribution to the zero wavenumber low frequency signal. In spite of the sensor drift, the M2 tide can be seen at a variety of wavenumber bands. The most visible signal in Fig. 14 is the large peak at zero wavenumber which occurs at high frequency, just below the Vaisala cutoff. This peak corresponds to the high frequency low mode motions that are so apparent in Fig. 8. The disagreement between velocity and isotherm measurement of the high frequency wavefield is well summarized in the comparison of Fig. 11 and Fig. 14. In the slant velocity spectrum, the higher the frequency, the more gentle the wavenumber dependence. In the vertical velocity spectrum the spectral slope increases with increasing frequency.

Conclusions

Over the last decade considerable effort has been expended at MPL to develop the capability to measure small scale motions in the sea in the context of the larger scale background. Considerable progress has been made, as evidenced by the spectra of Figs. 11, 14. However, the technical difficulties have not been completely overcome. The physical processes remain imperfectly understood. The disagreement between vertical velocity measurements with CTD's and horizontal velocity measurements with conventional current meters or Doppler sonars is an example of the state of our present understanding. It is not clear whether this is a measurement problem (fine structure contamination) or a clue to the true physics of the upper ocean.

The CTD is an appealing instrument to use in these studies. It is no longer considered an exotic device and the interpretation of the measurements is straightforward (Figs. 6, 7, 8). The CTD clearly has the sensitivity to resolve high

frequency internal wave motions. Yet it cannot sense the low frequency shear field in which the higher frequency motions must propagate, as the low frequency shears are associated with almost no vertical displacement. This becomes an increasingly larger problem as one moves to more polar latitudes and the coriolis frequency decreases. At 75°N the vertical signature of the M2 tide disappears (F = 12.4 cph). Is one justified in extrapolating low latitude intuitions into polar regions in the absence of direct shear measurements? A related problem at high latitude is that the water is often isothermal to great depths, due to wintertime convection. The CTD provides no useful small scale information in such conditions.

Direct measurements of the velocity field are clearly preferred for use in regions where the water might be isothermal. Yet the existing generation of moored or profiling instruments is not adequate to resolve the smaller scale internal wave motions at high frequency.

Since the May 1980 cruise the MPL Doppler sonar system has been considerably improved. The velocity precision has been increased to the point where high frequency internal wave motions might be monitored. A major sea test, MILDEX, will be conducted in Fall 1983. At that time it is hoped that the discrepancy in the measurement of high frequency low mode internal will be resolved.

At this point the very issue is to understand how the small scale high frequency motions interact with the background shear. These small scale motions are currently measured only by special purpose microstructure devices. However, they are well within the measurement capabilities of so-called pulse to pulse coherent Doppler sonars. Such sonars have maximum range of a few tens of meters in contrast with the 1.5 km of the present incoherent sonars. However range resolution can be as small as a few centimeters. Measurements precise to 1 Hz in Doppler resolution can be obtained every few seconds! There has been no development history of these

devices in the Navy community, with the exception of a proof of concept demonstration done at MPL in the mid 1970's. This should be changed.

References

Muller, P., D. J. Olbers and J. Willebrand, 1978, The IWEX spectrum, J. Geophys. Res., 83, no. C1, 479-499.

Occhiello, L. M. and R. Pinkel, 1976, Temperature measurement array for internal wave observations, in Oceans '76, MTS, IEEE, 20E1-20E7.

Pinkel, R., 1975, Upper ocean internal wave observations from FLIP, J. Geophys. Res., 80, 3892-3910.

Pinkel, R., 1981a, On the use of Doppler sonar for internal wave measurements, Deep-Sea Res., 28A, no. 3, 269-289.

Pinkel, R., 1981b, Observations of the near-surface internal wavefield, J. Phys. Oceanog., 11, no. 9, 1248-1257.

Weller, R. A., 1981, Observations of the velocity response to wind forcing in the upper ocean, J. Geophys. Res., 86, no. C3, 1969-1977.

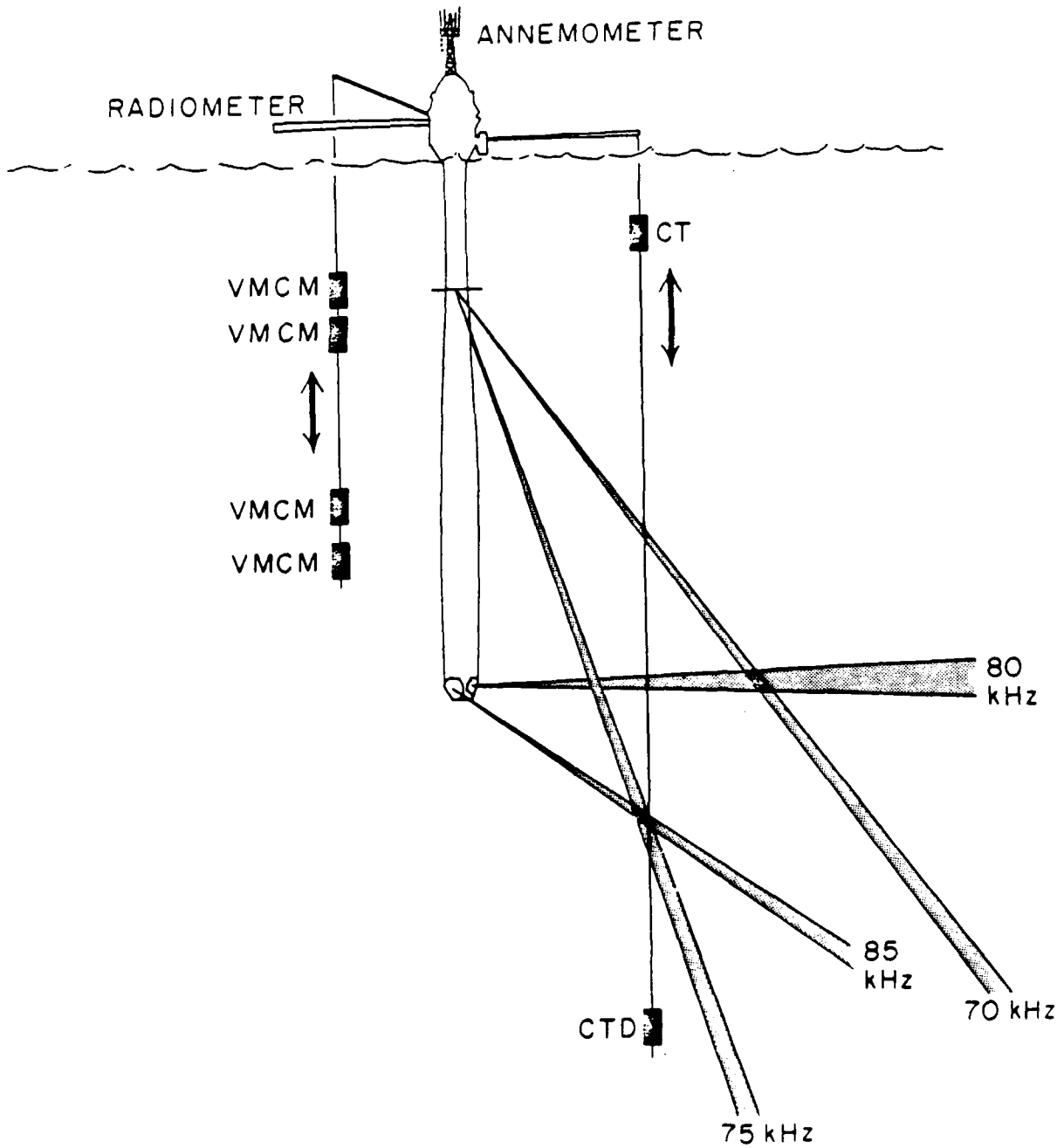

Fig. 1. Schematic of the May 1980 FLIP Experiment. The position of the four Doppler sonar beams is given by the grey areas. The VMCM current meters were generated by Dr. Robert Weller of Woods Hole.

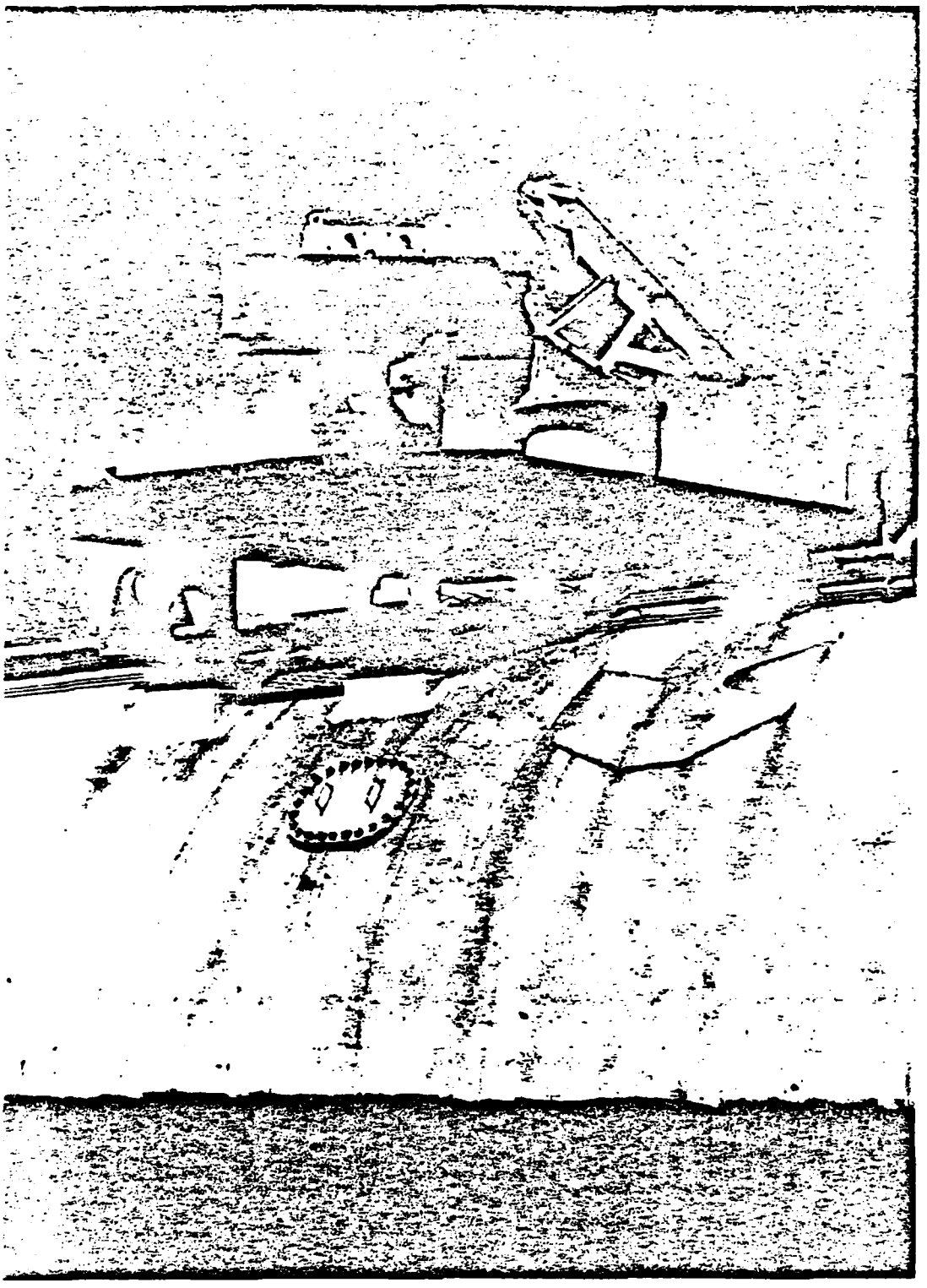

Fig. 2. The 45° downward slanting Doppler sonars used to obtain the velocity and shear profiles. The sonars operate at frequencies of 70 and 75 kHz, at a peak power of 8 kW. The acoustic beam width is less than 1° in the vertical and approximately 2° in the horizontal.

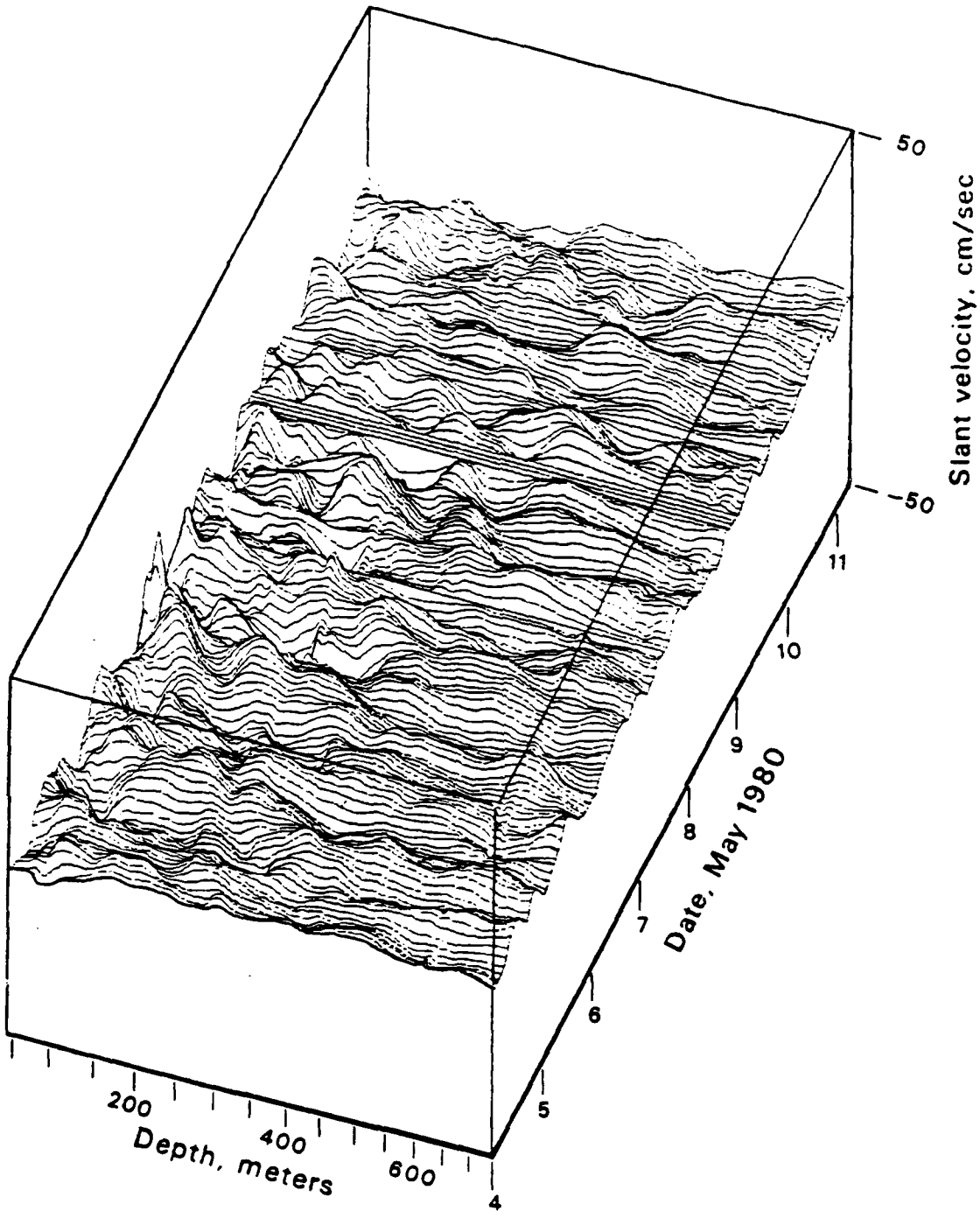

70 kHz VELOCITY PROFILE: 7 DAY RECORD

Fig. 3. Hourly profiles of velocity vs. depth and time obtained with the 70 kHz sonar. The first week of the May 1980 data set is presented.

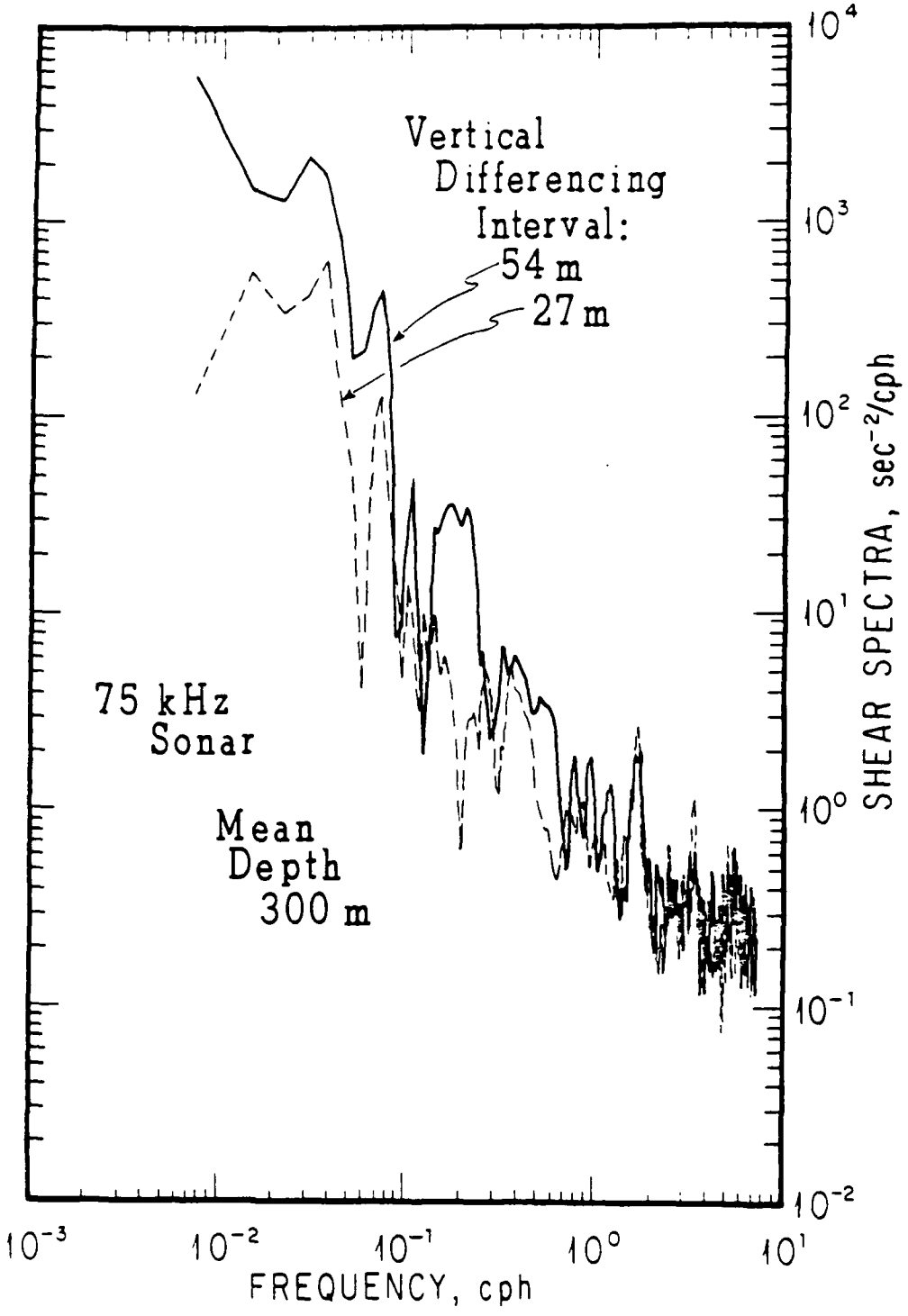

Fig. 4. Spectra of velocity shear obtained by differeing the Doppler velocity range-time series (Fig. 2) with respect to range. Spectra are presented for a depth centered at 300 m with differing intervals 27 m and 54 m. The low frequency form of the spectrum with 54 m separation is very nearly ω^{-2}. With the smaller separation the slope is more gradual. The spectra fall into the noise at approximately 2 cph.

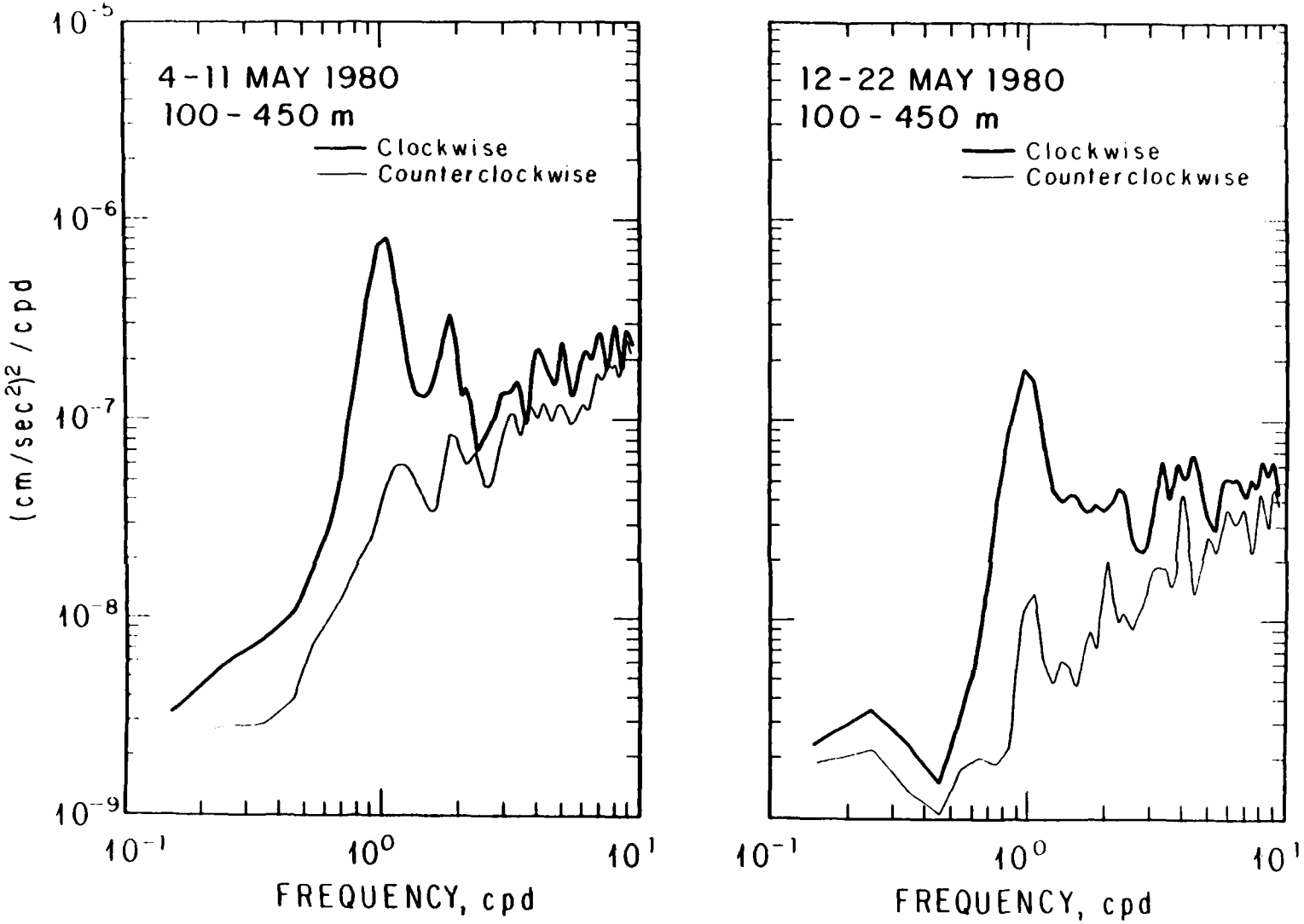

Fig. 5. Depth averaged rotary slant acceleration spectra, 3-11 May and 12-22 May 1980. Eight spectra, at 50 m intervals between 100 and 450 m, are combined to form each spectral estimate. There are nominally 64 degrees of freedom below 2.5 cpd, 102 degrees of freedom below 5 cpd. The actual statistical stability of this estimate is less than indicated by the number of degrees of freedom, as adjacent depths are not statistically independent. The clockwise spectra are indicated by the heavy lines.

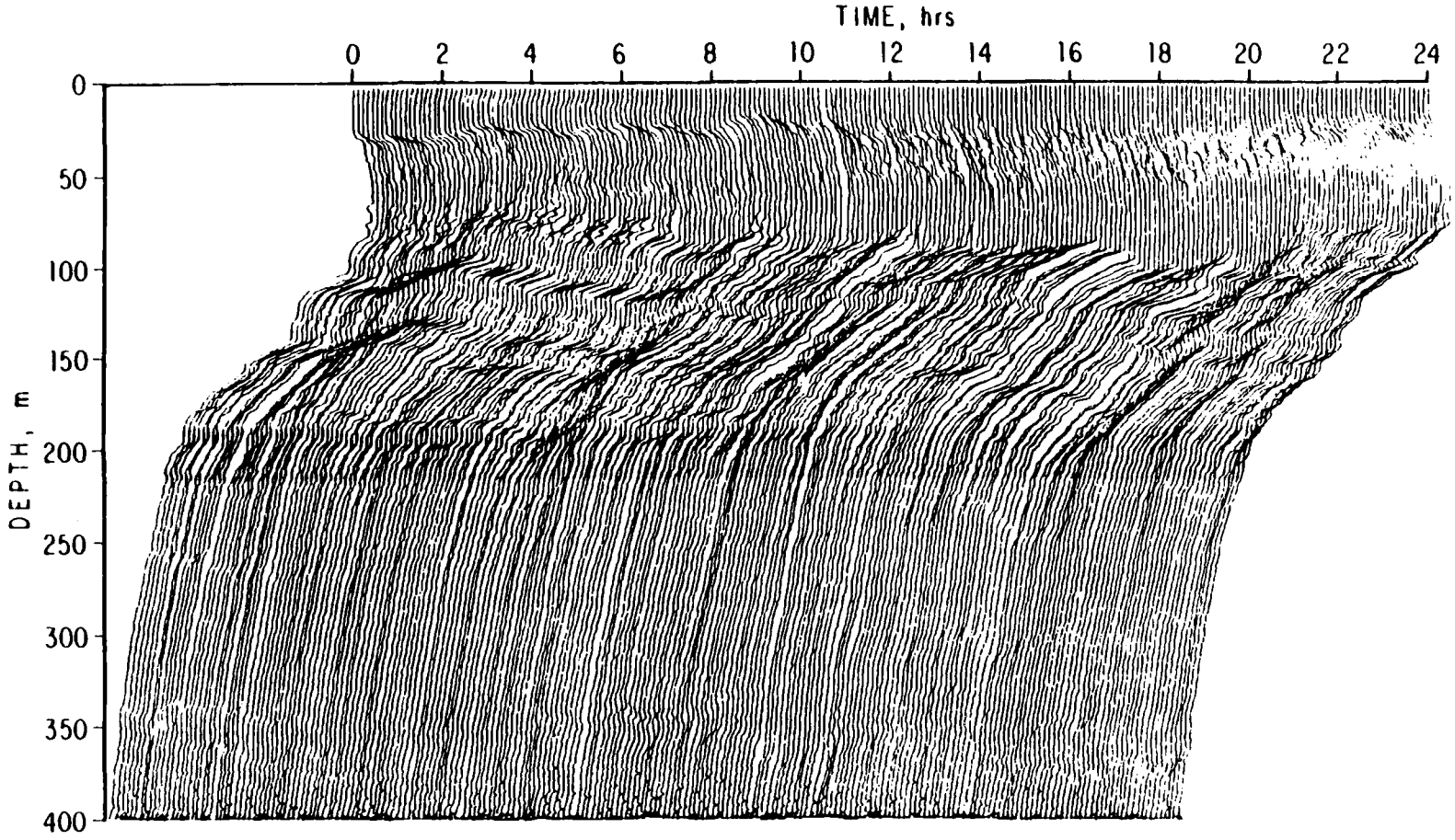

Fig. 6. A 24-hour sequence of temperature profiles obtained during the May 1980 FLIP cruise. Profiles are separated by approximately 6.6 minutes.

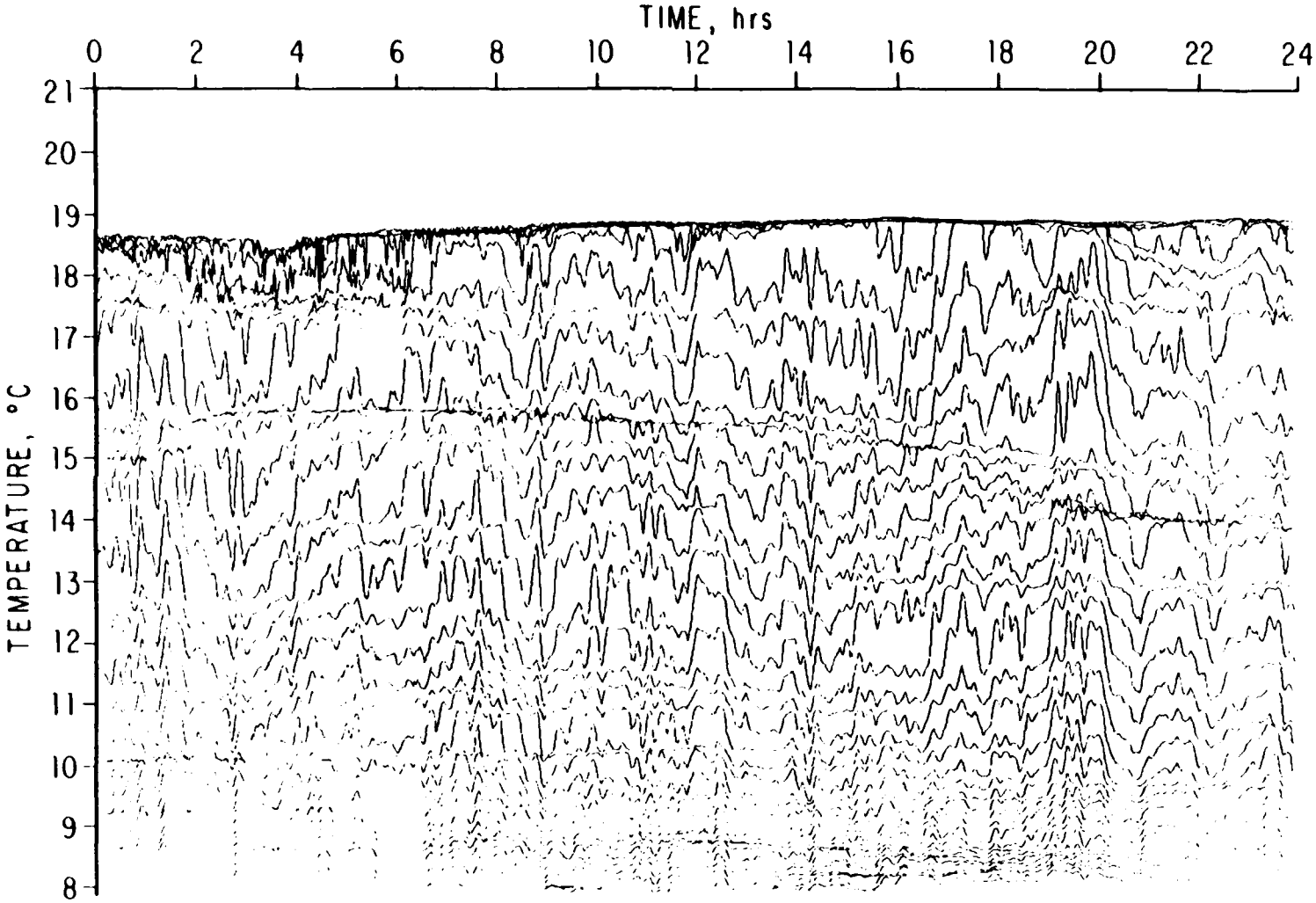

Fig. 7. Temperature fluctuations as a function of time at a series of fixed depths for the same time interval as in Fig. 6. The temperature fluctuations are tracked at a set of depths separated by 6 m over a depth range of 70 to 400 m. The quasi horizontal lines in these data correspond to nearly isothermal regions in Fig. 6.

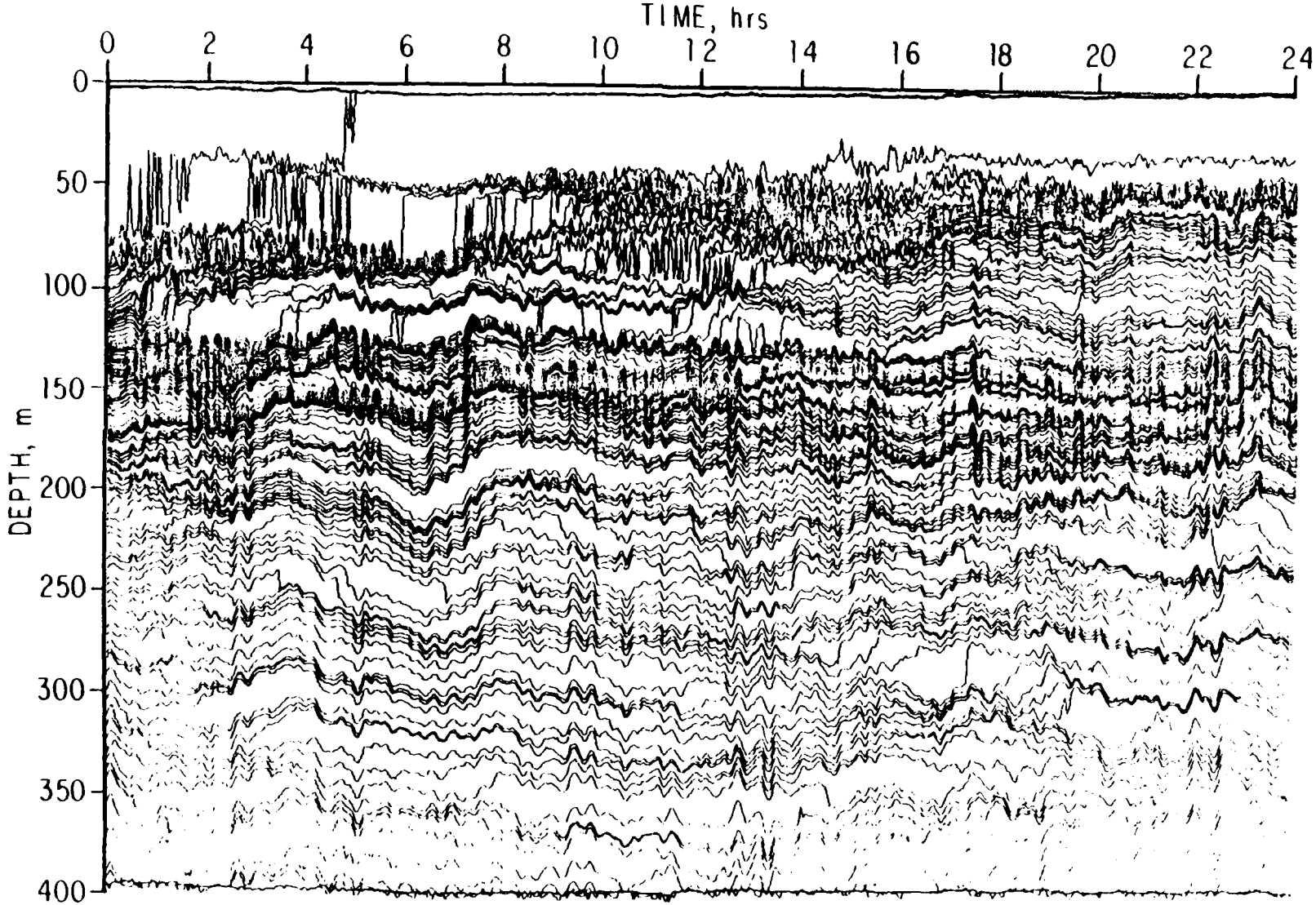

Fig. 8. Isotherm displacement time series for the same data interval as in Figs. 6, 7. The depths at which a set of 140 different temperatures occur are tracked from profile to profile to produce this view of the internal wavefield.

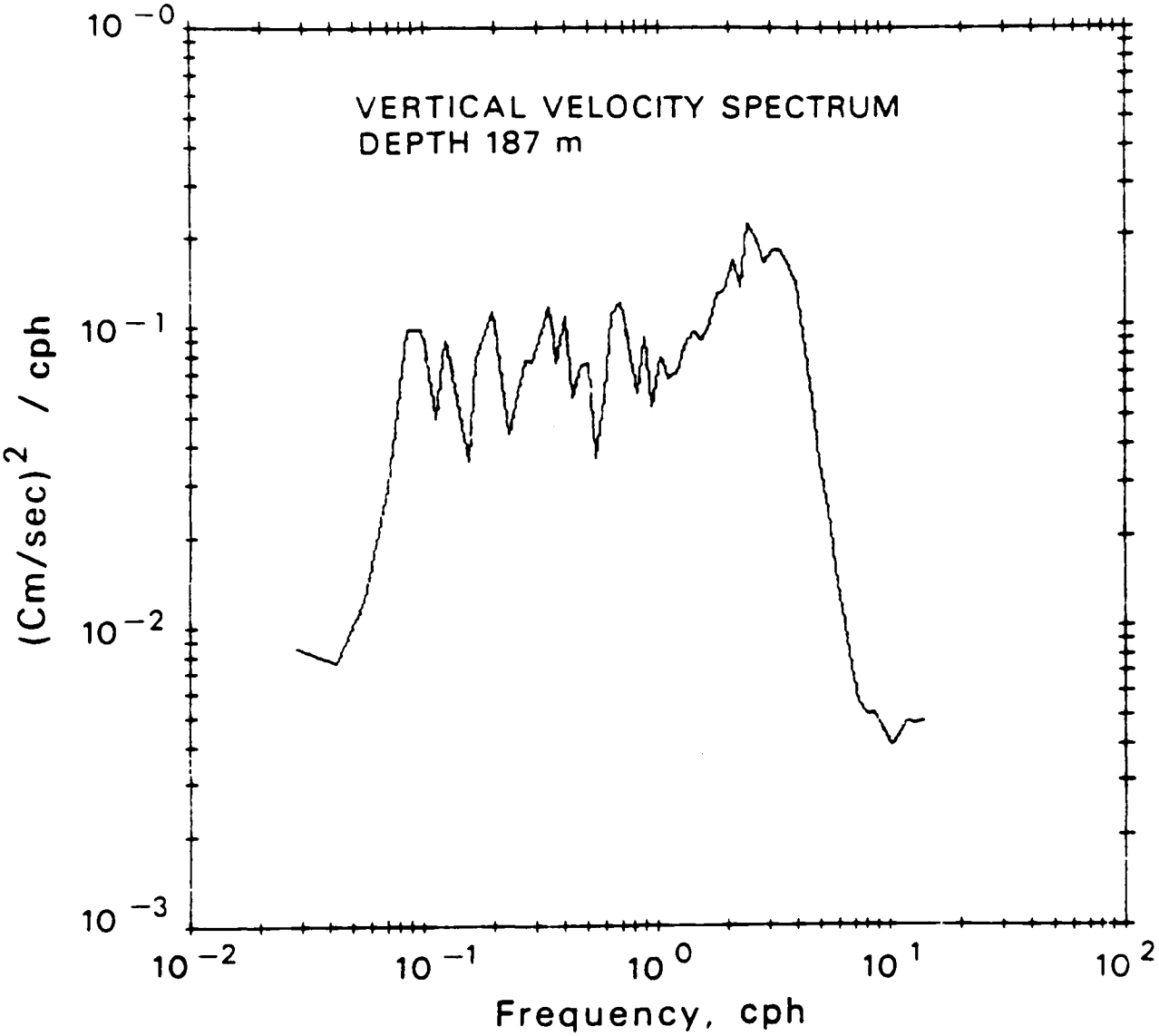

Fig. 9. A power spectrum of vertical velocity obtained from the profiling CTD. The spectrum is sharply confined between the inertial and Vaisala frequencies. The peak at the low frequency end of the spectrum is the 12.4 hr tide. The broad high frequency peak corresponds to low mock high frequency motions visible in Fig. 8.

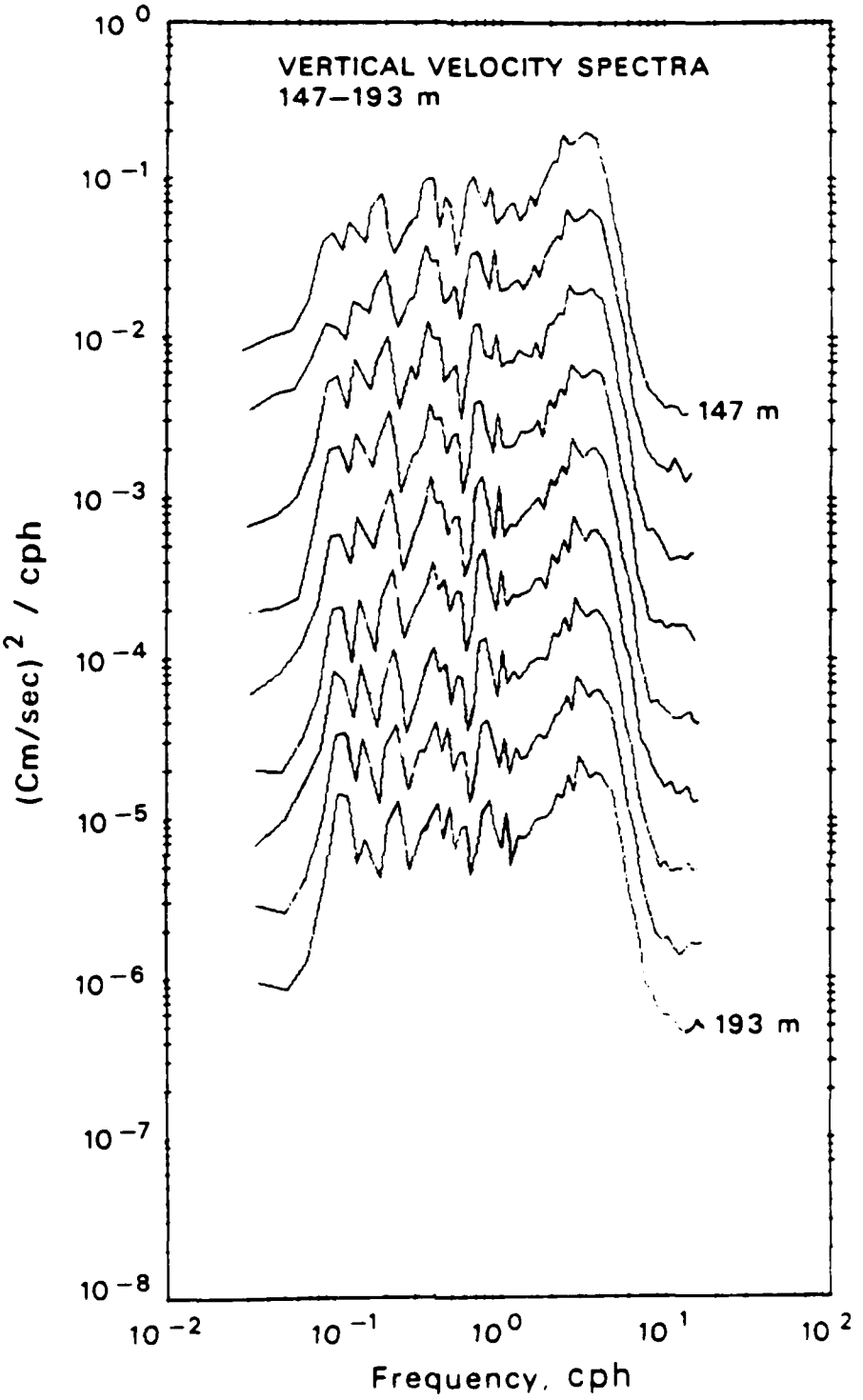

Fig. 10. A sequence of nine vertical velocity spectra over the region 147-193 m. The scale for the uppermost spectra is correct. Subsequent spectra are displaced by -5 dB. Solid arrows indicate the frequencies of the M2 tide and its first three harmonics. The dashed arrow marks the sum of inertial and tidal frequencies.

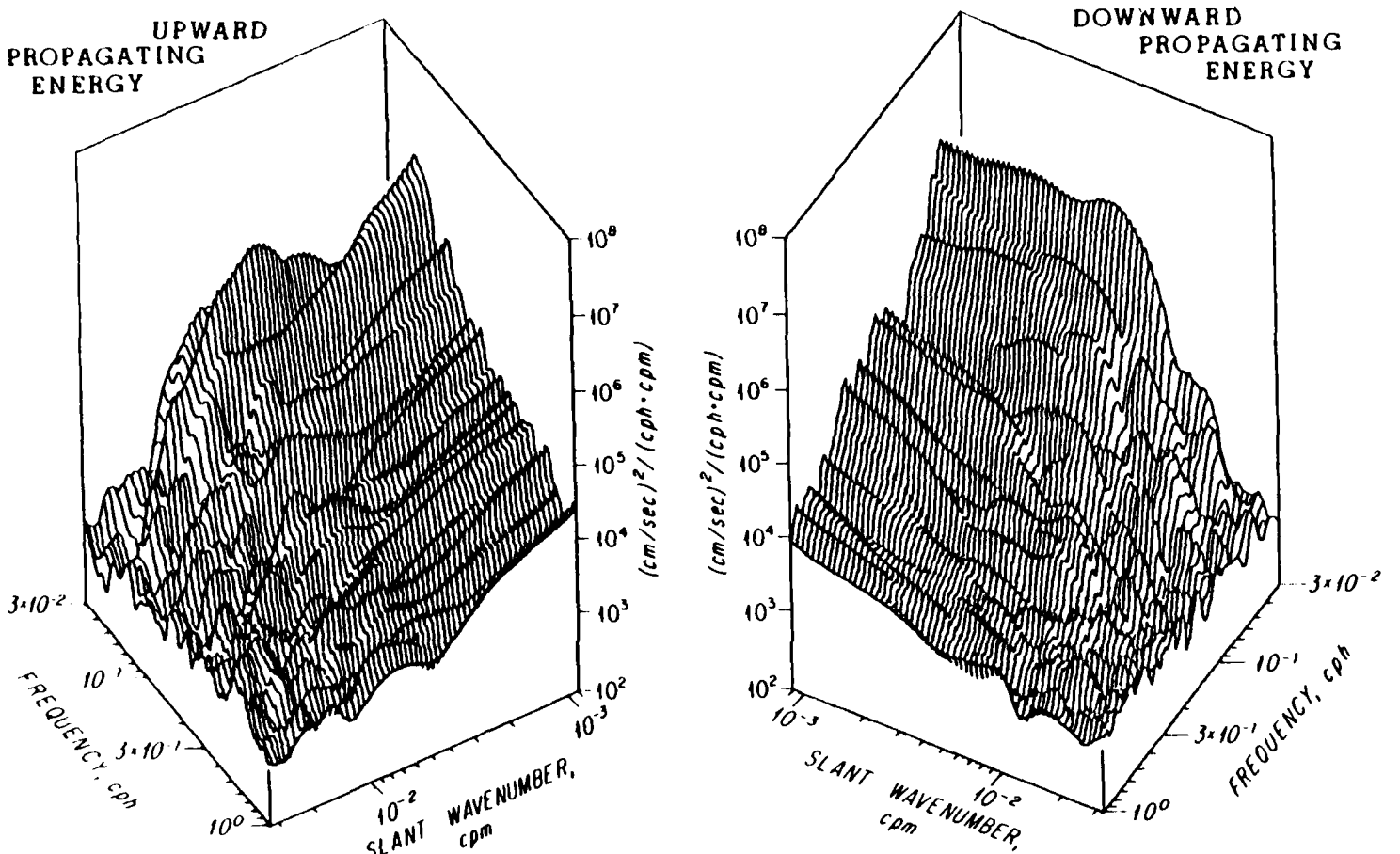

13-23 MAY 1980
29°-30° N, 124° W
VELOCITY IN DIRECTION 55° – 235°
70 kHz SONAR

Fig. 11. The wavenumber-frequency spectrum of the oceanic velocity field, as measured by the 70 kHz 45° downward slanting Doppler sonar. The low-frequency low wavenumber peak corresponds to near-inertial motions. The high-frequency high wavenumber motions are seen to have some ten thousand times less energy. It is necessary to further reduce the overall spectral noise level in order to get a clear view of this portion of the spectrum. Note the high wavenumber cut-off visible at low frequency.

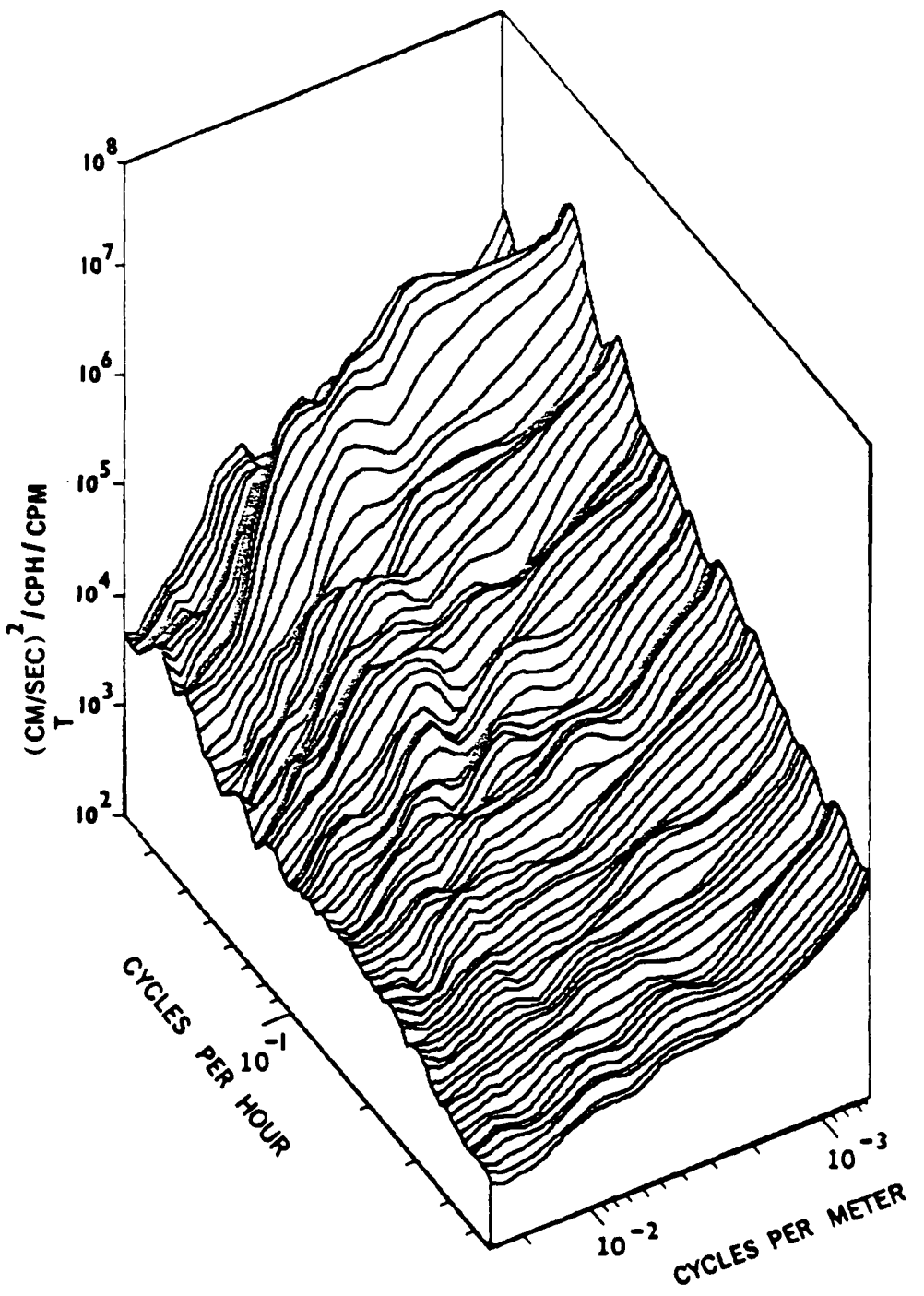

Fig. 12. A smoothed version of the spectrum presented in Fig. 11. When the ridges, which might correspond to harmonics of the tidal and inertial frequencies, are smoothed away, the low-frequency spectral shoulder and cut-off are seen to exentd to higher frequencies.

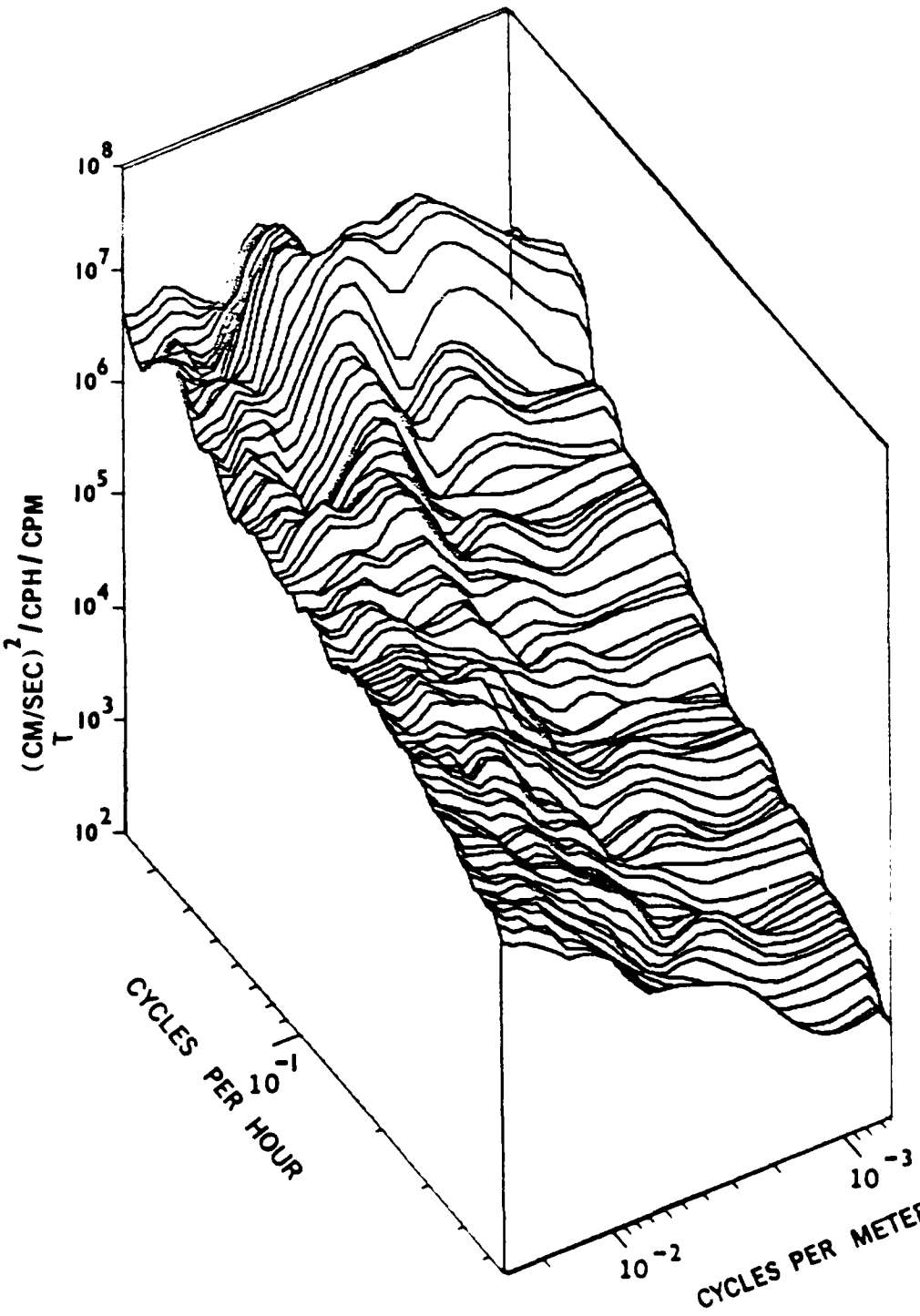

Fig. 15. A smoothed wave number frequency spectrum of the shear in the upper 700 m of the sea. This is obtained by differentiating the velocity profiles with respect to range, or alternatively weighting the 2-D velocity spectrum by a factor of k^0. The spectrum is band limited in wavenumber at low frequency, but becomes progressively more "blue" at higher frequency.

VERTICAL VELOCITY SPECTRUM AS A FUNCTION OF VERTICAL WAVENUMBER AND FREQUENCY

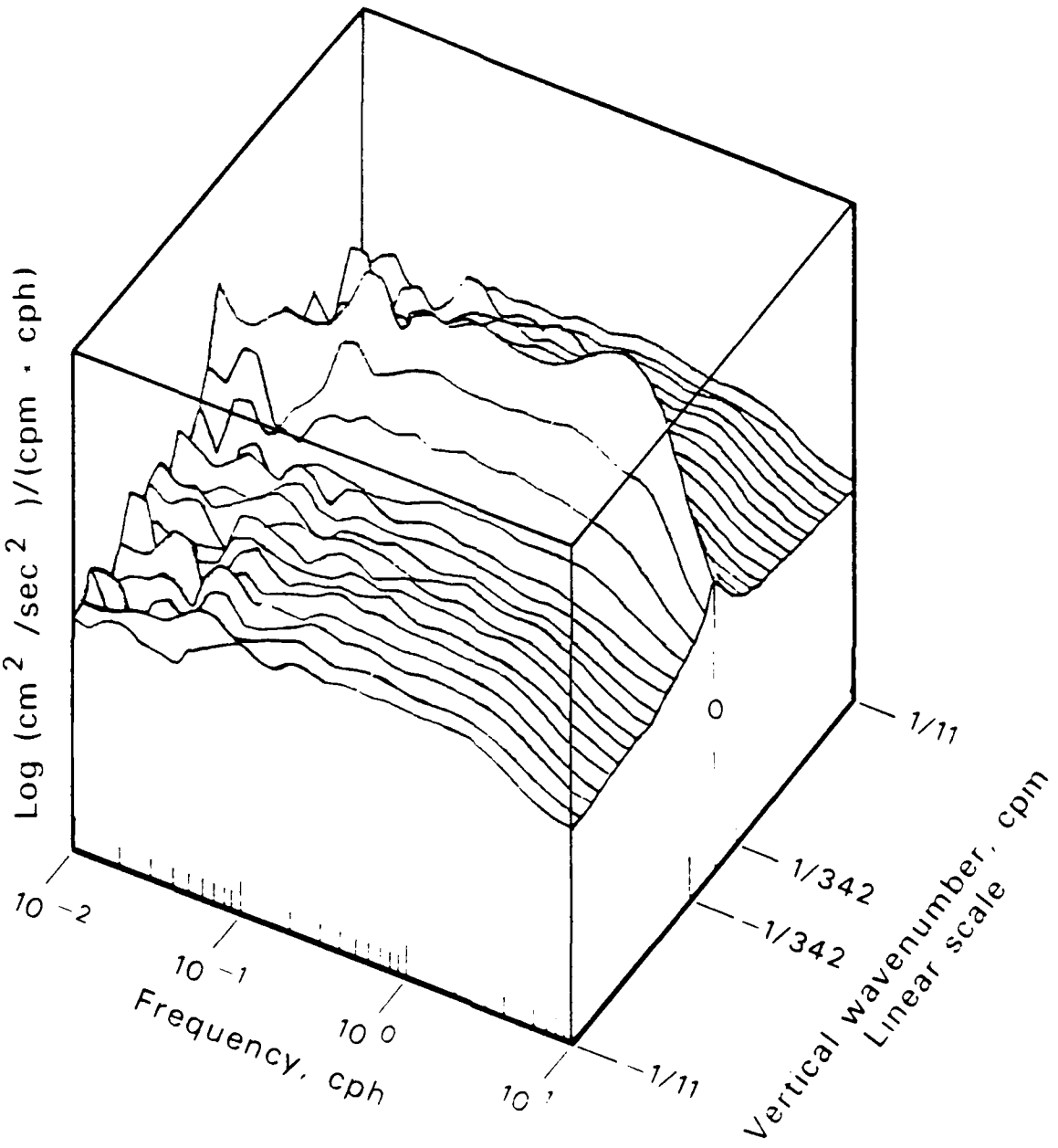

Fig. 14. A wavenumber-frequency spectrum of vertical velocity obtained with the profiling CTD. In contrast with the Doppler slant velocity spectrum, the vertical velocity spectrum is dominated by high-frequency motions. The spectrum is more strongly dominated by the longest vertical wavelengths at high frequency than at low. This disagrees with the picture obtained from the Doppler sonar (Fig. 11).

APPENDIX C

Reprinted from JOURNAL OF PHYSICAL OCEANOGRAPHY, Vol. 14, No. 8, August 1984
American Meteorological Society
Printed in U. S. A.

Doppler Sonar Observations of Internal Waves: The Wavenumber-Frequency Spectrum[1]

R. PINKEL

University of California, San Diego, Marine Physical Laboratory of the Scripps Institution of Oceanography, La Jolla, CA 92093

(Manuscript received 7 November 1983, in final form 23 April 1984)

ABSTRACT

In May 1980 an 18-day sequence of velocity profiles of the top 600 m of the sea was collected off the coast of Southern California. The measurements were obtained using a pair of Doppler sonars mounted on the Research Platform FLIP. From these data, estimates of the wavenumber–frequency spectrum of the oceanic internal wavefield are obtained. The spectra are characterized by a series of ridges, which occur at near-inertial and tidal frequencies as well as higher harmonics and sums of these fundamentals. The ridges run parallel to the wavenumber axis. There is a pronounced near-inertial spectral peak. The near-inertial motions are dominated by a few identifiable wave groups. There is a net downward energy propagation in the near-inertial frequency band. The vertical-wavenumber dependence of the spectrum is decidedly asymmetric in this region. The asymmetry extends to five times the inertial frequency, making much of the so-called continuum asymmetric. A high-wavenumber cutoff at approximately 60 m vertical wavelength extends from the inertial frequency to approximately 5 cycles per day (cpd). The changing form of the wavenumber dependence of the spectrum with frequency frustrates any simple attempt to assign a scale wavenumber bandwidth to the spectrum. The total variance of the downward propagating motions exceeds that of the upward, primarily because of an excess of downward near-inertial energy. Surprisingly, the net energy transport of the wavefield is upward, of the order 0.003 W m^{-2}. The upward flux results from an excess of high-frequency (5–60 cpd) upward propagating waves. Although these have much less variance than the downward propagating near-inertial waves, they have a far greater vertical group velocity.

1. Introduction

Internal waves are found throughout the ocean interior. They are properly described by a four-dimensional wavenumber–frequency spectrum $E(\bar{k}, \omega)$. To resolve this spectrum a set of measurements dense in both spatial and temporal separations is necessary. Such measurements are difficult to obtain. In 1972 Garrett and Munk proposed a simplified model spectrum which would allow a consistent picture of the wavefield to be pieced together from a variety of more manageable observations. Their primary assumption is that a single spectral form describes the open ocean wavefield globally. A number of other strong assumptions are made to produce a simple, useful model which is consistent with the governing physics and existing observations. The assumptions include:

- The linear internal-wave dispersion relation is valid.
- The effects of discretization into vertical normal modes can be neglected. An experiment with a vertical aperture of twice the ocean depth would be needed to resolve a spectral gap between two adjacent vertical modes. An "equivalent continuum" is proposed instead.
- The spectrum is horizontally isotropic and vertically symmetric.
- The spectrum is separable in frequency and wavenumber. The frequency dependence of the spectrum does not change with wavenumber. The vertical-wavenumber dependence does not change with frequency, except perhaps for a bandwidth scale factor.

During the 1970s the model was updated several times to refine the parameterization (Garrett and Munk, 1975, 1979). However, the underlying assumptions have not been altered. Also during this period observational methods have been improved. Techniques have been created to provide multidimensional measurements of the wavefield. At Scripps, Doppler sonar technology was developed for this purpose. A sonar provides an estimate of the component of oceanic (scatterer) velocity parallel to the sonar beam as a function of range. Maximum ranges of order 1 km can be achieved, with 20 m range resolution (Pinkel, 1981a).

In May of 1980 four such sonars were mounted on the research platform FLIP and operated for an 18-day period in the deep sea approximately 400 km west of San Diego. Two of the sonars, depressed 45° downward and at right angles to each other, obtained slanting profiles of the velocity field to a depth of 600 m. These repeated profiles can be Fourier transformed in both time and depth to provide an estimate of the

[1] Contribution of the Scripps Institution of Oceanography, new series.

slant wavenumber–frequency spectrum $E(k, \omega)$. At frequencies low compared to the local Väisälä frequency N this spectrum is related to the vertical wavenumber spectrum of horizontal velocity by a multiplicative constant. Combining data from the two sonars, a rotary wavenumber–frequency spectrum can be estimated. These spectral estimates are resolved in sufficient detail that interesting observations can be made without the assistance of a specific spectral model.

This paper discusses the wavenumber–frequency spectra estimated from the downward-slanting-sonar data. A companion paper (Pinkel, 1983) describes these data in the depth–time and depth–frequency domain. The experiment is reviewed briefly in the next section. The method of spectral analysis is then described and the wavenumber-frequency spectra are presented. The remainder of the paper consists of two extended discussions of the spectra. Attention will be focussed on the following issues:

1) The wavenumber dependence of the spectrum. How valid is the G-M assumption of separability?

2) The scale bandwidth of the spectrum. How does it vary with frequency? How can it be related to coherence if the separability assumption is not accurate?

3) The vertical symmetry of the spectrum. Which frequency bands of the spectrum exhibit significant asymmetry in vertical wavenumber?

The second discussion, which compares these measurements with other works, concludes the paper.

2. Measurements

The observations were made during an 18-day period in May 1980 as FLIP drifted southward in the California Current. Measurements commenced at approximately 30°50′N, 124°0′W and concluded at 28°40′N, 124°0′W, approximately 200 km to the south. During this period FLIP's azimuthal orientation was regulated by a thruster system linked by a standard auto-pilot to the ship's gyrocompass. This enabled azimuthal stability in the orientation of the sonar beams. Heading stability was maintained to ±3° for the majority of the observing period. Excursions up to ±30° occurred occasionally, during squalls or major wind shifts.

Equipment on board FLIP included a profiling-current-meter system (Weller, 1984) a profiling CTD (Pinkel, 1975), the sonar system, and a number of environmental sensors.

The downward slanting Doppler sonars were mounted at a depth of 38 m and operated at frequencies of 70 and 75 kHz. During the course of the experiment the 70 kHz sonar was nominally directed toward 235° (True), while the 75 kHz sonar pointed toward 145°. Accurate slant-velocity estimates were achieved over the depth range of 80 to 600 m. Maximum range was limited by electronic noise in the sonar receiver system. A more complete description of the experiment is presented by Pinkel 1983.

The response of the sonar measurements to the internal wavefield is complicated by the geometric properties of the instruments, which only measure the component of velocity parallel to the beam, and by those of the wavefield (Pinkel, 1981a). If the downward slant angle of the sonar beam is steep compared to the slope of the internal wave rays, a vertical profile of the wavefield is effectively achieved. Since internal-wave ray slopes depend on wave frequency, and steepen with increasing frequency, only the lower-frequency waves sensed by a fixed sonar have this simple interpretation. Given the 45° downward angle of the sonar beams used in 1980, effective vertical profiles are achieved for motions of frequency $\omega \ll N/\sqrt{2}$. For simplicity in interpretation, only frequencies below this value are considered in the present analysis.

To illustrate the nature of the data set, a series of hourly averaged profiles of slant velocity is presented in Fig. 1 for the first week of the cruise. Flat spots in

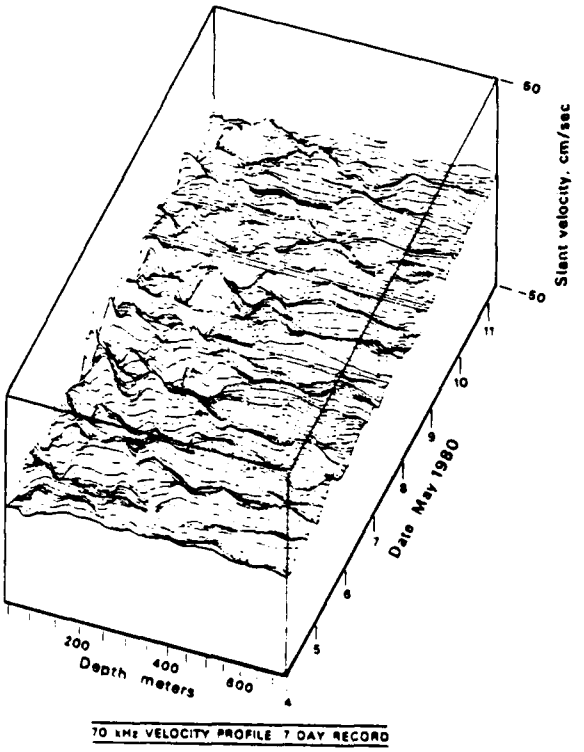

FIG. 1. A one-week series of hourly averaged velocity profiles obtained from the 70 kHz sonar. The depth scale and the velocity magnitudes have been Väisälä-stretched. Near-inertial waves dominate the field of motions. Flat spots in this deformed-surface record correspond to periods when the sonar was not operating.

the figure correspond to intervals when the sonar was not operating. Near inertial motions dominate the velocity field. Smaller scale higher-frequency motions are also present, although more difficult to track in the confused near-inertial sea. Much of the irregularity of Fig. 1 disappears when the data are plotted differently. Figures 3 and 4 of Pinkel (1983) present these identical data in the form of color contour maps of velocity and shear. In these representations considerable structure can be seen in the near-inertial motions.

3. Spectral analysis

The acoustic data were divided into two segments, corresponding to observation intervals of 4–11 May and 12–23 May. During the first observing interval, pulses of 32 ms duration were transmitted. These resulted in a range resolution of 24 m and a depth resolution of 17 m. (Subsequent averaging in range degraded this nominal resolution, however). Average velocity profiles were formed at five-minute intervals. During the second observing period, 40 ms pulses were transmitted, corresponding to range and depth resolution of 30 m and 21.4 m respectively. Average profiles were formed at 5.6-minute intervals.

The velocity data series were first differenced in time, and the series means were removed. Gaps in the time records were zero-filled. The time series were then multiplied by a triangular data window and digitally Fourier transformed. Complex "depth series" were obtained in 1200 frequency bands, at frequency increments of 0.1 cycles per day (cpd) for both data collection intervals.

An attempt was made to reduce the effects of refraction due to depth variations in Väisälä frequency using the now standard technique of WKB-stretching. The velocity Fourier coefficients were weighted by the factor

$$W = C_1[N^2(z) - \omega^2]^{-1/4},$$

where the constant C_1 was chosen such that the integral W^2 over the depth range to be Fourier transformed was equal to unity. Similarly the depth was stretched such that

$$dz_s = C_2(N^2(z) - \omega^2)^{1/2}dz.$$

The constant C_2 was chosen such that the total vertical aperture of the array was the same whether in stretched or unstretched units.

In each frequency band, the complex depth series was WKB-weighted and first differenced in depth. The complex depth mean was then removed and the series was multiplied by a triangle window. Note that the data are not equally spaced in "stretched depth" as they originally were in actual depth. A (slow) digital Fourier transform was again employed to implement the Riemann sum

$$A(k, \omega) = \sum_{z=z_0}^{z_{max}} \mathrm{WDO}(z)A(z_s, \omega)e^{-ikz_s}dz_s.$$

Here, WDO represents the triangle window, and $A(z_s, \omega)$ is the depth series of weighted first differenced Fourier coefficients, with mean removed. The maximum depth, z_{max}, was adjusted frequency-by-frequency such that only depths where $\omega < N(z_{max})$ were transformed. Typically 45 depths were included in the vertical transform. Fourier coefficients were produced at 1/1500 cpm increments in wavenumber.

An analytical model of the local Väisälä profile was used in the WKB stretching

$$N(z) = N_0e^{-bz},$$

where N_0 = 6 cph and b = 1 km^{-1}. Other models of the Väisälä profile were tried, as well as the actual measured profile. The resulting spectral estimates proved quite insensitive to the particular form of the Väisälä profile used and to the details of the stretching.

The ability to produce good spectral estimates is not, however, a confirmation of the validity of the WKB stretching technique. A more appropriate test is to generate numerical solutions to the internal wave equation with a variable $N(z)$ and then to see how well the WKB stretching procedure deforms these solutions back into sinusoids. This has been done (Pinkel, 1974). It was found that the WKB procedure does a poor job, particularly for the shorter vertical wavelengths, when realistic (i.e., irregular) upper ocean Väisälä profiles are considered. One would expect the WKB-procedure to work best for the smallest-wavelength motions. Indeed, the error per wavelength is less for the smaller wavelengths. However, the total error over some fixed vertical aperture is *greatest* for the small-wavelength motions, as more wavelengths occur within the aperture, and the errors accumulate. The WKB-analysis employed here must be considered nonoptimal, although adequate for the issues to be addressed.

It is particularly convenient to use the digital (slow) Fourier transform for this work. Fourier coefficients can be produced at the same frequency and wavenumber intervals for both data collection periods, regardless of the depth–time spacing of the original data, and the length of the original records. Aspects of the WKB stretching can be implemented in the Fourier transformation process itself. Note that adjacent wavenumber and frequency bands are not independent, as it is the case when the fast Fourier transform is applied to un-windowed data. In particular, the spectral estimates here are heavily over sampled in wavenumber. The "slant" resolution of the array is of the order 1/750 cpm while spectral estimates are produced at 1/1500 cpm intervals.

The complex Fourier coefficients are squared, averaged, recolored, and normalized to produce the

various (two-sided) spectral estimates. Data from both observing intervals are averaged together to improve the statistical precision of the estimates. Separate wavenumber-frequency spectra have been estimated using data from each of the slant sonars. In addition, these data have been combined to produce estimates of the rotary wavenumber-frequency spectrum (Gonella, 1972). The rotary analysis overlooks the fact that the measurements from the two sonars are closely spaced at shallow depths but diverge as depth increases. At a depth of 600 m the sonar beams are separated by nearly 1 km. The effect of this separation is not severe. Expected differences in wave velocity over 1 km horizontal separation are of the order of a few cm s^{-1}. However, since the velocity differences are coherent with the signals being measured, this error cannot be modeled as a random noise. Discussion in the text is confined to the 70 and 75 kHz wavenumber–frequency spectra. The rotary spectra are similar in most respects and are documented, primarily through figures, in the Appendix.

Given the short duration of the experiment the spectra represent an essentially deterministic description of the specific low-frequency (near-inertial) wave groups that passed under FLIP during the cruise. At high frequencies, the statistical significance of the spectral estimates becomes large. In principle, these high-frequency spectral estimates should be representative of the typical oceanic wavefield. However, the high-frequency waves might well be modified by the specific low-frequency background through which they propagate. In this event, the large number of degrees of freedom does not establish that the results are globally representative.

The spectra $E(k, \omega)$ are presented in three different formats in this paper.

1) Spectral Cross Sections: The spectrum $E(k, \omega)$ is plotted versus k for a set of fixed frequencies. Statistical stability is achieved by averaging in frequency.

2) Logarithmically Averaged Two-Dimensional Spectra: The squared Fourier coefficients are averaged over bins in both frequency and wavenumber. The averaging interval increases logarithmically with both ω and k. The resulting spectral estimates have 4 degrees of freedom in the lowest ω–k bands and several hundred degrees of freedom at large ω, k. Again, the spectral estimates can be viewed as "snapshot" quantifications of the low-frequency, low-wavenumber motions that happened to occur under FLIP during the experiment. At high frequency and wavenumber the statistical significance of the estimates is greater, in principle.

3) Frequency-Smoothed Logarithmically Averaged Spectra: One of the striking features of the logarithmically averaged spectra is a series of ridges that run parallel to the wavenumber axis at fixed frequencies. The ridges are sufficiently strong to obscure much of the underlying form of the spectrum in the frequency band between the semidiurnal tide and 1 cph. In order to compare the oceanic spectral estimates with the Garrett-Munk model spectrum, which did not account for these ridges, additional smoothing in frequency is necessary. The frequency smoothing enables a clear look at the resulting continuum (i.e., the spectrum that is forced to appear continuous by the smoothing process).

Deformed surface plots of the 70 and 75 kHz spectral estimates are presented in Figs. 2 and 3. Contour maps of the frequency-smoothed log–log averaged data are presented in Figs. 4 and 5. Spectral cross-sections are presented in Fig. 6. A discussion of various aspects of these spectra is given next.

4. Discussion: Spectral estimates

a. The wavenumber–frequency spectrum

Deformed surface plots of the log–log averaged spectra from the 70 kHz sonar and 75 kHz sonar are presented in the top halves of Figs. 2 and 3. The spectra are essentially red in frequency for frequencies greater than inertial. They are also red in wavenumber except near the inertial frequency, where a broad band of wavenumbers is energetic. The total integrated variance of the spectra is 19.7 cm^2 s^{-2} for the 70 kHz spectrum of downward propagating energy (henceforth referred to as a downward spectrum), 15.9 cm^2 s^{-2} for the spectrum of upward energy propagation (upward spectrum), 18.7 cm^2 s^{-2} for the 75-kHz downward spectrum, and 13.8 cm^2 s^{-2} for the 75-kHz upward spectrum. These variance estimates are underestimates of the total wavefield variance. They represent the contribution due to motions of vertical wavelength 600 m and less. Longer wavelengths contribute variance to the zero-wavenumber band of the spectrum, which is not plotted. Since FLIP drifted freely during this experiment, only motions that vary significantly over the vertical aperture of the array can be distinguished from the signal of FLIP's drift. As the navigation was not sufficiently precise to remove the drift signal, the zero-wavenumber band has been neglected. The spectra drop into the noise at high frequency and high wavenumber. The observed level implies an integrated noise variance of $\sim$2 cm^2 s^{-2}, assuming a white noise spectrum.

b. Spectral ridges

The deformed surface plots of the spectra are dominated by a series of ridges, which run parallel to the wavenumber axis at several frequencies. The lowest-frequency ridge corresponds to near-inertial motion. A broad band of near-inertial wavenumbers is energetic. Higher frequency ridges correspond to

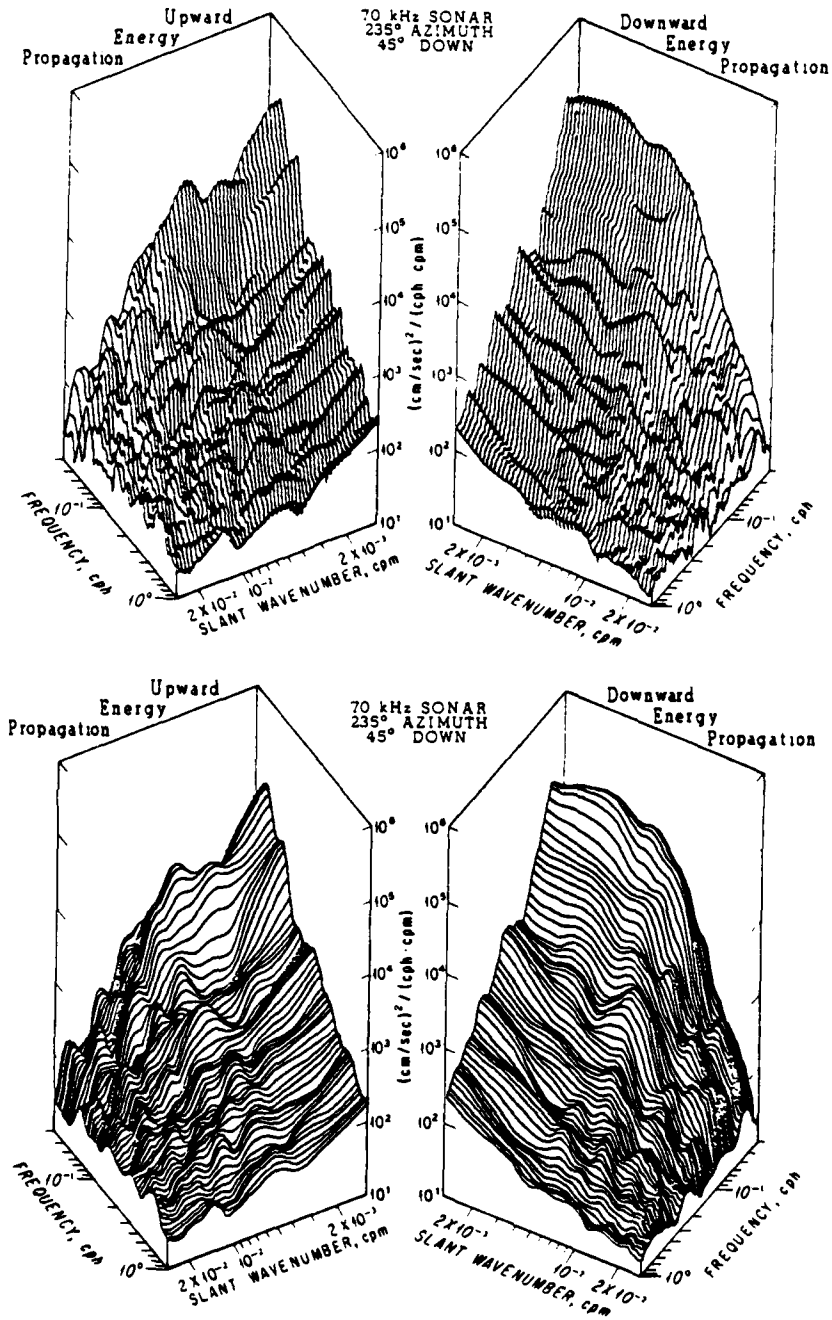

FIG. 2. Wavenumber–frequency spectral estimates obtained from the 70 kHz sonar (direction 235°). The upper spectrum has been logarithmically averaged in both wavenumber and frequency. The lower spectrum has been additionally smoothed in frequency to suppress the series of ridges that parallels the wavenumber axis. At low frequencies, a high wavenumber cutoff is seen at slant wavenumber of order $k_z = 0.01$ cpm.

the baroclinic tide and what might be harmonics of the tidal and inertial frequencies (Pinkel, 1983). The fact that these possible harmonics stand out at low wavenumber, but not at high, indicates a steeper spectral slope (in wavenumber) for these ridges than for the regions between the ridges. The vertical co-

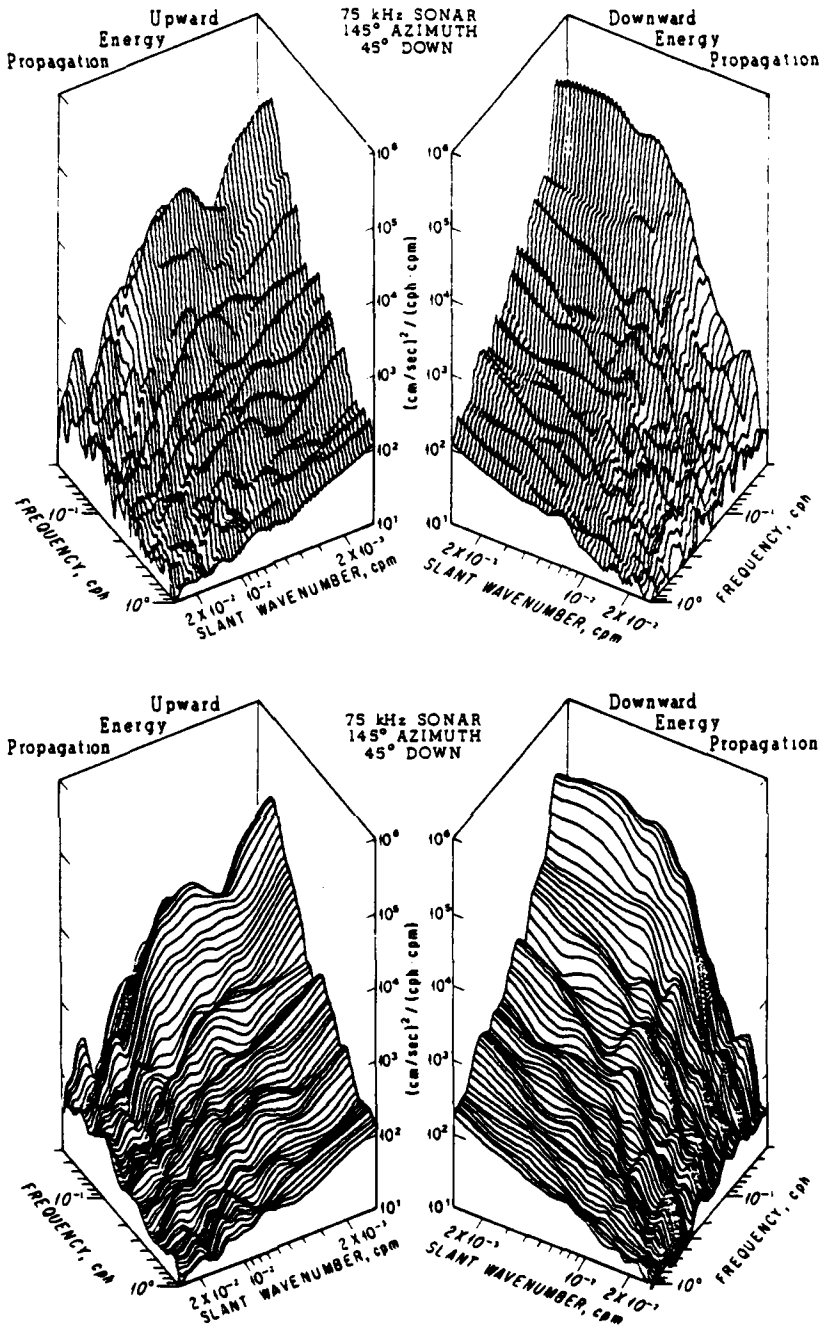

FIG. 3. As in Fig. 2 but from the 75 kHz sonar (direction 145°).

herence of the wavefield, which is related to the wavenumber bandwidth of the spectrum, should correspondingly be greater for the ridges than between them. This is seen in the analysis of Pinkel (1983).

In part, the regularity of these ridges is due to the poor resolution of the spectrum at low wavenumber. The log–log averaging process obscures the fact that independent estimates of the spectrum are much more widely spaced (on a log–log plot such as this) at low frequency and wavenumber than at high. Nevertheless there is no corresponding set of ridges paralleling the frequency axis, an artifact of log-

averaging in frequency. The point is that the irregularities in these spectra are not symmetric with respect to the ω–k axes. This symmetry would be expected if the irregularities were strictly due to statistical imprecision in the spectral estimates.

c. *Spectral shoulder*

The ridges make it difficult to visualize the underlying form of the spectrum. To see this form, the log–log averaged portraits can be further smoothed in frequency, forcing the spectrum to appear continuous. The frequency-smoothed log–log averaged spectra are displayed in Figs. 2 and 3 (lower) as deformed surface plots, and in Figs. 4 and 5 (upper) as contour maps. The interesting feature that emerges from the smoothing is a distinct change in the slope of the spectrum with wavenumber. This occurs at a slant wavelength of approximately 100 m. The change is frequently preceded by an irregularity in the spectrum reminiscent of the pre-cutoff peak that is found in frequency spectra of internal waves just prior to the Väisälä cutoff. This wavenumber pre-cutoff spectral shoulder extends continuously from the inertial frequency band up to 0.2 cycles per hour (cph), with little change in wavenumber. The slope of the spectrum with wavenumber is very steep in the region of the cutoff, exceeding k^{-5} in some instances.

The spectral shoulder and high-wavenumber cutoff were first seen in temperature profiling data also taken from FLIP (Pinkel, 1975, Figs. 16–18). They would appear to be a ubiquitous feature of the spectrum and a strong clue to the physics of the wavefield.

d. *Separability*

Garrett and Munk hypothesized that the wavenumber dependence of the spectrum does not change with frequency, except for perhaps a scale factor. This hypothesis can be investigated by plotting cross sections of the spectrum with wavenumber at a set of fixed frequencies. A set of cross sections is presented in Fig. 6 for the 70 and 75 kHz spectra. Cross sections are given at octave increments with center frequencies of 1, 2, 4, 8, 16, 32, and 64 cpd. The averaging bandwidth about these center frequencies is increased with increasing center frequency, corresponding to 20, 36, 68, 132, 260, 516, and 1028 degrees of freedom, respectively. Note that at 64 cpd, these data can no longer be thought of as vertical profiles of horizontal velocity. Nevertheless, no dramatic change in spectral form is seen.

It is interesting that differences in these cross sections are more pronounced between upward and downward propagation direction than between azimuthal directions. In the near-inertial cross sections, motions with downward energy propagation are energetic over a wide range of wavenumbers, with maximum energy density at slant wavelengths of 500 m. Energy levels are uniformly greater for the downward propagating than for upward propagating motions. The upward spectra decay quickly from a low-wavenumber maximum and exhibit a pronounced secondary peak at slant wavelengths of 200 m. Traces of this peak are seen at the same wavenumber in the higher-frequency cross-sections, forming the pre-cutoff spectral shoulder. The near-inertial cross sections sensed by the different sonars are nearly identical. This is expected, however, as these near-inertial motions are almost circular when viewed from above. Estimates of near-inertial velocity variance should not be sensitive to the azimuthal direction of measurement.

The two-cycle per day cross section is dominated by the baroclinic tide. At low-wavenumber the upward propagating motions are more energetic by a factor of two. However the situation reverses at higher wavenumber, with downward propagating motions becoming more energetic. This crossover is more apparent in the 70 kHz spectrum than in the 75 kHz spectrum.

At higher frequencies the vertical asymmetry is reduced, although there are significant differences up to 16 cpd, particularly in the 70 kHz data. Upward energy propagation tends to exceed downward. The spectral shoulder, prominent in the spectrum of upward energy propagation at low frequency, becomes less distinct at high frequency. The wavenumber slope of the spectrum decreases with increasing frequency, approaching $k^{-1/2}$ at 64 cpd. The high-wavenumber, high-frequency levels are significantly influenced by noise in the sonar measurements. The $k^{-1/2}$ slope must eventually steepen in order that the shear variance be finite.

e. *Bandwidth*

It is not clear that one is justified in parameterizing the changes in these cross sections with frequency with a single variable, *bandwidth*. Indeed, for the upward spectra, the cross sections appear remarkably similar, except for a progressive change in mean spectral *slope*. Nevertheless, the notion of gross spectral bandwidth is useful. It is worthwhile to introduce a definition of bandwidth that is appropriate, given the changing form of the spectrum. A simple approach is to remove the frequency dependence of the spectrum, calculating a normalized, dimensionless spectrum

$$\hat{E}(k, \omega) = \frac{E(k, \omega)}{E(\omega)},$$

where

$$E(\omega) = \frac{1}{k_{max}} \int_0^{k_{max}} E(k, \omega) dk.$$

Frequency smoothed log–log averaged contour maps of the normalized spectra are presented in the

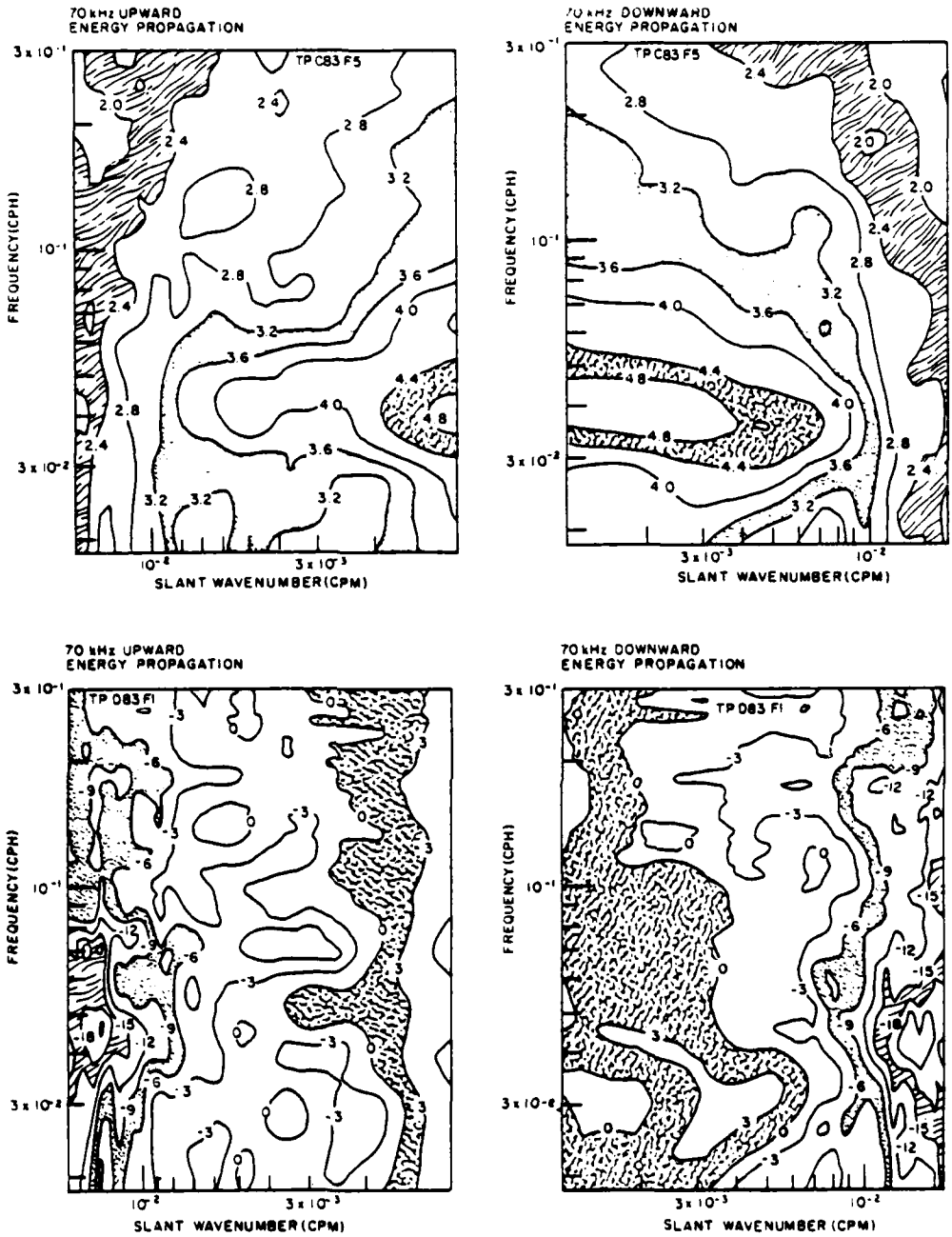

FIG. 4. Contour maps of the frequency-smoothed log–log averaged spectrum from the 70 kHz sonar. The upper maps represent the estimate of the slant velocity spectrum, $(\text{cm s}^{-1})^2/(\text{cpm} \cdot \text{cph})$, contoured at logarithmic intervals. The lower maps give the spectral estimate normalized such that

$$\frac{1}{k_{max}} \int_0^{k_{max}} E(k, \omega) dk = 1$$

for all ω. The contour interval is in decibels. The position of the zero dB contour line indicates the wavenumber at which the spectral level equals the mean spectral level at each frequency, when averaged over wavenumber. The position of the 3 dB contour line indicates the wavenumber at which twice the mean level is found, etc.

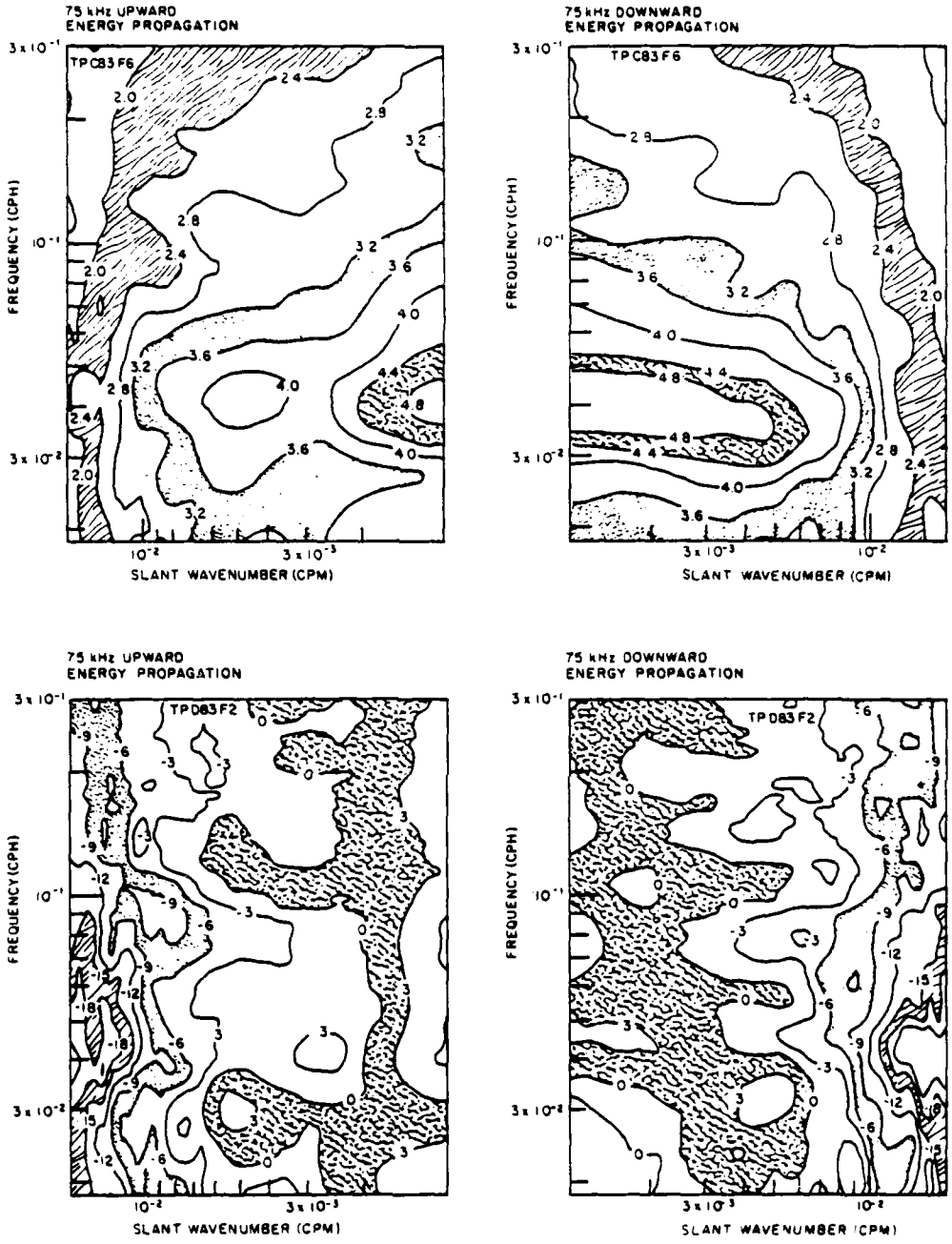

FIG. 5. As in Fig. 4 but from the 75 kHz sonar.

lower panels of Figs. 4 and 5. The maps are contoured in dB relative to unity, with a 3 dB contour interval. The individual contour lines can be taken as separate measures of the spectral bandwidth. There is a clear difference in the gross form of these frequency-normalized spectra. The upward spectra have contours generally parallel to the frequency axis. There is a significant widening of the contours near the inertial frequency, corresponding to an increase in short wavelength upward propagating motions. The inertial bandwidth maximum falls below the local inertial frequency. The energy spectra themselves (upper panels, Figs. 4 and 5) show the energy peak at the inertial frequency. The downward spectra also show the

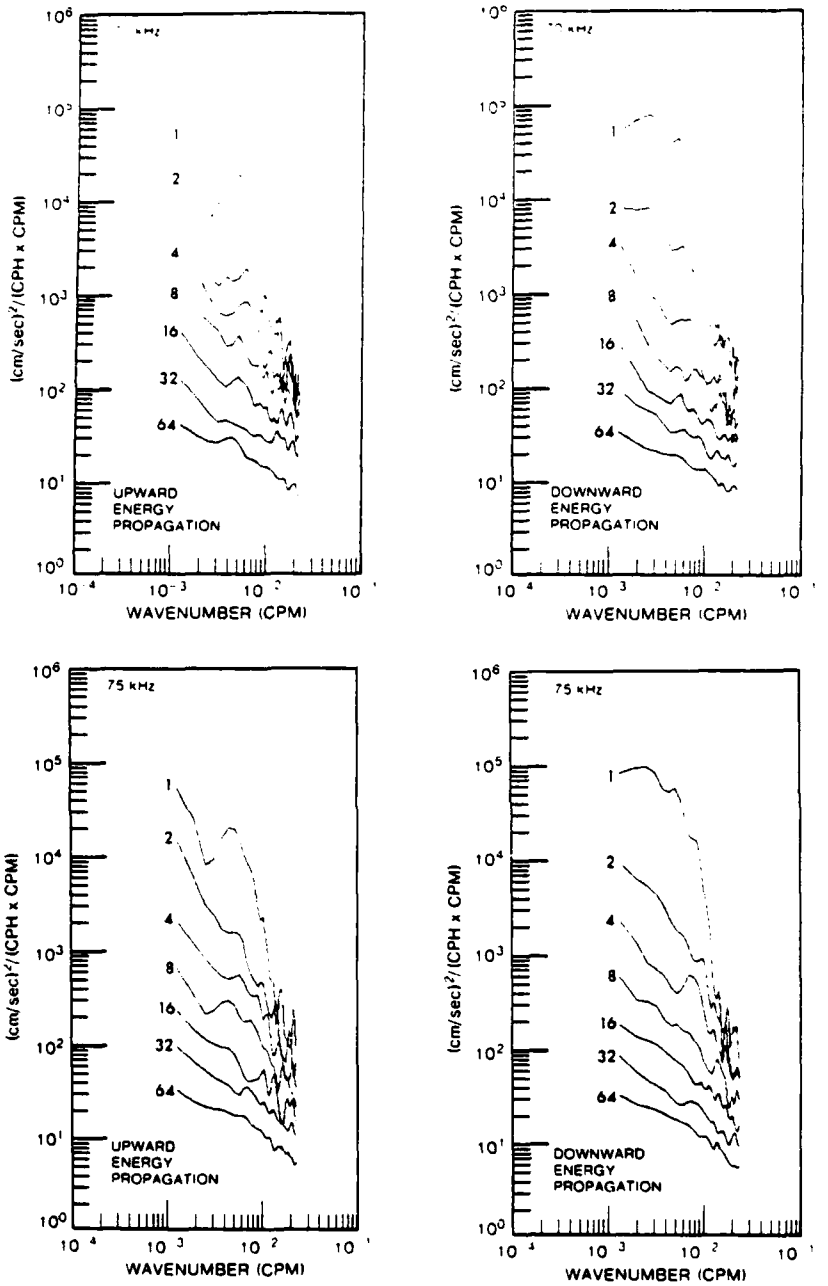

FIG. 6. Cross sections of the 70 and 75 kHz wavenumber–frequency spectra. Sections are taken at frequencies of 1, 2, 4, 8, 16, 32 and 64 cpd. Averaging across frequency is done to improve the statistical stability of the sections. The spectral estimates are formed at 20, 36, 68, 132, 260, 516 and 1028 degrees of freedom.

broadest bandwidth at and below the inertial frequency. However, if one traces the 0 dB contour line, the "bandwidth" is seen to decrease gradually with frequency, up to frequencies of 0.2 cph. While the internal-wave spectrum has been known to be asymmetric in the near-inertial frequency band (Leaman and Sanford, 1975), this is the first clear indication that the asymmetry extends to much higher frequency. It is interesting that the upward and downward energy levels are not greatly different, yet the gross form of

the corresponding spectra are. Note that the lower value contour lines do not parallel the 0 dB line. This is in part a consequence of the normalization procedure, which forces the high wavenumber region of the spectrum to appear larger at high frequency than at low frequency. In spite of these effects, the vertical asymmetry in spectral form is striking.

f. Vertical energy fluxes

The asymmetry in the form of the spectrum encourages an attempt to isolate the sources of wave energy and model the energy residence time of the wavefield. The first step in this effort is to estimate the net vertical energy flux as a function of wavenumber and frequency. The flux is calculated by assuming that the measured velocities are entirely due to horizontal motion, correcting the spectra by a factor of 2 to account for this, and multiplying by a factor that represents the partition of kinetic and potential energy as a function of frequency. The flux is given by

$$F(k, \omega) = [E_{dn}(k, \omega) - E_{up}(k, \omega)]C_{gz}(k, \omega)X(\omega),$$

where

$$C_{gz}(k, \omega) = \frac{(\omega^2 - f^2)(N^2 - \omega^2)^{1/2}}{k_z\omega(N^2 - f^2)^{1/2}}$$

$$X(\omega) = \left(1 + \frac{\omega^2 - f^2}{\omega^2 + f^2}\right)$$

Here, f is the local inertial frequency taken as 1/24 cph, N is taken as 2.5 cph, C_{gz} is the vertical component of the group velocity and X the ratio of kinetic plus potential energy to kinetic energy alone. Maps of the spectral energy flux density (W m^{-2})/(cpm × cph) are presented in Fig. 8. The net fluxes, integrated over the spectrum, are 0.0018 W m^{-2} upward and 0.0010 W m^{-2} upward for the 70- and 75-kHz sonars respectively. Individual contributions to this flux are given in Table 1.

The dominant contributor to this surprising net upward flux is the high-frequency continuum, from 5 to 60 cpd. Here the upward energy slightly exceeds the downward (Fig. 7, bottom). While these motions have much less energy than downward propagating near-inertial waves, they extend over a broader range of frequencies and are associated with larger vertical group velocities.

In addition to this mysterious mean upward flux in the 5–60 cpd band, a distinct downward flux is seen in the near-inertial band and in the semidiurnal tidal band, at high wavenumber. At low wavenumber, tidal energy is propagating upward. The upward tidal flux is approximately 0.000267 W m^{-2} in itself, as estimated from the 70 kHz spectrum (Fig. 8a). Were this flux maintained globally, a result of the scattering of the barotropic tide from the sea floor, the global upward flux would be of order 6×10^{11} Watts. This amount is approximately 15% of the energy-loss rate of the earth–moon system, as reported by Munk (1981). Curiously, much of this flux is canceled by the downward flux of tidal energy at higher wavenumbers (Table 1). The net tidal flux is sufficiently small that it cannot be detected using only phase-difference information between pairs of vertically separated measurements (Pinkel, 1983, Fig. 9). Also, the tidal flux sensed by the 75 kHz sonar is much weaker than that detected by the 70 kHz sonar.

It is likely that the source of baroclinic tidal energy is not the sea floor in general but rather the Patton Escarpment, a 300 km long, 3 km deep steplike division between the Southern California continental borderland and the deep sea. The 70 kHz sonar was directed nearly orthogonal to this escarpment. It should be sensitive to waves propagating from it. The tidal energy does not appear confined to narrow depth zones, as ray theory would suggest (Rattray, 1960). At a distance 240 km offshore of the escarpment, the energy is predominantly in very-long wavelength motions, which fill the 600 m vertical observing window. If one assumes that the wave ray slope is given by $k_H/k_z = [(\omega^2 - f^2)/(N^2 - \omega^2)]^{1/2}$, the tidal ray has made approximately two round trips from sea surface (shelf edge) to sea floor. In this distance the high-wavenumber motions that serve to localize the beam might have been dissipated or destroyed, leaving only the low-wavenumber components. Alternatively, the generated wave train might not be as spatially confined as ray theory predicts.

There are several prominent sources of error in these flux estimates. Most significantly, the 45° downward-slanting sonar beams cannot in principle distinguish between vertical asymmetry and horizontal anisotropy. The net upward flux at high-frequency results from a 10–20% difference in up–down spectral levels. Horizontal anisotropy might contribute substantially to this difference. The spectral analysis resolves only motions of 600 m vertical scale or less. Longer motions have faster group velocity and are

TABLE 1. Positive flux downwards.

	$\Delta\omega$ (cpd)	Δk (cycles per slant kilometer)	70 kHz (W m^{-2})	75 kHz (W m^{-2})
Total flux	0.5–60	1.5–25	−0.001791	−0.001032
Near-inertial flux	1–1.5	1.5–25	+0.000209	+0.000249
Tidal, long wavelength	1.5–2.5	1.5–2.5	−0.000267	+0.000160
Tidal, short wavelength	1.5–2.5	2.5–25	+0.000392	+0.000157
Mid-frequency	2.5–5	1.5–25	+0.000130	−0.000163
Mid-frequency	5–15	1.5–25	−0.000974	−0.000025
High frequency	15–25	1.5–25	−0.000788	−0.000566
High frequency	25–60	1.5–25	−0.000554	−0.000509

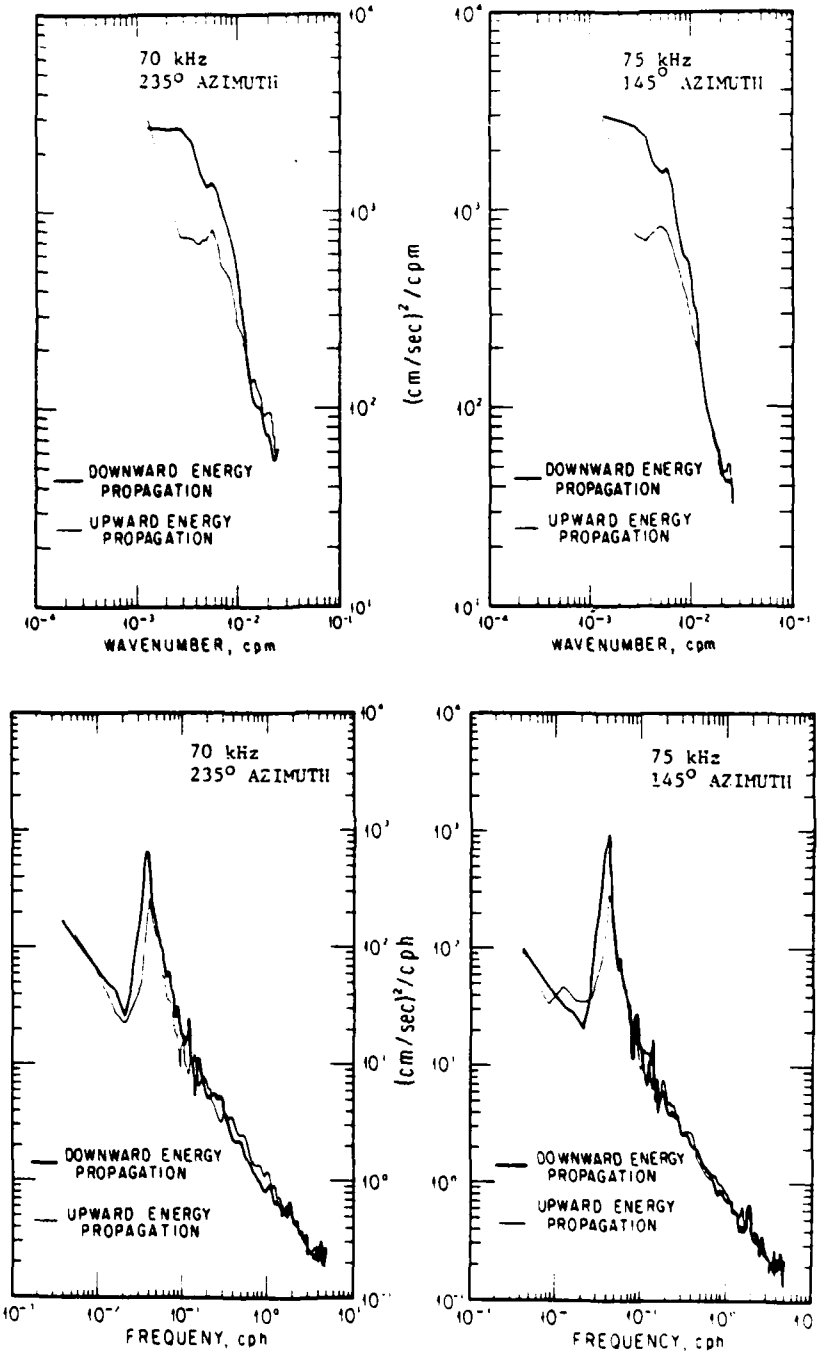

FIG. 7. Estimates of the wavenumber–frequency spectrum integrated in frequency, to produce a slant wavenumber spectrum (top), and in wavenumber, to produce a frequency spectrum (bottom). The dark line corresponds to the integrated downward spectrum, the light line to the upward. For comparison with conventional profiling measurements (top), or moored time series measurements (bottom), the upward and downward contributions should be summed. Note that the low-frequency, high-wavenumber cutoff, visible in Figs. 2, 3 and 6 is largely obscured when the spectrum is integrated over frequency (top). Also, the upward frequency spectra (bottom) tend to have more variance than the downward over a broad band of high frequencies. As these motions have a greater vertical group velocity than the more energetic near-inertial motions, they are the predominant contributors to the net *upward* energy flux of the wavefield.

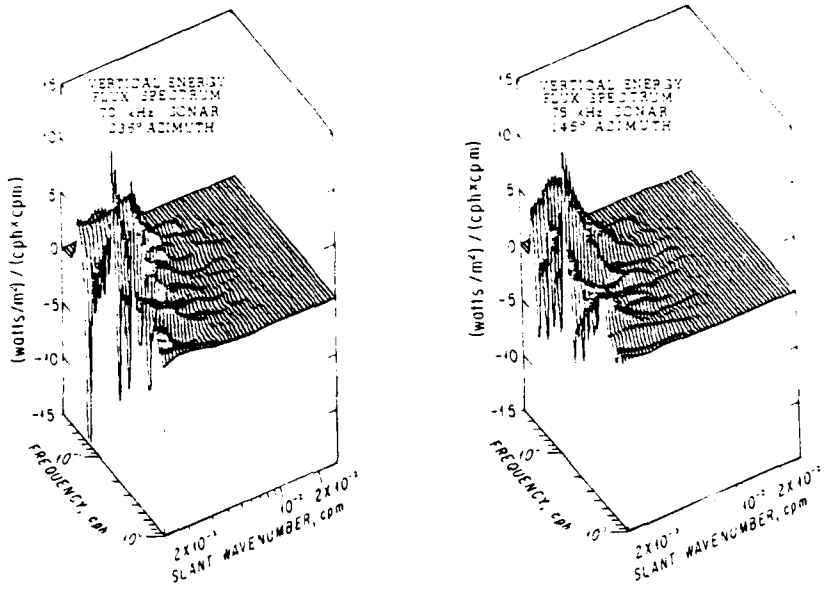

FIG. 8. Deformed surface plots of energy flux spectrum $F(k, \omega)$ for the 70 and 75 kHz sonars. The spectra are log-log averaged, and presented so as to preserve the visibility of the spectral ridges. Positive spectral values correspond to a downward energy flux. The 70 kHz spectrum has been truncated in the semidiurnal tidal band. The upward-flux spectrum peaks at approximately -25 W m^{-2} (cph · cpm)$^{-1}$ in this band. The upward-flux contribution from the higher-frequency waves, which dominates the net wavefield flux, is obscured by all of the detail in this figure.

capable of carrying a large flux. The limited low-wavenumber resolution is of particular concern in the case of the tidal flux estimates. There is also spectral leakage from positive to negative wavenumbers. This tends to equalize spectral levels at low wavenumber. As the group velocity is greatest here, the tendency is to underestimate the flux. Doppler-shifting constitutes a final source of error. The spectrum is most asymmetric near the inertial frequency. The vertical component of group velocity vanishes at the inertial frequency and is sensitive to small differences between ω and f. A drift velocity of 3 cm s^{-1} is sufficient to Doppler-shift the frequency of a 10-kilometer wavelength wave from 1.1 to 1.36 cpd. The group velocities that would be assigned to the shifted and unshifted waves differ by a factor of 3! The Doppler problem is inherent in time series observations of the wavefield. An alternative approach is to measure the spectrum as a function of k_H and k_z from a spatial survey, and infer the intrinsic frequency of the waves from the ratio k_z/k_H. D'Asaro and Perkins (1984) are exploring this approach.

In spite of these difficulties, it would be attractive to use the flux estimates to generate estimates of the energy residence time of the wavefield. Unfortunately, in the absence of knowledge of the spatial distribution of energy sources and sinks, flux measurements alone are inadequate for this purpose. For example, one can consider a model ocean with dissipation uniform throughout the interior and with equal internal wave forcing at the sea surface and sea floor. Measurements made near the sea surface would show a net downward flux. Near the sea floor an upward flux would be seen. At mid-depth the net flux is zero. Obviously, the dissipation rate is not proportional to any of these measured fluxes, but rather to the *flux divergence*. Experimental efforts must be redirected toward the goal of measuring flux divergences before significant progress will be made in understanding wavefield generation and dissipation.

Disregarding this fundamental issue, one can define an "energy loss rate"

$$\dot{E}(k, \omega) = (E_{dn} - E_{up})/T(k, \omega),$$

where $T(k, \omega)$ is the round-trip travel time from the sea surface to the sea floor at each wavenumber and frequency. While the up–down spectral difference fluctuates irregularly, the smooth variation in $T(k, \omega)$ imposes a significant pattern on any estimate of $\dot{E}$. The round-trip travel time is contoured for a 4 km deep ocean in Fig. 9. For the waves resolved in this study, it varies from tens to hundreds of days. If all of the energy in the sea were found to be going downward (or all upward) the energy replacement time would be given by $T(k, \omega)$. In this experiment, where differences in up–down spectral levels are

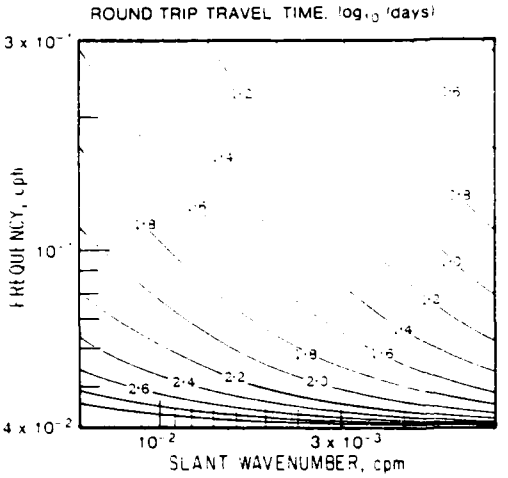

FIG. 9. A contour map of the theoretical round-trip travel time for linear internal waves propagating in a 4 km ocean of mean Väisälä frequency 1 cph. The logarithm ($\log_{10}$) of the travel time is contoured. For the waves resolved in this experiment, travel times are of order tens to hundreds of days.

typically less than a factor of 2, the replacement time is correspondingly longer. However, the validity of this type of loss rate calculation is highly suspect given ignorance of flux divergences.

5. Discussion: Comparison with other measurements

a. *Profiling measurements*

Sanford (1975) has pioneered the measurement of velocity profiles on scales larger than several meters. Using electromagnetic sensors on free-fall instruments he has obtained profiles with spectra of approximate k^{-2} slope between 10 and 100 m vertical scales. He has identified most of the observed variance at the larger scales with near-inertial motion.

Gargett *et al.* (1981) have proposed a composite spectrum of shear from scales of hundreds of meters to 1 cm. Their work is consistent with (and partially based on) Sanford's measurements down to 10 m. In this region the shear spectrum is constant. Between 10 and 1 m the spectrum decreases, suggesting a high-wavenumber cutoff to the internal wavefield. This is also seen in the temperature fine-structure measurements of Gregg (1977). At scales smaller than 1 m the spectrum changes to a region dominated by the intermittent occurrence of turbulence.

The spectral cross sections of Fig. 6 in this work are sufficiently irregular that one would hesitate to characterize the wavenumber dependence by a simple power law. Yet, when integrated over frequency, (Fig. 7) the resulting wavenumber spectra are practically identical to those of Sanford (1975, Fig. 13). The low-wavenumber region of this integrated spectrum is dominated by low-frequency motions. The high-wavenumber region is dominated by the high frequencies, which obscure the low-frequency high-wavenumber cutoff. This distinction is significant for those modeling the cascade of energy in the wavenumber domain, from the largest scales to dissipation scales (Holloway, 1983). In the internal wave regime, the shift in frequency associated with changing vertical scale should be considered.

b. *Vertical coherence measurements*

Garrett and Munk (1972, 1975, 1979) have emphasized the role that coherence estimates play in inferring the bandwidth of the spectrum. They have demonstrated that the coherence $R(\Delta z, \omega)$ is related to $E(k, \omega)$ by

$$R(\Delta z, \omega) = \frac{\left| \int_{-\infty}^{\infty} E(k, \omega) \cos k \Delta z dk \right|}{\int_{-\infty}^{\infty} E(k, \omega) dk}$$

for a spectrum *symmetric in k*. Estimates of the vertical coherence of *horizontal* velocity have been found to decrease with increasing frequency (Webster, 1972; Briscoe, 1975). Estimates of the vertical coherence of *vertical* velocity are constant or slightly increasing with increasing frequency (Pinkel, 1981b). Garrett and Munk have diplomatically decided that the bandwidth of the spectrum is essentially constant with frequency (except at very-high frequency, near N). The difference in coherence behavior has been ascribed to so-called finestructure contamination of the measurements (Briscoe 1975, 1977; Müller *et al.*, 1978). As with previous measurements, the issues of coherence, bandwidth and finestructure contamination are central to the interpretation of these Doppler acoustic data. The coherence–bandwidth issue will be discussed first, followed by a discussion of finestructure contamination.

When Figs. 4 and 5 are examined one gets the impression that the bandwidth of the spectrum is greatest at low-frequency (at least for downward propagating energy) and decreases gradually with increasing frequency. Yet estimates of slant-coherence (Pinkel, 1983) are also greater at low-frequency than at high. This should indicate an increasing bandwidth with frequency. This apparent inconsistency within the same data set is due to the changing wavenumber dependence of the spectrum with frequency. The similarity (separability) hypothesis of Garrett and Munk is sufficiently invalid that different definitions of bandwidth exhibit markedly different variation with frequency. In particular, in Figs. 4 and 5 lower, the 0-dB contour line is suggested as an index of bandwidth. With coherence measurements, the value of the coherence at fixed separation is related to the

bandwidth. It is consistent that these two indices exhibit opposite behavior, once the similarity hypothesis is relaxed. As an example consider the two hypothetical spectral cross sections shown in Fig. 10a. The rectangular cross section has a coherence of

$$R_1(\Delta z) = \frac{\sin(k_1 \Delta z)}{k_1 \Delta z}.$$

The coherence of the triangular section is

$$R_2(\Delta z) = \frac{2[1 - \cos(k_2 \Delta z)]}{(k_2 \Delta z)^2}.$$

At small separations such that $k_i \Delta z \ll \pi/4$, these expressions can be approximated as

$$\left.\begin{aligned} R_1(\Delta z) &\approx 1 - \frac{(k_1 \Delta z)^2}{6} \\ R_2(\Delta z) &\approx 1 - \frac{(k_2 \Delta z)^2}{12} \end{aligned}\right\}.$$

If $k_2 = \sqrt{2} k_1$, the coherences at small separation Δz are nearly identical. If the two spectral cross sections are perturbed slightly so as to resemble the data (Fig. 10b) one would not be inclined subjectively to say that the bandwidths are the same. Yet at small $k\Delta z$, the coherences are surprisingly similar.

c. Temperature measurements

When temperature measurements are used to infer vertical motions in the sea, a significantly different view of the internal wavefield is obtained. The most apparent and easily understood discrepancy is the absence of near-inertial waves. These have very little vertical motion and thus are not seen.

A more disturbing difference is found in the vertical structure of the measurements. At frequencies between the inertial frequency and 0.5 cph the vertical coherence is approximately constant. It rises to a pre-cutoff maximum and then falls at the local Väisälä frequency (Briscoe, 1975; Pinkel, 1975). Correspondingly, the vertical-wavenumber dependence of the spectrum of vertical motion is steeper in the pre-cutoff peak region than at lower frequencies. Zalkan (1970) has identified the waves in this region to be predominantly first mode.

The vertical coherence of horizontal velocity, in contrast, tends to decrease with increasing frequency. There is no coherence increase associated with a pre-cutoff region in the horizontal velocity spectrum. The spectral estimates presented here tend to get less steep in wavenumber as frequency increases. If the motions sensed are indeed *linear* internal waves, spectra and coherences from the two types of sensors should be essentially identical.

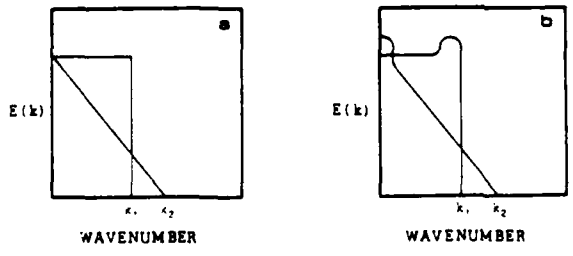

FIG. 10. (a) Spectral cross sections of two hypothetical wavenumber–frequency spectra. The cross sections are associated with nearly identical values of coherence over small separations Δz. (b) Slightly perturbed variants of these spectral forms having only slightly different coherence. Yet, qualitatively, one would not be inclined to say that they have the same bandwidth. While coherence is an appropriate way to quantify spectral bandwidth, it is not very sensitive.

d. Finestructure contamination

Historically, this discrepancy has been explained in terms of passive finestructure contamination of fixed-depth sensors (Phillips, 1971). It is necessary to hypothesize different degrees of contamination for the temperature and horizontal velocity measurements to account for the different coherence behavior.

Finestructure contamination of temperature is modeled starting with the heat equation

$$\frac{DT}{Dt} = 0.$$

Changes in vertical velocity are inferred from changes in fixed-depth temperature by

$$\frac{\partial T}{\partial t} = -w \frac{\partial T}{\partial z} - \bar{\mathbf{u}} \cdot \nabla_H T.$$

Even when $\nabla_H T$ is negligibly small, if the vertical component of the temperature gradient $\partial T/\partial z$ is not constant in depth, sinusoidal variations in w do not result in sinusoidal variations in $\partial T/\partial t$ at the sensor. The measurements are said to be contaminated.

The corresponding governing equation for horizontal velocity is

$$\frac{D\bar{u}}{Dt} = -\frac{1}{\rho} \nabla p - 2\bar{\Omega} \times \bar{u}.$$

The Eulerian acceleration $\partial \bar{u}/\partial t$ measured by a fixed-depth current sensor is only equal to the ratio of force/mass if the advective terms in the total derivative, $\bar{\mathbf{u}} \cdot \nabla \bar{\mathbf{u}}$, are negligibly small. Finestructure contamination is said to occur when the $w\partial \bar{u}/\partial z$ term is significant when compared with $\partial \bar{u}/\partial t$. Note that finestructure contamination of temperature is a totally kinematic phenomenon, whereas the "passive" contamination of horizontal velocity is essentially dynamic. To the extent that the dominant contributor to the open-ocean shear is the internal wavefield itself, finestructure contamination of horizontal velocity is an index of wavefield nonlinearity. The

discrepancy in vertical coherence between temperature and horizontal velocity measurements becomes a strong clue to the physics of the wavefield.

Briscoe (1977) did a careful study of the finestructure contamination of horizontal velocity measurements in the Sargasso Sea. He concluded that the majority of the contamination comes from motions on scales less than 1 m. The total amount of contamination was too small to explain the discrepancy in vertical coherence measurements in the IWEX data set. Müller *et al.* (1978), in explaining the discrepancy, found it reasonable to postulate the existence of a second field of motion, not internal waves, which exists in the internal-wave frequency band and at higher frequencies. These motions are purely horizontal, with large horizontal coherence scales and short vertical scales.

Recently, Müller, Henyey and Holloway (personal communication, 1984) have suggested that the nonlinear advection of the small-scale potential vorticity field past any fixed sensor will result in an observed signal similar to the one hypothesized. Müller has termed this field the "Vortical Mode." Measurements of horizontal velocity will suffer reduced vertical coherence, as the vortical motions are unrelated in the vertical. Vertical velocity or displacement measurements will be essentially unaffected. If an added class of motions is contributing to the wavenumber–frequency spectrum of slant velocity, but not to that of vertical velocity, a detailed comparison of the two spectra can be used to infer the spectrum of the nonwave motions. This will be done using the 1980 sonar and CTD data.

Regardless of the source of "contamination," the disparity in the relative contamination of temperature and velocity measurements suggests that linearity of the overall field be investigated. For example, one can consider a group of high-frequency motions in a band 1 cph wide centered at 1 cph. The rms horizontal and vertical velocities are both approximately 1 cm s^{-1} in typical oceanic conditions. If a representative background shear $\partial u/\partial z$ of order 10^{-3} s^{-1} is considered, perhaps associated with lower frequency near-inertial motions, then

$$\left.\begin{aligned} \frac{\partial u}{\partial t_{\text{rms}}} &\approx 1.7 \times 10^{-3} \\ w_{\text{rms}} \frac{\partial u}{\partial z} &\approx 10^{-3} \end{aligned}\right\}.$$

One would hesitate to neglect this advective term (Holloway, 1980). Since the vertical velocity spectrum and the horizontal acceleration spectrum are nearly white, nonlinearity will be significant even at lower frequencies. It is likely that measurements of Eulerian acceleration differ from the ratio of force/mass by a significant amount. Modeling this as a passive finestructure is perhaps unwise.

6. Summary and conclusions

During an 18-day period in May 1980, while FLIP drifted southward in the California Current, oceanic velocity data were obtained in the top 600 m of the sea using a pair of Doppler sonars. These data were used to estimate the slant wavenumber–frequency spectrum of the motions observed. The spectral estimates, at low frequency, represent an accurate description of the particular wave groups that passed under FLIP during the course of the experiment. At higher frequency, the statistical confidence of the spectral estimates is much greater. However, to the extent that the high-frequency motions are influenced by the lower-frequency "background" through which they propagate, standard measures of statistical precision do not necessarily imply representativeness.

The spectral estimates are basically red in both frequency and wavenumber. Near-inertial peaks dominate the spectra. The spectrum of downward propagating near-inertial motions is both more energetic and broader in wavenumber bandwidth than that of upward motions. This asymmetry is seen to extend to frequencies nearly five times inertial. The excess downward energy is associated with a clockwise (viewed from above) sense of rotation (Appendix).

At low frequencies, both upward and downward spectra appear to have a high-wavenumber cutoff at a vertical scale of 60 m. Spectral slopes in the cutoff region approach k^{-5}. The cutoff is much less visible at frequencies above 5 cpd. As a consequence of this changing spectral form with frequency, the major contribution to the shear on vertical scales less than 60 m is from high-frequency motions. In contrast, the Garrett-Munk spectral model indicates that near-inertial motions dominate the shear field at all vertical scales.

With minimal smoothing, the spectral estimates display prominent ridges which run parallel to the wavenumber axis. The ridges might be harmonics of the inertial and tidal fundamental peaks. That the spectrum is so irregular is of relevance to modelers who are attempting to estimate wave–wave interaction rates for the wavefield. Holloway (1982) has emphasized that the number of wave groups in any one volume of the sea, available for interaction, is less than the smooth "process spectrum" of the wavefield would indicate. The average interaction resulting from many realizations of the instantaneous wavefield can be different from the net interaction predicted from the averaged wavefield spectrum.

If the ridges are indeed forced harmonics of the tide there are additional dynamic implications. Olbers and Pomphrey (1981) have argued that scattering of the barotropic tide from the sea floor can be at most a negligible source of energy for the internal wavefield. Their argument is based on the fact that the weak resonant nonlinear transfer rates from the baroclinic

tidal band to other regions of the internal-wave spectrum are very slow. Energy cannot leak out of the tidal band at an adequate rate to be an important source for the wavefield. However, if forced nonresonant interactions are occurring, tidal energy can be transferred to higher frequencies at a much greater rate. At high frequencies, even the weak resonant transfer rates become large. It would be interesting to repeat the "spectral bump" experiments of McComas and Müller (1981) from a different perspective. Rather

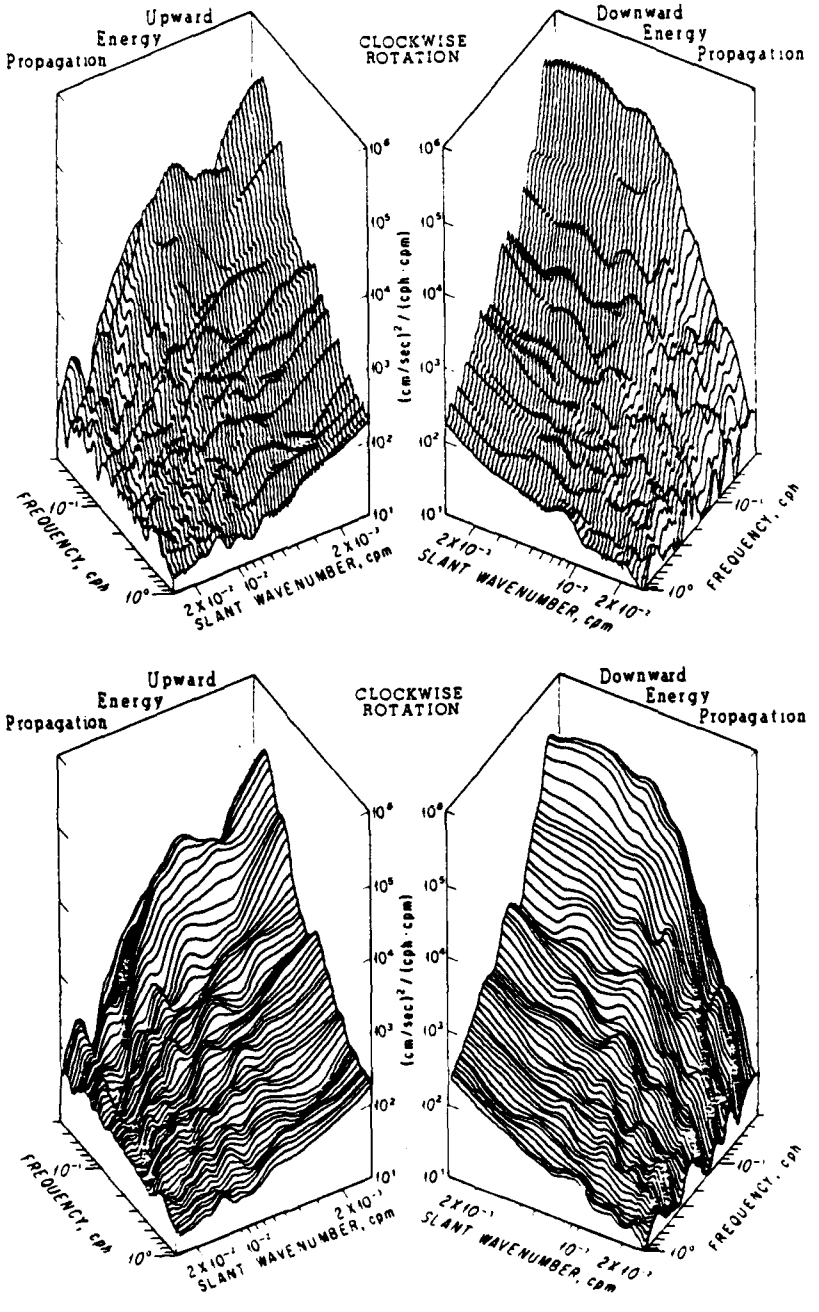

FIG. 11. Clockwise rotary wavenumber–frequency spectral estimates obtained from combining 70 and 75 kHz sonar information. The upper spectrum has been logarithmically averaged in both wavenumber and frequency. The lower spectrum has been additionally smoothed in frequency to suppress the series of ridges that parallels the wavenumber axis.

than estimating the decay time of a perturbation on an otherwise smooth spectrum, one might calculate the energy flux needed to maintain a "spectral bump" in steady state. This would provide the beginning of a theoretical perspective to these observations.

The vertical coherence of slant (effectively horizontal) velocity is not consistent with vertical coherences estimated using vertical velocity or displacement data. In the past this discrepancy has been ascribed to "finestructure contamination" of the horizontal velocity measurements. However, the sonar measurements are averages over approximately 20 m in the vertical, and they still appear "contaminated." It is reasonable to invoke the presence of an additional

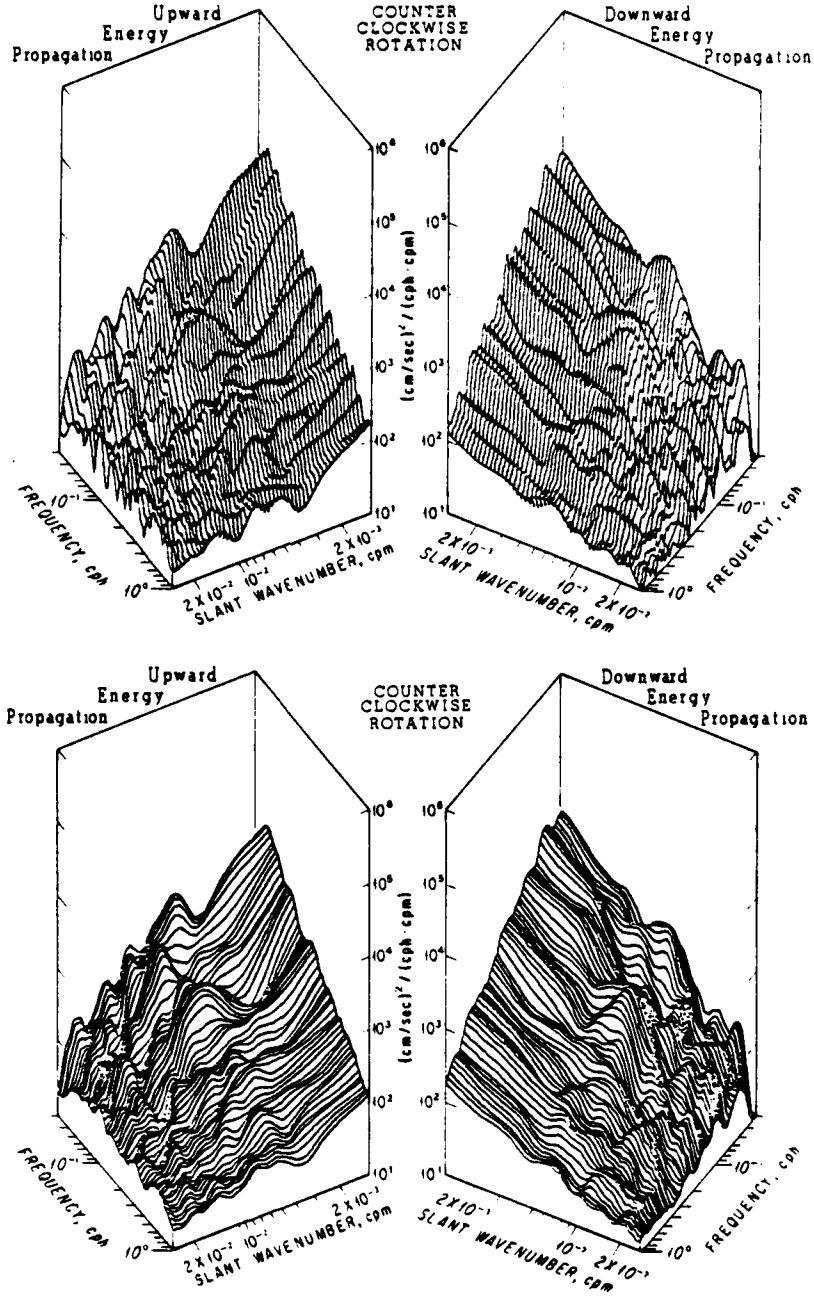

FIG. 12. As in Fig. 11 but for a counterclockwise sense of rotation.

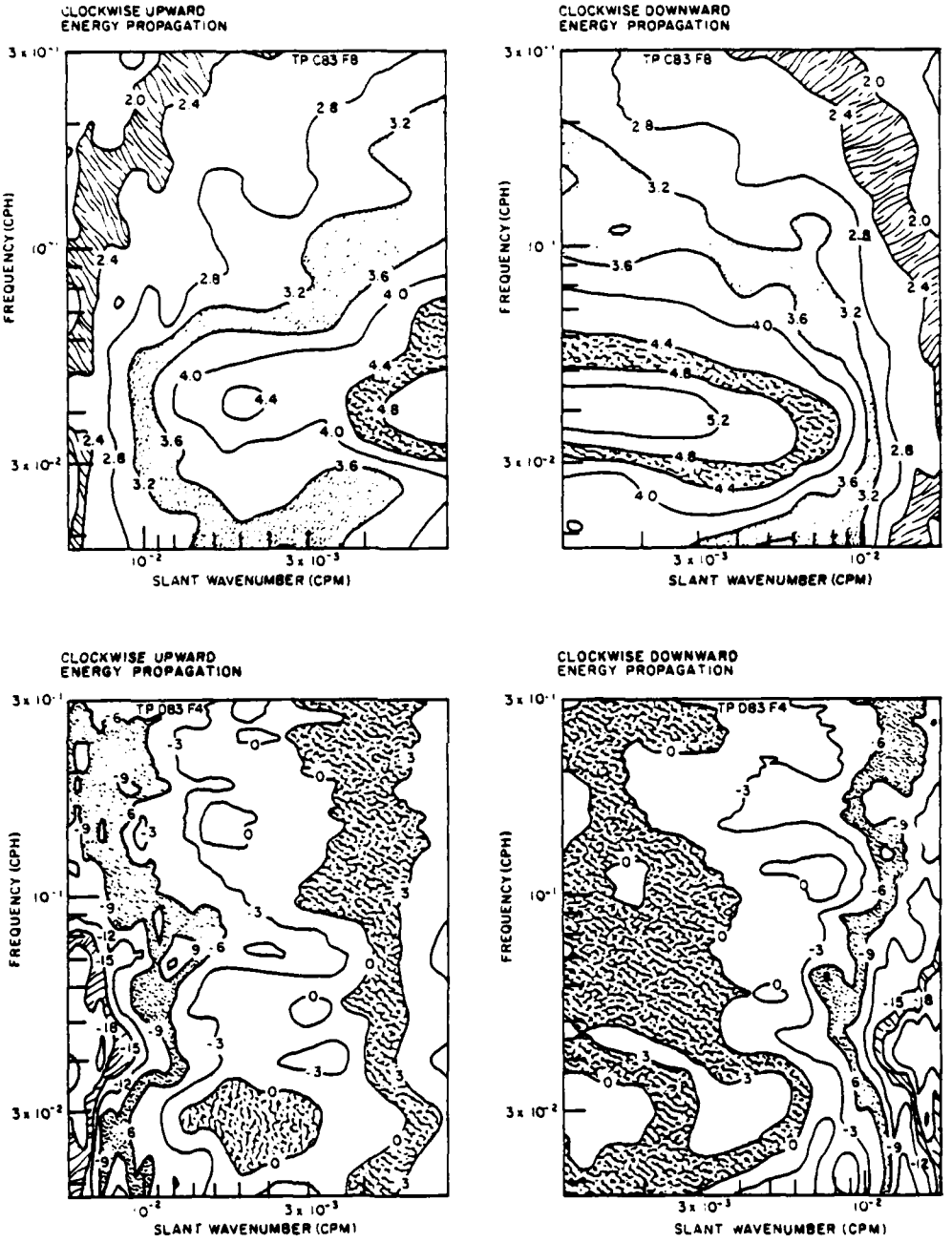

FIG. 13. Contour maps of the frequency-smoothed log–log averaged spectrum of clockwise motion. The upper maps represent the estimate of the slant velocity spectrum, $(\text{cm s}^{-1})^2(\text{cpm} \cdot \text{cph})^{-1}$, contoured at logarithmic intervals. The lower maps give the spectral estimate normalized such that

$$\frac{1}{k_{max}} \int_0^{k_{max}} E(k, \omega) dk = 1$$

for all ω. The contour interval is in decibels. Note that the pronounced variation in bandwidth with frequency, seen in the 70 and 75 kHz downward spectra, occurs only in the clockwise downward spectrum here. It is not seen in the downward counterclockwise spectrum (Fig. 14, bottom).

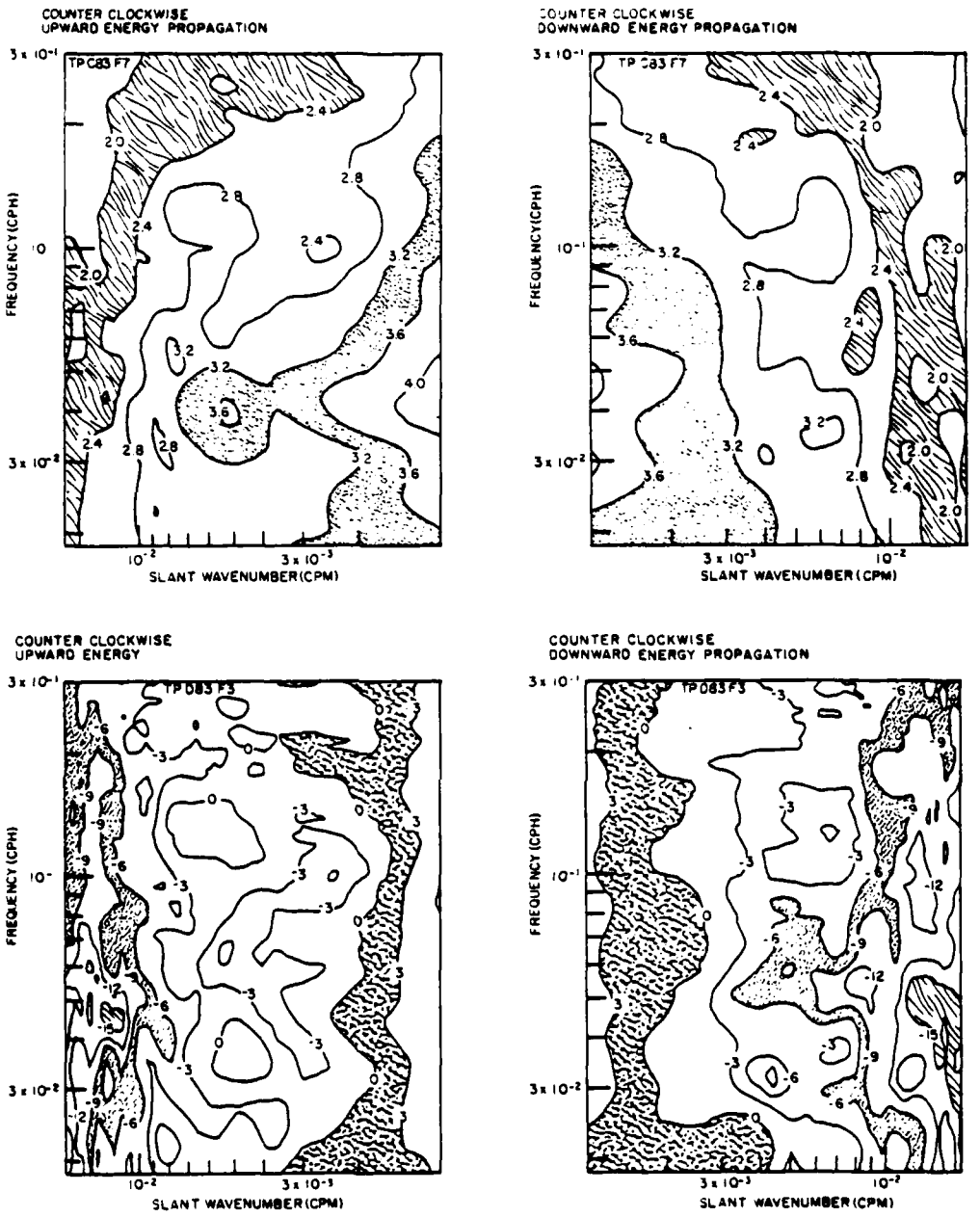

FIG. 14. As in Fig. 13 except for a counterclockwise sense of rotation. Note that neither the upward nor downward spectral estimate exhibits a significant change in bandwidth with frequencies.

field of motion with long horizontal, but short vertical, coherence scales, as was done by Müller *et al.* (1978) in IWEX. The dynamics of this hypothesized class of motions is now being investigated by Müller (personal communication, 1984) and others. The coherence discrepancy, regardless of specific explanation, encourages one to note that the advective term $w\partial u/\partial z$ can be of the same order as $\partial u/\partial t$ in the upper ocean.

The vertical energy flux associated with the waves resolved in this experiment ($\lambda_z < 600$ m) is approximately 0.0028 W m^{-2} upward. Significant contributors to the flux are short-wavelength near-inertial motions which take energy slowly downward, and the long-wavelength baroclinic tide which displayed strong upward energy propagation. However, the primary contributor is the high-frequency (5–60 cpd) continuum, which has much faster vertical group speeds than the lower-frequency motions. If one assumes

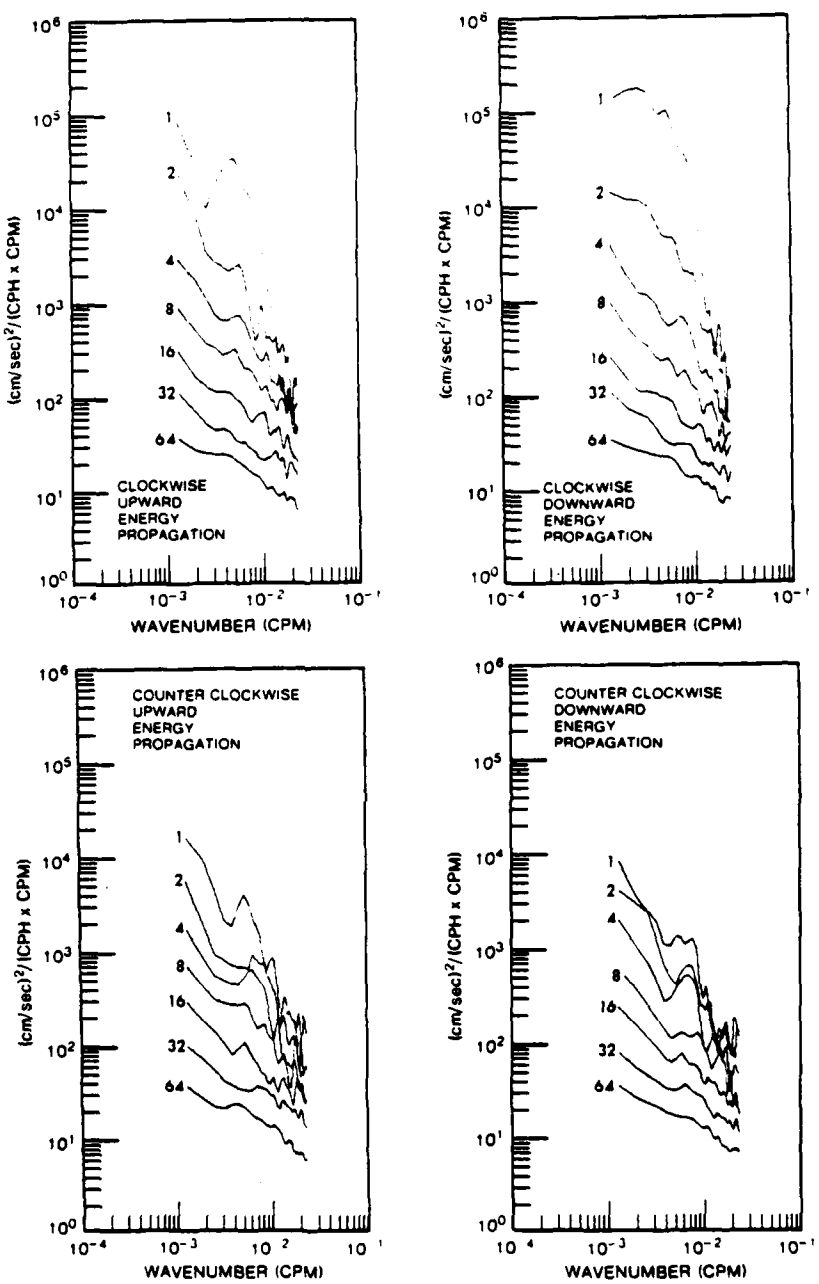

FIG. 15. Cross sections of the clockwise and counterclockwise wavenumber–frequency spectra. Sections are taken at frequencies of 1, 2, 4, 8, 16, 32 and 64 cpd. Averaging across frequency is done to improve the statistical stability of the sections. The spectral estimates are formed at 20, 36, 68, 132, 260, 516 and 1028 degrees of freedom.

that the wavefield is forced entirely from regions above or below the experiment, energy replacement times can be calculated. These are on the order of tens to hundreds of days. In part these long times are a consequence of the slow rates of vertical propagation of the waves resolved in this study. Longer vertical-wavelength motions propagate faster. A conclusive picture of the energetics of the wavefield cannot be formed in the absence of adequate measurements of the energy flux divergence.

Acknowledgments. The author would like to thank S. Beck, M. Goldin, L. Green, L. Occhiello, E. Slater, L. Tomooka and W. Whitney for designing, devel-

oping and operating the Doppler sonar system on FLIP. W. Davy led the MPL development group in the construction of the sonar equipment. D. Efird, the Captain of FLIP, accommodated this equipment on his vessel and operated it safely for the duration of the operation. Discussions with H. Abarbanel, W. Hodgkiss, G. Holloway, W. Munk and W. R. Young were particularly helpful in the development of this work. This program is funded by ONR Code 220, ONR Code 420 and NORDA Code 540.

APPENDIX

Rotary Spectral Analysis

Rotary wavenumber–frequency spectra can be calculated from the 70 and 75 kHz sonar data in the manner suggested by Gonella (1972). The profiles are first-differenced, Väisälä-stretched, and triangle-windowed, as for the conventional spectra. They are combined prior to Fourier transformation in the vertical such that rotary Fourier coefficients are obtained. A normalization is chosen such that the sum of the clockwise and counterclockwise (viewed from above) spectral variances is equal to the sum of the 70 and 75 kHz spectral variances. Spectral variances are 30.8, 20.7, 7.9 and 9.3 $cm^2\ s^{-2}$ for the clockwise down, up, counterclockwise down, up spectra respectively.

No attempt is made to correct for the fact that the sonar beams are diverging with increasing depth. At 600 m depth the beams are separated by more than 1 km. Velocity differences of order 1–2 $cm\ s^{-1}$ are likely over this separation. As a result the rotary spectral estimates are contaminated by a noise that increases with depth and is coherent with the signal.

In spite of this contamination, a number of features stand out in the rotary spectral estimates. The spectra are presented as deformed surface plots in Figs. 11 and 12, as contour maps in Figs. 13 and 14, and as spectral cross sections in Fig. 15. For frequencies higher than 0.2 cpd the spectra are nearly identical, independent of sense of rotation or direction of vertical propagation. The significant differences appear in the near-inertial band. The clockwise downward spectrum is nearly two orders of magnitude more energetic than the either of the counterclockwise spectra. The high-wavenumber region of the clockwise downward near-inertial ridge appears Doppler-shifted to a frequency below inertial. This is not the case with the less energetic clockwise upward near-inertial signal. The spectra can be normalized so as to remove the frequency dependence as was done for the conventional spectra. The resulting contour maps indicate that only the clockwise downward spectrum has a "bandwidth" that increases with decreasing frequency. A constant bandwidth is a more appropriate characterization of the other three spectra. The high-wavenumber cutoff is visible at low frequency in all four rotary spectral estimates.

REFERENCES

Briscoe, M. G., 1975: Preliminary results from the trimoored internal wave experiment (IWEX). *J. Geophys. Res.*, **80**, 3872–3884.

——, 1977: On current finestructure and moored current measurements of internal waves. *Deep-Sea Res.*, **24**, 1121–1131.

D'Asaro, E. A., and H. Perkins, 1984: The near inertial internal wave spectrum in the late summer Sargasso Sea. *J. Phys. Oceanogr.*, **14**, 489–503.

Gargett, A. E., P. J. Hendricks, T. B. Sanford, T. R. Osborn and A. J. Williams, III, 1981: A composite spectrum of shear in the upper ocean. *J. Phys. Oceanogr.*, **11**, 1258–1271.

Garrett, C. J. R., and W. H. Munk, 1972: Space-time scales of internal waves. *Geophys. Fluid Dyn.*, **2**, 225–264.

——, and ——, 1975: Space-time scales of internal waves, a progress report. *J. Geophys. Res.*, **80**, 291–297.

——, and ——, 1979: Internal waves in the ocean. *Annual Reviews of Fluid Mechanics*, Vol. 11, Annual Reviews, 339–369.

Gonella, J., 1972: A rotary component method for analyzing meteorological and oceanographic vector time series. *Deep-Sea Res.*, **19**, 833–846.

Gregg, M. C., 1977: A comparison of finestructure spectra from the main thermocline. *J. Phys. Oceanogr.*, **7**, 33–40.

Holloway, G., 1980: Oceanic internal waves are not weak waves. *J. Phys. Oceanogr.*, **10**, 906–914.

——, 1982: On interaction time scales of oceanic internal waves. *J. Phys. Oceanogr.*, **12**, 293–296.

——, 1983: A conjecture relating oceanic internal waves and small-scale processes. *Atmos. Ocean*, **21**, 107–122.

Leaman, K. D., and T. B. Sanford, 1975: Vertical energy propagation of internal waves: A vector spectral analysis of velocity profiles. *J. Geophys. Res.*, **80**, 1975–1978.

McComas, C. H., and P. Müller, 1981: Time scales of interaction among oceanic internal waves. *J. Phys. Oceanogr.*, **11**, 139–147.

Müller, P., D. J. Olbers and J. Willebrand, 1978: The IWEX spectrum. *J. Geophys. Res.*, **83**, 479–500.

Munk, W. H., 1981: Internal waves and small scale processes. *Evolution of Physical Oceanography*. B. A. Warren and C. Wunsch, Eds., The MIT Press, 264–290.

Olbers, D. J., and N. Pomphrey, 1981: Disqualifying two candidates for the energy balance of oceanic internal waves. *J. Phys. Oceanogr.*, **11**, 1423–1425.

Phillips, O. M., 1971: On spectra measured in an undulating layer medium. *J. Phys. Oceanogr.*, **1**, 1–6.

Pinkel, R., 1974: Observations of internal waves in the upper ocean. Ph.D. thesis, University of California, San Diego, 154 pp.

——, 1975: Upper ocean internal wave observations from FLIP. *J. Geophys. Res.*, **80**, 3892–3910.

——, 1981a: On the use of Doppler sonar for internal wave measurements. *Deep-Sea. Res.*, **28A**, 269–289.

——, 1981b: Observations of the near-surface internal wavefield. *J. Phys. Oceanogr.*, **11**, 1248–1257.

——, 1983: Doppler sonar observations of internal waves: Wavefield structure. *J. Phys. Oceanogr.*, **13**, 804–815.

Rattray, M., Jr., 1960: On the coastal generation of internal tides. *Tellus*, **12**, 54–62.

Sanford, T. B., 1975: Observations of the vertical structure of internal waves. *J. Geophys. Res.*, **80**, 3861–3871.

Webster, T. F., 1972: Estimates of the coherence of ocean currents over vertical distances. *Deep-Sea Res.*, **19**, 35–44.

Weller, R. A., 1984: Near inertial motions observed in and below the mixed layer. Submitted to *J. Phys. Oceanogr.*

Zalkan, R. L., 1970: High frequency internal waves in the Pacific Ocean. *Deep-Sea Res.*, **17**, 91–108.

APPENDIX D

THE WAVENUMBER-FREQUENCY SPECTRUM OF UPPER OCEAN SHEAR

Robert Pinkel

Marine Physical Laboratory of the

Scripps Institution of Oceanography

University of California, San Diego

La Jolla, CA 92093

ABSTRACT

In May 1980 an eighteen day sequence of oceanic velocity profiles was obtained off the coast of Southern California. The measurements were made using a pair of Doppler sonars mounted on the research platform FLIP and angled downward 45°. The profiles extend to a depth of 600 m. Depth resolution is approximately 30 m. From these profiles the wavenumber-frequency spectrum of the oceanic shear field, $\Phi(\kappa,\omega)$ is estimated.

At low frequency, from one to five times inertial, the low wavenumber portion of the spectrum is most energetic. The near inertial shear contribution has the greatest spectral density. There is a pronounced cut-off with wavenumber of the spectrum at approximately 60 m vertical scale. At higher frequencies, the cut-off is obscured and the wavenumber dependence of the spectrum becomes progressively more blue. When $\Phi(\kappa,\omega)$ is integrated over all frequency, the resulting wavenumber spectrum $\Phi(\kappa)$ is nearly white, in good agreement with the previous measurements of Gargett et al. (1981). The wavenumber spectral levels are approximately a factor of four greater than the Gargett et al. (1981) Atlantic measurement.

It is unlikely that the high frequency - high wavenumber shear is a result of internal wave activity. The spectrum $\Phi(\kappa,\omega)$ is not consistent with previous estimates of the spectrum of vertical displacement, $<\eta^2>(\kappa,\omega)$ (Pinkel, 1975), if internal wave scaling is used. The vertical displacement spectrum becomes progressively more red (low mode dominated) with increasing frequency while the shear spectrum becomes progressively more blue. An added class of motions, with horizontal currents and shears but not vertical, is called for to explain this

discrepancy (Müller et al., 1978, Müller, 1984). In ignorance of the dynamics of this added class of motions, it is unwise to use internal wave WKB scaling to describe the vertical variation of the shear field.

INTRODUCTION

This paper presents estimates of the vertical wavenumber - frequency spectrum of shear, $\Phi(\kappa,\omega)$. The measurements were made using a pair of Doppler sonar mounted on the Research Platform Flip. The shear spectral estimates are essentially re-weighted versions of velocity spectra presented in a companion paper (Pinkel, 1984). It is worthwhile to present them independently here in that they differ greatly from the pre-existing model of the shear spectrum (Garrett and Munk, 1975-1979). Specifically, at low frequency, one to five times inertial, the low wavenumber region of the spectrum has the greatest variance density. At higher frequencies the spectrum becomes progressively more blue (Figs 1,2).

Three points will be emphasized in this work. The first is that this unusual estimate of $\Phi(\kappa,\omega)$ is completely consistent with previous estimates of the shear spectrum as a function of vertical wavenumber alone, $\Phi(\kappa)$. Specifically, Gargett et al. (1981) have presented estimates of $\Phi(\kappa)$ which are essentially white down to scales of 10 m and transition to a κ^{-1} form between 10 m and 1 m.

In attempting to explain the transition in $\Phi(\kappa)$ at 10 m vertical scale, both Holloway (1980) and Munk (1981) have suggested that a wave - shear interaction criterion is relevant. A change in spectral form should be observed at that vertical scale Δz where waves of vertical wavelength $\lambda = \Delta z$ have a horizontal phase speed $c = \frac{N}{2\pi}\lambda$ of the order of the expected difference in horizontal velocity $\Delta u(\Delta z)$ over vertical separation Δz. The horizontal velocity difference is presumed due to larger vertical scale waves. However, when realistic values of $\Delta u(\Delta z)$ are considered, a vertical scale of 60 m, not 10 m is suggested. The second emphasis of this work is to demonstrate the existence of this change in $\Phi(\kappa,\omega)$ at 60 m scale, not seen by Gargett et al. (1981), and to show why it is not apparent in the one dimensional spectrum $\Phi(\kappa)$.

The final point is that the high frequency high vertical wavenumber shear variance, which is a significant fraction of the overall shear in the sea, is not likely due to internal waves. Previous estimates of the wavenumber - frequency spectrum of vertical displacement, $<\eta^2>(\kappa,\omega)$ (Pinkel, 1975) have a high wavenumber high frequency spectral form which is inconsistent with the present estimate of $\Phi(\kappa,\omega)$ if internal wave scaling is applied. Specifically, the wavenumber dependence of the displacement spectrum becomes more red with increasing frequency while that of the shear spectrum becomes more blue. Attempts to scale the depth variability of the shear field using WKB internal wave scaling can be greatly in error.

A brief description of the measurements and the analysis technique is given next. The remainder of the paper discuses the various forms of the shear spectrum which are presented.

MEASUREMENTS

The observations of the shear field were obtained during an 18-day period in May 1980. The measurements were made using a pair of Doppler sonars mounted on the Research Platform FLIP. The operation commenced at 30°50'N, 124°'W, approximately 500 km WSW of San Diego. It concluded 200 km to the south, at 28°40'N, 124°0'W.

The sonars were mounted on FLIP's hull at a depth of 38 m and slanted 45° downward. They were operated at frequencies of 70 and 75 kHz. The 70 kHz sonar was directed toward 235° true, a direction nearly orthogonal to the Patton Escarpment, a 2 km step in the seafloor which parallels the California coast for some 500 km. It will henceforth be referred to as the offshore sonar. The 75 kHz sonar was oriented toward 135° true, approximately parallel to the escarpment and (perhaps) to the mean path of the California Current. The strategy was to maximize the sensitivity of the offshore sonar to baroclinic motions generated at the Patton Escarpment by the barotropic tides. It was anticipated that the orthogonal, longshore sonar, (75 kHz) would see the less of a tidal signature and more of the effects of the mean shear of the California Current.

These measurements are described in greater detail in Pinkel (1983). The subsequent wavenumber-frequency spectral analysis is described in Pinkel (1984). Several items should be noted, however. First, the effective range resolution of the sonar is of order 40 m (depth resolution is approximately 30 m). The resolution is set by the duration of the acoustic pulse transmitted by the sonars. As a consequence, these data cannot resolve the change in the shear spectral form at 10 m observed by Gargett et al. (1981).

A second consideration is the use of WKB stretching in the two-dimensional spectral analysis of these data. WKB stretching is used to correct for the effects of refraction of the propagating internal waves, due to variations of the Väisälä frequency with depth (Pinkel, 1984). It is seen below that a significant contribution to the shear variance comes from high frequency motions which are not likely linear internal waves. The effect of the WKB stretching is to introduce a spatial non-homogeneity to these motions which do not originally scale as internal waves. While this effect is probably slight, it is neverless a concern.

The dominant technical uncertainty in this work is associated with measurement noise. The noise results from both measurement errors in the sonars and from gaps in the time series. Both error sources should contribute to a velocity noise spectrum which is white in frequency and wavenumber. The resulting shear noise spectrum will have a κ^2 wavenumber dependence. The issue is whether this noise spectrum dominates the spectrum of the water motion in any region of the frequency - wavenumber domain resolved by the experiment.

Simple modeling of the shear noise spectrum, suggests it will be a significant contributor in the high frequency, high wavenumber region. Fortunately, the effect of the noise contamination can be "removed" by subtracting a κ^2 spectrum of the appropriate level from the estimated shear spectrum. While simple to implement, this correction alters the estimate of overall shear variance. It also changes the wavenumber dependence of the spectrum at very high frequencies from a monotonically increasing form to a band limited one.

To aid the reader in distinguishing those spectral regions which are unaffected by noise, those where the influence of noise is easily understood, and those where there is no useful

information, spectral estimates are presented in this paper both with and without the modeled noise removed. This enables an intuitive assessment of the data quality. A model shear noise spectrum corresponding to a velocity noise level of 1.5 cm^2/sec^2 is used. This is somewhat less than the actual noise experienced in the offshore, 70 kHz measurements, but more than that experienced in the longshore, 75 kHz measurement. Fortunately, the essential conclusions of this work remain unaffected even when so much modeled noise is "removed" that the resulting longshore spectrum becomes negative at high wavenumber.

The spectral analysis is described in detail in Pinkel (1984), and can be summarized briefly here. The velocity series are first differenced in both time and range and are then Fourier transformed in time. The resulting Fourier coefficients are WKB stretched and Fourier transformed in depth. To obtain spectral estimates of shear rather than "first differenced velocity" the squared Fourier coefficients are "recolored" in wavenumber using the factor $((\pi\kappa/\kappa_s)^2/(2-2\cos(\pi\kappa/\kappa_s)))$ where κ is the wavenumber and κ_s is the Nyquist wavenumber. This factor differs significantly from unity as the Nyquist wavenumber is approached, where it reaches the value $\pi^2/4$. The conventional factor $1/(2-2\cos(\pi\omega/\omega_s)$ is used to recolor the frequency dependence of the spectrum.

Unlike Pinkel (1984), the units of the shear spectra presented here have been scaled to give the variance of horizontal (not slant) velocity per unit of vertical (not slant) distance. Spectral density is given per cycle per vertical (not slant) meter. This facilitates direct comparison with the shear spectrum of Gargett et al. (1981). To justify this conversion, one must assume that the slant differences in vertical velocity are negligibly small and that the horizontal gradient of horizontal velocity is small compared to the vertical gradient.

The shear spectrum $\Phi(\kappa,\omega)$ is presented in several different formats in this paper. In Fig. 1, deformed surface plots of the spectrum are presented for the longshore and offshore sonars. In Fig. 2, these data are combined to produce estimates of the clockwise and counter-clockwise (viewed from above) spectra. In both figures the overall motion field is separated into upward and downward (energy) propagating components. An internal wave convention is assumed here.

with downward energy propagation corresponding to upward phase propagation.

In Figs. 1 and 2, the averaging interval increases logarithmically in wavenumber. A logarithmic averaging technique is used for frequency averaging also. However additional linear smoothing is employed to reduce the signature of a series of spectral ridges which occur at fixed frequencies. These ridges might be harmonics of the baroclinic tide. They cannot be quantified with adequate statistical precision in this limited, 18-day, data set. The linear averaging smoothes them out, allowing a clear view of the underlying continuum. (Whether this "spectral continuum" is strictly an artifact of the severe smoothing remains an issue.)

In Figs. 3 and 4, cross sections of the shear spectrum $\Phi(\kappa,\omega_i)$ are presented as functions of vertical wavenumber at the set of center frequencies $\{\omega_i = 1,2,4,8,10,32 \text{ and } 64 \text{ cpd}\}$. Here linear smoothing is employed in wavenumber. Statistical stability is achieved primarily by averaging in frequency. The frequency averaging interval increases with increasing center frequency.

In Fig. 5 cumulative shear spectra are presented for the 70 and 75 kHz sonars. These are plots of

$$\Phi_i(\kappa) = \int_{1/2\,f}^{\omega_i} \Phi(\kappa,\omega)d\omega$$

for the set of frequencies $\{\omega_i = 1,2,4,8,16,32 \text{ and } 64 \text{ cpd}\}$. Note that in Fig. 5, the upper limit on the integration band is the same as the center of the averaging bands in Figs. 3 and 4.

In Fig. 6 estimates of the frequency spectrum of shear are presented. These are simply

$$\Phi(\omega) = \int_{\kappa_{min}}^{\kappa_{max}} \Phi(\kappa,\omega)d\kappa$$

Here κ_{min} is taken as $1/530$ m^{-1} and κ_{max} as $1/28$ m^{-1}.

The final figure depicts Munk's (1981) inverse Richardson function.

$$R_i^{-1}(\kappa,\omega) = N^{-2} \int_{\kappa_{min}}^{\kappa} \int_{\omega_{min}}^{\omega} \Phi(\hat{\kappa},\hat{\omega})\, d\hat{\omega}\, d\hat{\kappa}$$

Here N is the Väisälä frequency, κ_{min} is $1/530$ m^{-1} and $\omega_{min} = .5$ cpd. This is essentially a

cumulative shear spectrum, normalized by the Väisälä frequency.

DISCUSSION: THE WAVENUMBER-FREQUENCY SPECTRUM OF SHEAR

Estimates of the wavenumber frequency spectrum are presented as deformed surface plots in Figs. 1 and 2 and as series of spectral cross-sections in Figs. 3 and 4. The shear variance associated with the spectrum is sensitive to the assumed level of noise contamination. Two estimates of shear variance are given in Table I. The first includes all forms of measurement noise. The second estimate is obtained after a modeled noise spectrum is subtracted from the direct estimate of $\Phi(\kappa,\omega)$. These variances are calculated over the vertical wavenumber band from 1/530 to 1/28 cycles per meter.

The shear spectrum is seen to be band limited in wavenumber in the region encompassing the inertial and semi diurnal tidal frequencies. Motions of vertical wavelength between 100 and 300 m have the greatest shear spectral density. A pronounced high wavenumber cut-off is seen in the spectrum, particularly in the near inertial frequency region. The cut-off occurs over vertical scales of approximately 50 to 80 m. Spectral slopes exceed κ^{-3} in this region.

As frequency increases, this energetic band limited region subsides into a background which becomes increasingly blue. At frequencies above 80 cpd a nearly featureless blue spectrum is seen. The wavenumber slope of the high frequency region is slightly in excess of κ^{+1}. At very high wavenumber, in excess of 0.03 cpm, a pronounced downturning of the spectrum is seen. This is a manifestation of the finite resolution of the sonar measurements and not a property of the motions in the sea.

The contrast between this estimate of the spectrum and the spectral models proposed by Garrett and Munk (1972, 1975) is clearly seen in Figs. 1-4. Their modeled vertical wavenumber dependence does not change with frequency. Here, the change is striking. On the other hand, Garrett and Munk set out to model the spectrum of a random field of linear interval waves. It

is unlikely that all of the motions which contribute variance to the observed shear spectrum are linear waves.

Support for this contention comes from previous measurements of vertical motion $\eta(z,t)$ obtained with the profiling CTD system on FLIP (Occhiello and Pinkel, 1976). Estimates of the wavenumber frequency spectrum of vertical motion $<\eta^2>(\kappa,\omega)$ become progressively more red in vertical wavenumber as frequency increases (Pinkel, 1975). This is just the reverse of the trend seen in the Doppler data, which are presumably dominated by horizontal, not vertical velocity. At frequencies above 1 cph, the spectrum of vertical velocity is dominated by the lowest internal wave mode. The spectrum of slant velocity, in contrast, looks nearly white. If linear internal waves were responsible for all of the observed motion, the spectral forms should be consistent. Thus, most of the shear variance on vertical scales less than 60 m comes from the part of the spectrum which is the least wave-like. This casts suspicion on the use of internal wave WKB scaling for the motions in this spectral region.

Similarly, the convention used in this work, to separate motions into upward and downward propagating components, needs to be re-examined. Specifically, motions which do not propagate at all will contribute variance equally to the upward and downward spectral estimates. When the up-down spectral levels are examined closely in Figs. 3-4, clear differences are seen at low frequency and intermediate wavenumber, presumably associated with propagating near inertial waves. At high frequency the up-down symmetry is more apparent.

In contrast, the similarity between the offshore and longshore spectra is nearly perfect at low frequency in the near inertial band. Even small irregularities in the spectrum are seen to reproduce (Fig. 3). In the tidal (2 cpd) band there is more variance in the offshore record than in the longshore. Curiously, at high frequency the offshore spectral levels are nearly a factor of two higher than the longshore. This is seen in the 16, 32 and 64 cpd cross sections.

THE VERTICAL WAVENUMBER SPECTRUM OF SHEAR

The wavenumber-frequency spectrum of shear $\Phi(\kappa,\omega)$ is red in wavenumber at low frequency and blue at high frequency. It would seem difficult to reconcile this complex variation with the Gargett et al. view that the wavenumber spectrum $\Phi(\kappa)$ is essentially white at vertical scales longer than 10 m. In fact the two-dimensional spectrum estimated here is consistent with a white $\Phi(\kappa)$. This can be seen by integrating $\Phi(\kappa,\omega)$ over frequency, to achieve a wavenumber spectrum alone. This is done in Fig. 5. The frequency integration is performed in a series of one-octave increments, from 1/2 to 1 cpd, 1/2 to 2 cpd, 1/2 to 4 cpd, etc. In this manner the contribution from the various frequency bands to the various wavenumber bands can be seen. The lowest frequency motions contribute most to the low wavenumber portion of the spectrum, as expected. However, the contribution to scales less than 50 m comes from progressively higher frequencies. This contrasts with the Garrett-Munk hypothesis that near inertial motions dominate the contribution to the shear spectrum at all vertical scales. This distinction is of significance in the statistical modeling of low Richardson number events.

It is not surprising that the shear spectrum is not perfectly white over scales of 10 to 100 m. The long wavelength portion reflects the level of near inertial wave energy, which is known to be highly variable. The the shear spectral level at shorter wavelengths, 50 to 30 m, is approximately a factor of four greater than the Gargett et al. measurements in the Atlantic. A detailed comparison of the measurements is rendered difficult due to the uncertainty in applying the WKB approximation to account for the variations in the Väisälä frequency with depth.

THE FREQUENCY SPECTRUM OF SHEAR

The wavenumber frequency spectrum $\Phi(\kappa,\omega)$ can also be integrated over wavenumber to produce a frequency spectrum of the shear field (Fig. 6). Here frequency spectra are presented for offshore and longshore velocity components as well as for clockwise and counter-clockwise rotating motions. The contributions to these spectra from upward and downward propagating motions are presented separately. The spectral estimates are formed from $\Phi(\kappa,\omega)$ by integrating in κ over 50 wavenumber bands (25 independent bands) and then smoothing additionally in

frequency. Band averaging over 10 bands (above .16 cph) and over 20 bands (above .32 cph) was employed. Adjacent frequency bands are not independent.

The spectra have a nearly ω^{-1} form from 0.1 to 1 cph. A hint of a Väisäla cut-off is seen at 3 cph. Above this frequency the spectra drop to an irregular noise floor of order 3 x 10^{-7} sec^{-2}/cph. The spectral form above 2 cph is strongly influenced by the modeled "noise removal" employed. When no noise is "removed", the 3 cph cut-off becomes less distinct and the high frequency noise level doubles, to approximately 6 x 10^{-7} sec^{-2}/cph.

The ω^{-1} slope at intermediate frequency contrasts with an $\omega^{-1.5}$ slope seen in the corresponding spectrum of velocity (Pinkel, 1984). The difference in slopes result from the changing form of the wavenumber dependence of the spectrum with changing frequency.

Pronounced, near inertial peaks dominate the offshore and longshore spectra, as well as the clockwise rotary spectrum. Near inertial shear variance associated with downward propagating wave groups exceeds that of upward propagating groups. Surprisingly, upward propagating shear levels are found to be significantly greater than downward over the frequency range 0.2 to 2 cph for the offshore sonar (but not the longshore sonar). This is seen in the velocity spectra also (Pinkel, 1984).

THE INVERSE RICHARDSON FUNCTION

Munk (1981) introduced the inverse Richardson function,

$$Ri^{-1}(\kappa) = N^{-2} \int_0^{\kappa}$$

as a means of quantifying the contribution of shear variance to the Richardson number as a function of vertical scale. The white shear spectrum of Gargett et al. (1982) imply a κ^{+1} form for the inverse Richardson function. Here, the definition of the inverse Richardson function can be broadened to include the effects of both wavenumber and frequency variation in $\Phi(\kappa,\omega)$.

$$Ri^{-1}(\kappa,\omega) = N^{-2} \int_{\kappa_{min}}^{\kappa} \int_{\omega_{min}}^{\omega} \Phi(\hat{\kappa},\hat{\omega})\, d\hat{\omega} d\hat{\kappa}$$

$\omega_{min} = 0.5$ cpd

$\kappa_{min} = 1/530$ cpm

The level of Ri^{-1} is somewhat arbitrary in that the proper value of N^2 is difficult to define. A WKB stretching appropriate for internal waves is used to calculate $\Phi(\kappa,\omega)$. Yet much of the high frequency shear might not be due to internal waves. Should the value of N^2 be determined by averaging over the actual depth of the observations or over the WKB stretched depth? If stretched depth is used, the higher values of N are more heavily weighted in the average. The value of $N = 3.6$ cph was chosen, subjectively, for the present calculation. It is closer to the value averaged over stretched rather than real depth.

Profiles of the $Ri^{-1}(\kappa,\omega)$ as a function of wavenumber at fixed frequencies are presented in Fig. 7. The upper most profiles, 0.5 to 1 cpd, 0.5 to 2 cpd, increase rapidly with increasing κ, but then level off considerably at $\kappa > 0.02$, vertical scales shorter than 50 m. This reflects the low level of shear spectral density at high wavenumber (above the wavenumber cut off) relative to that below. Note that most of the "near inertial" inertial shear occurs at frequencies slightly above 1 cpd. This is responsible for the large separation between the 1 cpd and 2 cpd profiles. As the contribution of higher frequencies is included, there is virtually no change in the form of $Ri^{-1}(\kappa,\omega)$ at low wavenumber. This is a consequence of the dominance of near inertial shears at low wavenumber. At high wavenumber, the high frequency contributions of shear variance significantly increase the inverse Richardson function.

Gargett et al. (1981) emphasizes the importance of the value of $Ri^{-1}(\kappa,\omega_{max})$ at the vertical transition scale of 10 m. They suggest a value of $Ri^{-1}(0.1,\omega_{max}) = 1$ is universal. If the present estimates of $Ri^{-1}(\kappa,\omega_{max})$ are extrapolated to 10 m scale, values of 2.5 and 1.2 are obtained for the offshore and longshore data respectively. This corresponds to component Richardson numbers of 0.4 and 0.8. When the results are combined to give an estimate of the Richardson number reflecting both components of the shear an overall value of 0.270 is obtained. It is unlikely that the estimate of N^2 is a factor of four in error. The disagreement between this result and the Gargett et al. universal (but only measured once) value stems

primarily from the unusually large shears associated with a few distinct near-inertial wave packets which propagated under FLIP during the course of the experiment. The shear spectral levels (Fig. 5) are a factor of four greater than Gargett et al. It is not surprising that the Richardson function should be a factor of four smaller. However, the extrapolation of these data from 30 m vertical scale down to 10 m scales is a highly uncertain procedure. The blue regions of $\Phi(\kappa,\omega)$ must eventually level off with increasing wavenumber, and then decrease, in order to be consistent with the Gargett et al. (1981) measurements between 10 and 1 m scales.

CONCLUSIONS

It is useful to summarize this paper in the context of previous discussions by Gargett et al. (1981) and Munk (1981). Over a range of scales approximately 1 to 10 m, Gargett et al. asserted that the shear spectrum is completely determined by the two parameters ϵ and N. Here ϵ is the rate of turbulent dissipation. The shear spectral level is set by

$$\Phi_b \equiv (\epsilon N)^{1/2}$$

A buoyancy scale is defined by

$$\kappa_b = (N^3/\epsilon)^{1/2}$$

They find empirically that the spectrum has a κ^{-1} form at wavenumbers less than κ_b down to some κ_0. Curiously, if one states this explicitly,

$$\begin{aligned}\Phi(\kappa) &= \frac{\kappa_b}{\kappa}\Phi_b \qquad \kappa_0 < \kappa < \kappa_b \\ &= \frac{(\epsilon N)^{1/2}(N^3/\epsilon)^{1/2}}{\kappa} \\ &= \frac{N^2}{\kappa} \qquad \kappa_0 < \kappa < \kappa_b\end{aligned}$$

it is seen that the spectral level in this region is independent of ϵ. Now, if this regime is valid down to some wavenumber κ_0, below which the spectrum is of constant level,

$$\Phi(\kappa) = \Phi_0 \qquad \kappa < \kappa_0$$

then $\Phi_0 = N^2/\kappa_0$. As a consequence, the inverse Richardson function, evaluated at k_0, is always of value 1, independent of N^2, ϵ, κ_0, and the dynamics of the region $\kappa < \kappa_0$.

$$R_i^{-1}(\kappa_0) = \Phi_0 \kappa_0 N^{-2} \equiv 1$$

The discussion can be continued a second step if one truly believes that the shear spectrum $\Phi(\kappa)$ is constant at wavenumbers below κ_0, that its value is globally universal, and that it varies in the vertical according to WKB internal wave scaling, ($\Phi(\kappa,z) \sim N^2(z)$). Then $\kappa_0 = N^2/\Phi$ is a universal dimensional constant independent of both depth and location. Gargett et al. (1981) find κ_0 of order 10 m, approximately six times smaller than the vertical scale Δz over which $\Delta u(\Delta z) = c(\kappa_1)$ ($\kappa_1 = 1/\Delta z_1$) for internal waves. They find no clear sign of a change in the shear spectrum at k_1, although small variations in the spectral shape are noted.

In this work, with both frequency and wavenumber variability of the shear spectrum resolved, a clear indication of a change in spectral form is seen at $\kappa_1 \approx 1/60$ m at frequencies less than 5 times inertial. When integrated over frequency, the resulting wavenumber spectrum $\Phi(\kappa)$ shows little evidence of this transition.

The major contribution to the shear variance at scales $\kappa_1 < \kappa < \kappa_0$ comes from high frequency motions. It is unlikely that this variance is due to internal waves. Previous estimates of the wavenumber frequency spectrum of vertical displacement $\langle\eta^2\rangle(\kappa,\omega)$ (Pinkel 1974, 1975) display a wavenumber dependence which becomes increasingly red with increasing frequency. The present estimate of $\Phi(\kappa,\omega)$ becomes increasingly blue. This disparity is inconsistent with internal wave scaling. Müller (1984) suggests that the shear variance in the high wavenumber, high frequency region results from a second field of motion, a type of two dimensional turbulence which he terms the Vortical Mode. While the dynamics of this added field are as yet uncertain, it is unlikely that the Vortical Mode shear variance will scale with depth identically to that of internal waves. Thus the universality of the dimensional wavenumber k_0 is uncertain. (For these measurements, $\kappa_0 = N^2/\Phi_0 \approx 1/25m$.)

An estimate of the vertical displacement spectrum $\langle\eta^2\rangle(\kappa,\omega)$ is currently being prepared from a sequence of six thousand CTD profiles obtained in May 1980, concurrent with the sonar data set. From the disparity between $\langle\eta^2\rangle(\kappa,\omega)$ and $\Phi(\kappa,\omega)$, the wavenumber frequency spectrum of this added field of motion can be inferred. In advance of this difficult exercise, one

can conjecture that the shear spectrum of the Vortical field is band limited in wavenumber, rising as κ^1 for $\kappa < \kappa_0$ (as seen in the high frequency cross section of Fig. 3-4) and falling as κ^{-1} for $\kappa > \kappa_0$, as estimated by Gargett et al. (1981). A remaining step will be to relate the ϵ, N scaling (which worked well for Gargett et al. (1981) over $\kappa_0 < \kappa < \kappa_b$) and the Vortical spectral form to a dynamical model of the motions.

Figure Captions

Figure 1. The component wavenumber frequency spectrum of shear for the 70 kHz and 75 kHz sonars. A near inertial peak dominates the spectrum at low-frequency and wavenumber. At higher frequencies the wavenumber dependence of the spectrum becomes progressively more blue. No modeled noise is removed in this spectral estimate. The "noise correction" process has very little effect at frequencies below 1 cph.

Figure 2. The rotary wavenumber-frequency spectrum of shear. These estimates are obtained by combining information from the offshore and longshore sonars. No modeled noise is removed.

Figure 3. Cross-sections of the component wavenumber-frequency spectrum of shear at 1, 2, 4, 8, 16, 32 and 64 cpd. Spectral estimates are calculated at 20, 36, 68, 132, 260, 516 and 1028 degrees of freedom. Dotted lines give the spectrum as measured. Solid lines give an estimate of the spectrum with a modeled noise spectrum removed. The noise level chosen corresponds to 1.5 cm^2/sec^2 velocity noise variance. The sharp drop in the spectrum at vertical wavenumbers greater than $3x10^{-2}$ is a consequence of the finite resolution of the measurement. Any actual high wavenumber cut-off of the spectrum is not resolved in these measurements.

Figure 4. Cross-section of the rotary wavenumber-frequency spectrum of shear. The interpretation is as in Fig. 3.

Figure 5. Cumulative shear variance as a function of vertical wavenumber for the 70 and 75 kHz sonars. The contribution to the overall variance from frequencies 0.5 to 1, 0.5 to 2...0.5 to 64 cpd is given by the various lines. Dashed lines give the variance contribution as measured. Solid lines show the result of subtracting a modeled noise spectrum. The corresponding velocity noise level assumed is 1.5 cm^2/sec^2. The drop in spectral levels above $3x10^{-2}$ cpm is a consequence of the finite resolution of the measurement.

Figure 6. The component frequency spectrum of shear (top), the rotary frequency spectrum

(bottom). The modeled noise spectrum has been removed.

Figure 7. The inverse Richardson function $Ri^{-1}(\kappa,\omega)$ evaluated at frequencies 1, 2, 4...64 cpd. The dashed line gives the function with no modeled noise removed. The solid line indicates the result of subtracting a modeled noise spectrum from the shear spectral estimate.

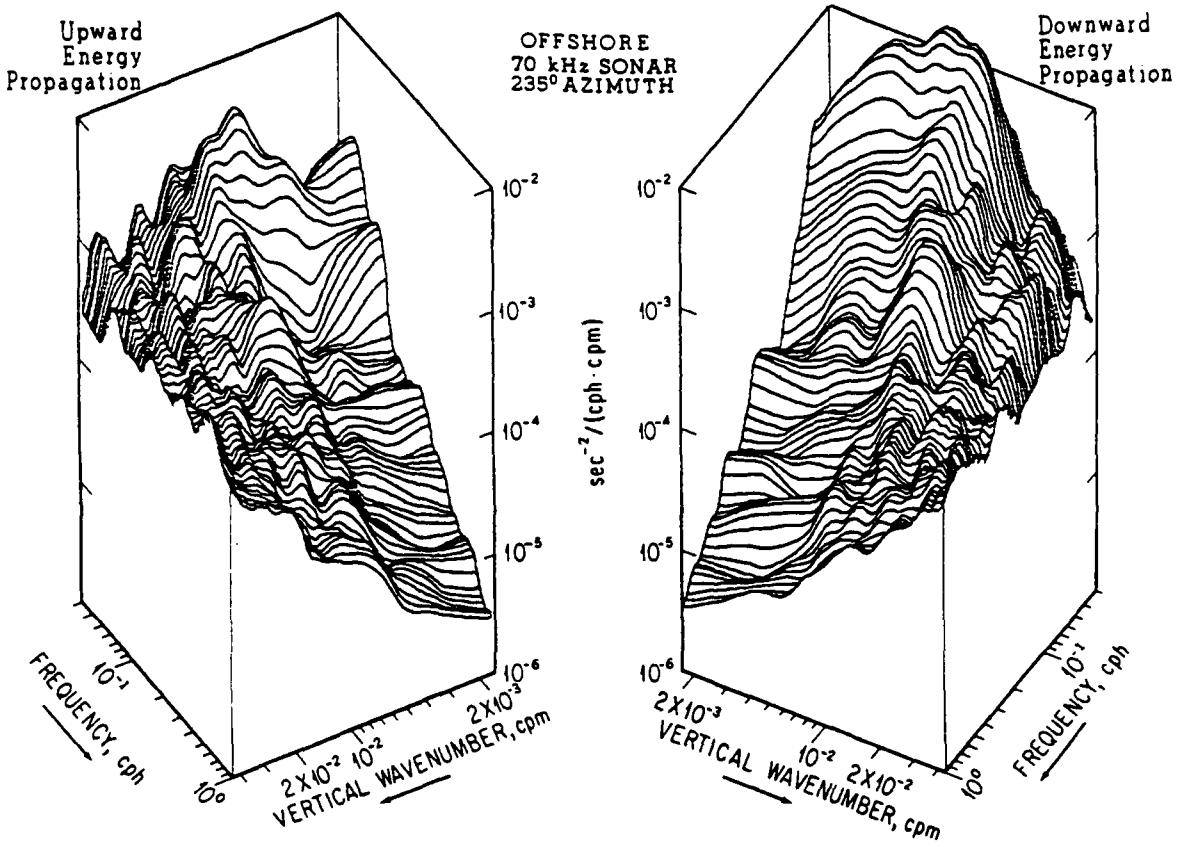
Upward
Energy
Propagation
OFFSHORE
70 kHz SONAR
235° AZIMUTH
Downward
Energy
Propagation
10^{-2}
10^{-3}
10^{-4}
10^{-5}
10^{-6}
$sec^{-2}/(cph \cdot cpm)$
FREQUENCY, cph
10^{-1}
10^{0}
$2X10^{-2}$ 10^{-2}
VERTICAL WAVENUMBER, cpm
$2X10^{-3}$
10^{-2} $2X10^{-2}$
VERTICAL WAVENUMBER, cpm
10^{0}
10^{-1}
FREQUENCY, cph

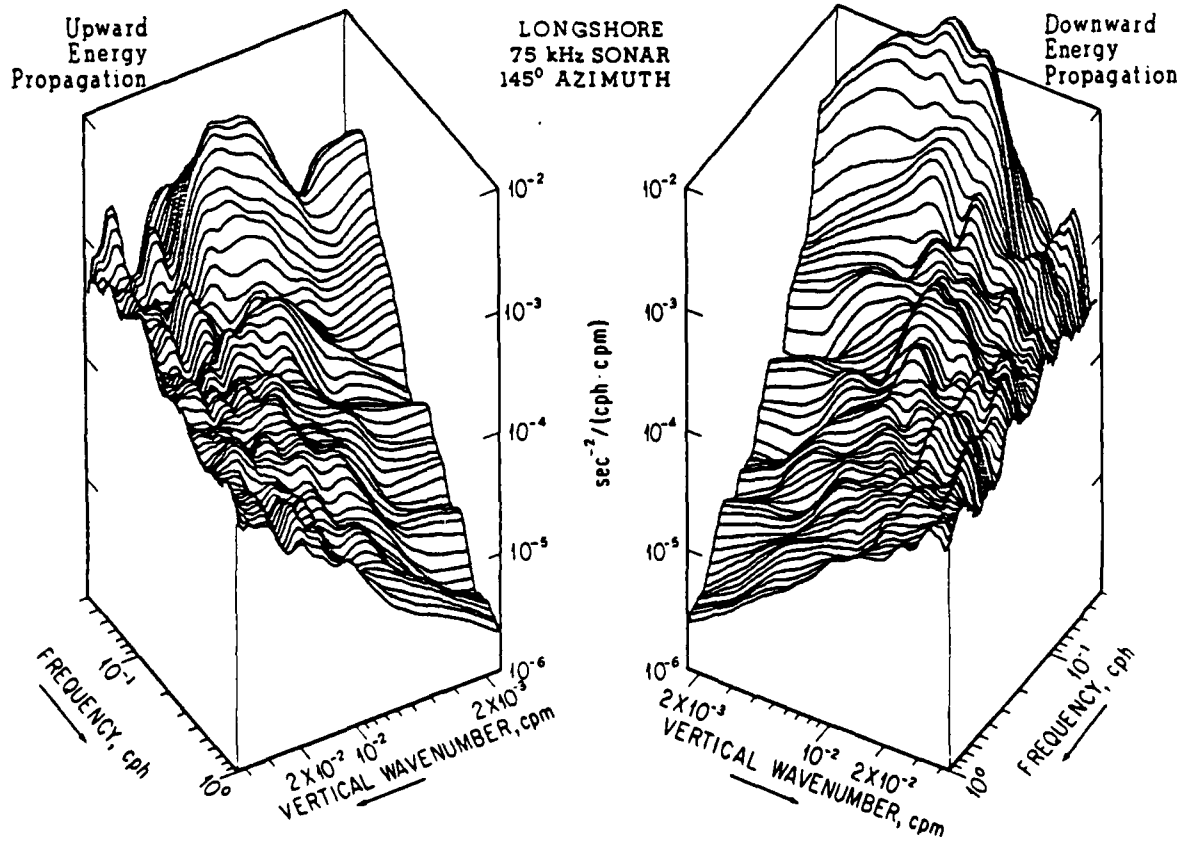
Upward
Energy
Propagation
LONGSHORE
75 kHz SONAR
145° AZIMUTH
Downward
Energy
Propagation
10^{-2}
10^{-3}
10^{-4}
10^{-5}
10^{-6}
$sec^{-2}/(cph \cdot cpm)$
FREQUENCY, cph
10^{-1}
10^{0}
$2X10^{-2}$ 10^{-2}
VERTICAL WAVENUMBER, cpm
$2X10^{-3}$
10^{-2} $2X10^{-2}$
VERTICAL WAVENUMBER, cpm
10^{0}
10^{-1}
FREQUENCY, cph

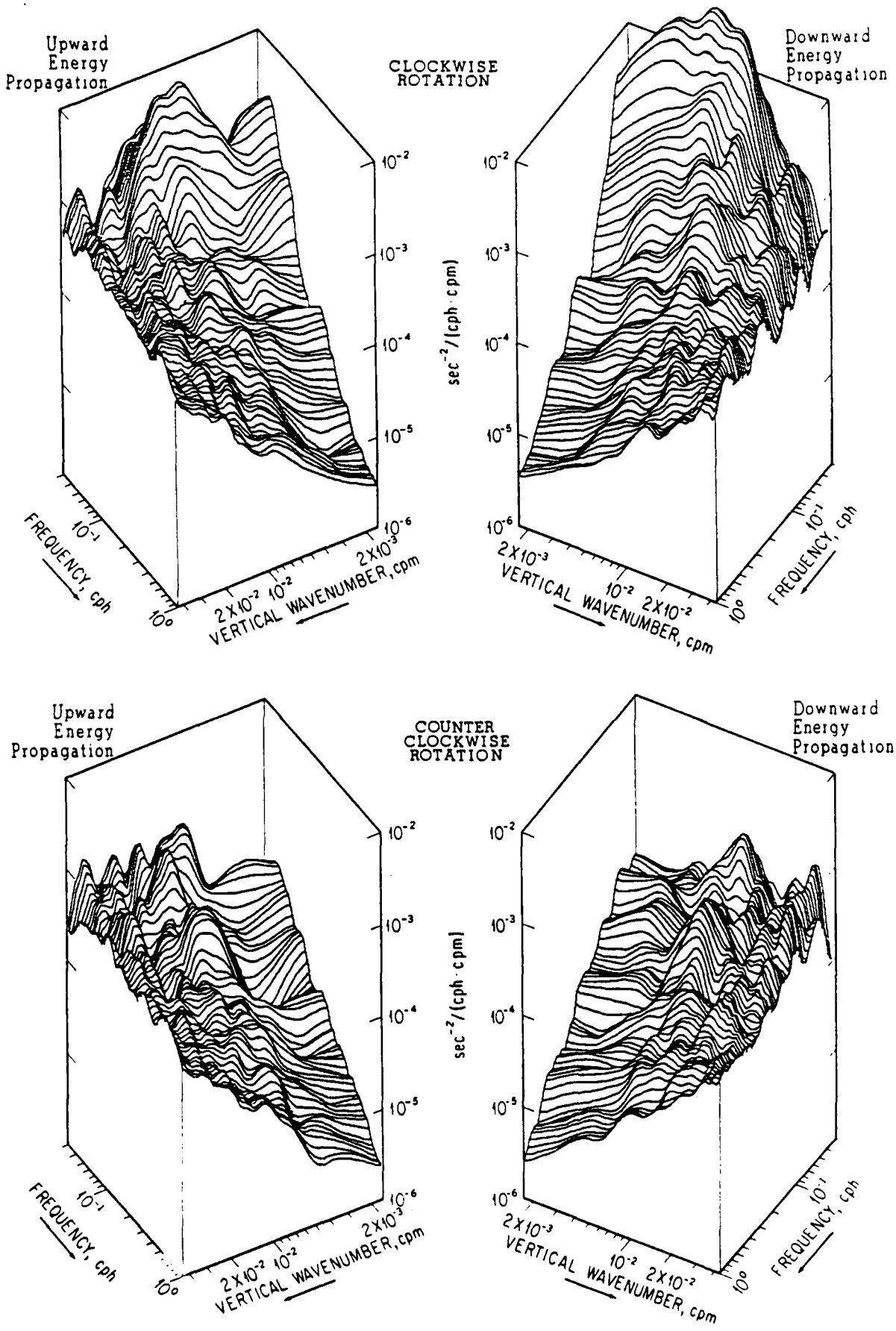
Upward
Energy
Propagation
CLOCKWISE
ROTATION
Downward
Energy
Propagation
10^{-2}
10^{-3}
10^{-4}
10^{-5}
10^{-6}
$sec^{-2}/(cph \cdot cpm)$
FREQUENCY, cph
10^{-1}
10^{0}
$2X10^{-2}$ 10^{-2}
VERTICAL WAVENUMBER, cpm
$2X10^{-3}$
10^{-2} $2X10^{-2}$
Upward
Energy
Propagation
COUNTER
CLOCKWISE
ROTATION
Downward
Energy
Propagation

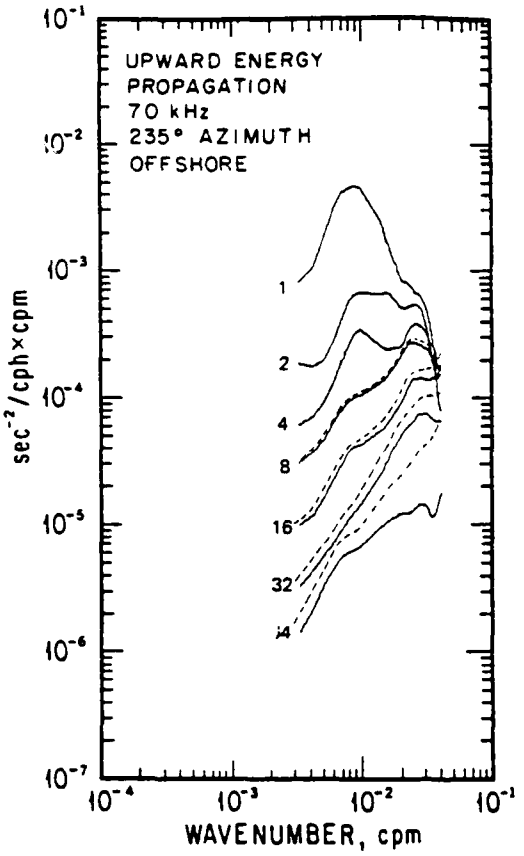
UPWARD ENERGY
PROPAGATION
70 kHz
235° AZIMUTH
OFFSHORE
1
2
4
8
16
32
64
sec⁻²/cph×cpm
WAVENUMBER, cpm

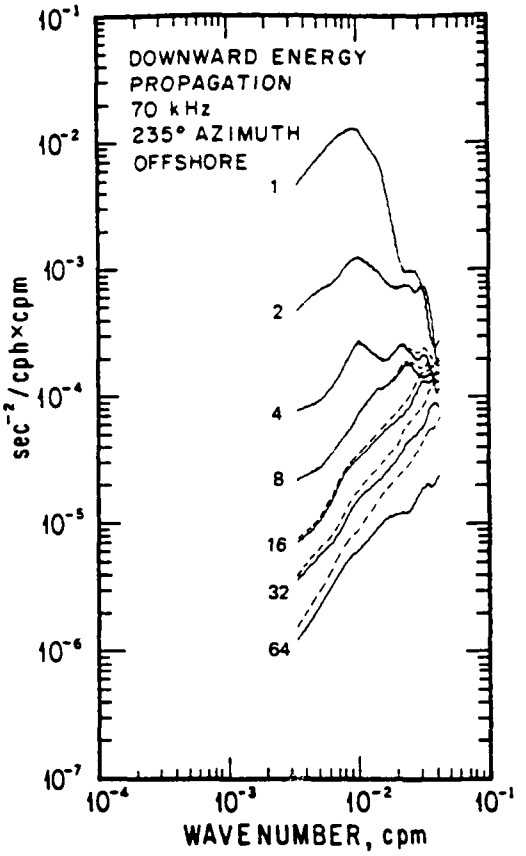
DOWNWARD ENERGY
PROPAGATION
70 kHz
235° AZIMUTH
OFFSHORE
1
2
4
8
16
32
64
sec⁻²/cph×cpm
WAVENUMBER, cpm

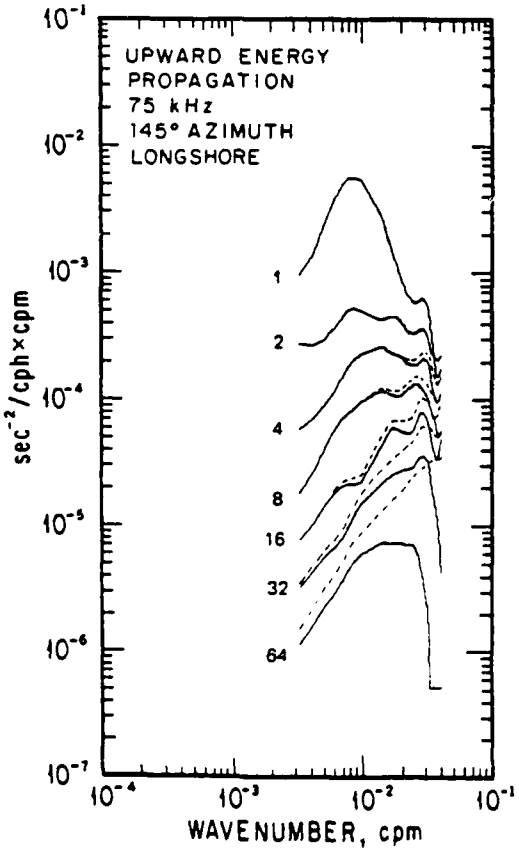
UPWARD ENERGY
PROPAGATION
75 kHz
145° AZIMUTH
LONGSHORE
1
2
4
8
16
32
64
sec⁻²/cph×cpm
WAVENUMBER, cpm

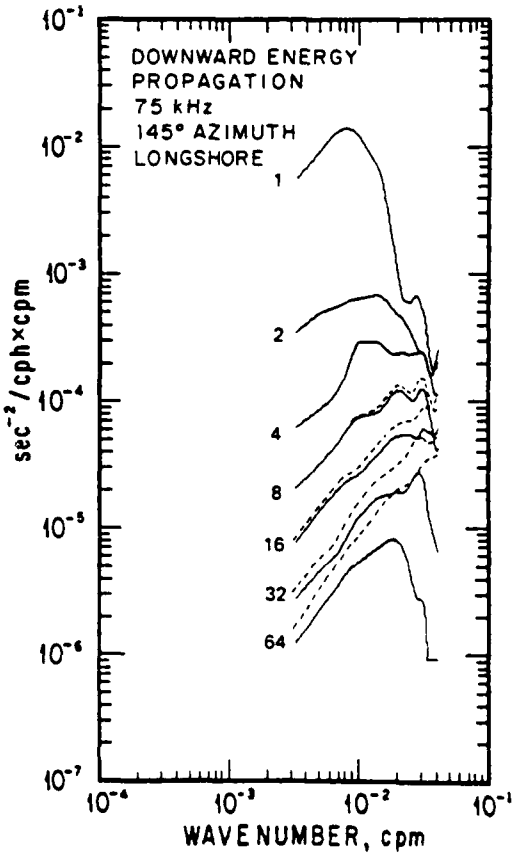
DOWNWARD ENERGY
PROPAGATION
75 kHz
145° AZIMUTH
LONGSHORE
1
2
4
8
16
32
64
sec⁻²/cph×cpm
WAVENUMBER, cpm

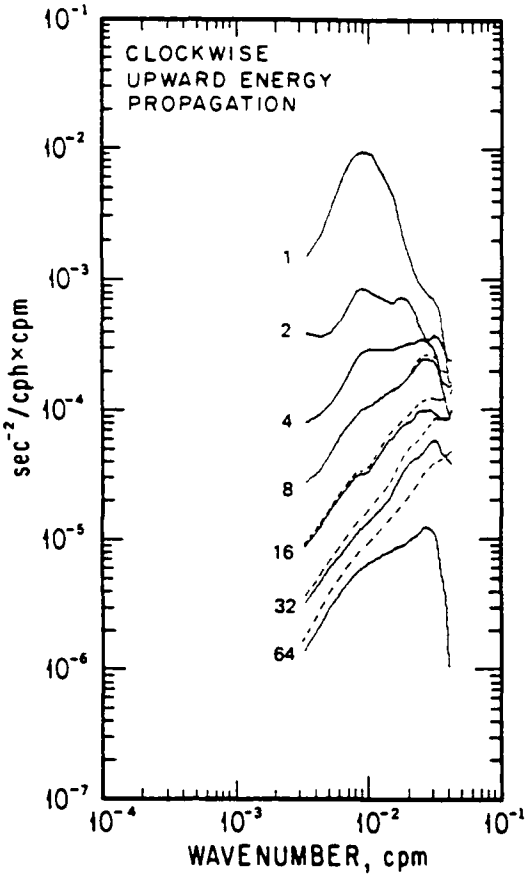
CLOCKWISE
UPWARD ENERGY
PROPAGATION
1
2
4
8
16
32
64
sec⁻²/cph×cpm
WAVENUMBER, cpm

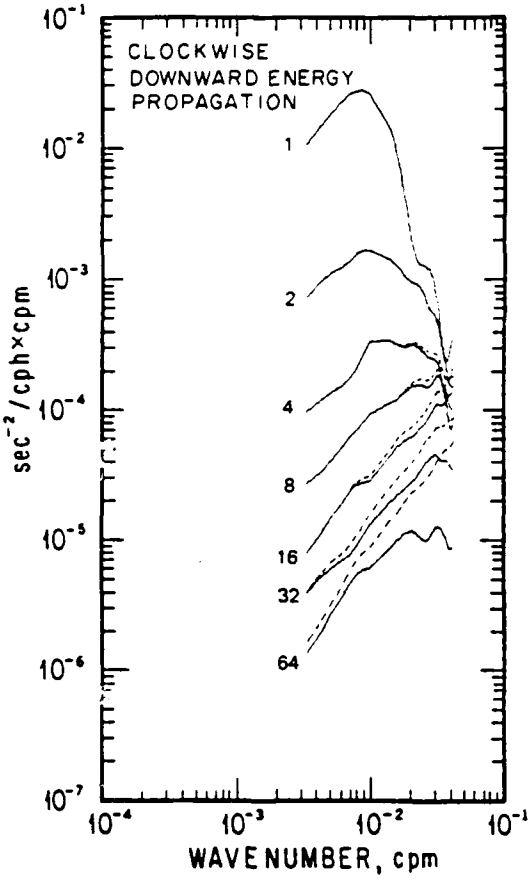
CLOCKWISE
DOWNWARD ENERGY
PROPAGATION
1
2
4
8
16
32
64
sec⁻²/cph×cpm
WAVENUMBER, cpm

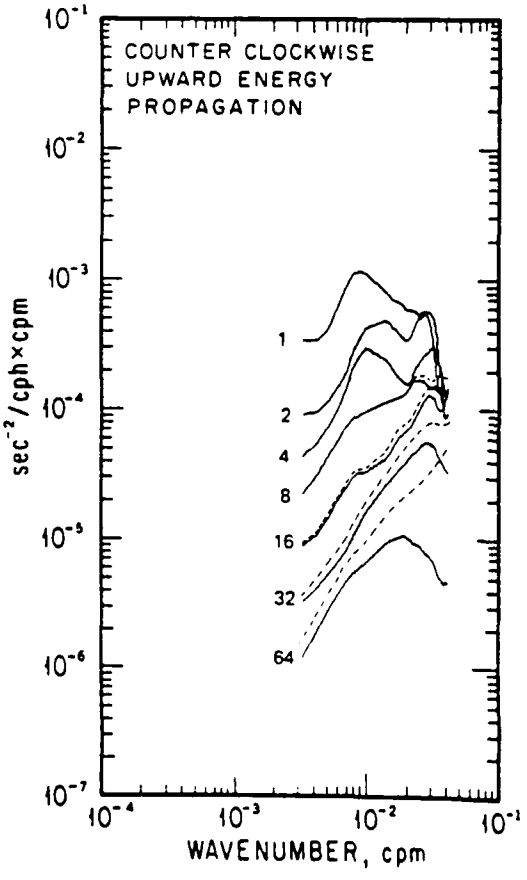
COUNTER CLOCKWISE
UPWARD ENERGY
PROPAGATION
1
2
4
8
16
32
64
sec⁻²/cph×cpm
WAVENUMBER, cpm

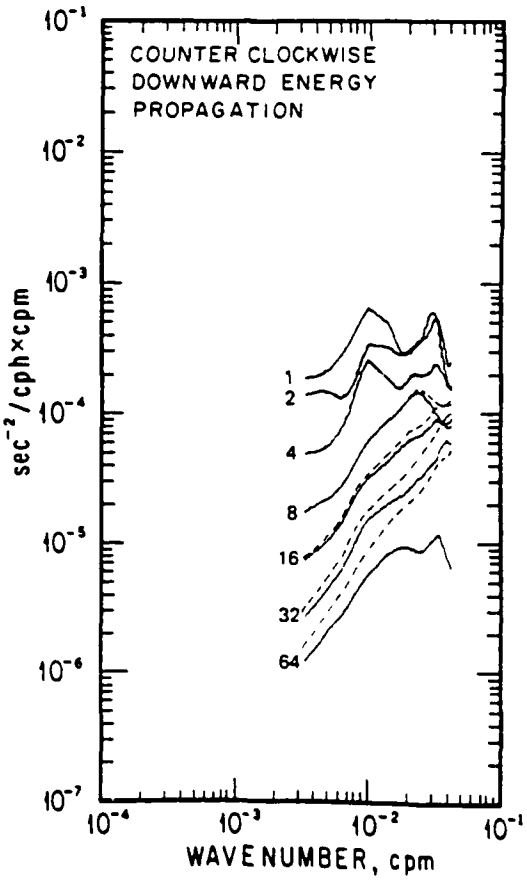
COUNTER CLOCKWISE
DOWNWARD ENERGY
PROPAGATION
1
2
4
8
16
32
64
sec⁻²/cph×cpm
WAVENUMBER, cpm

AD-A153 860 ENVIRONMENTAL BACKGROUND MEASUREMENT PROGRAM(U) SCRIPPS 2/2
INSTITUTION OF OCEANOGRAPHY LA JOLLA CA MARINE PHYSICAL
LAB K M WATSON ET AL. 15 FEB 85 MPL-U-7/85
UNCLASSIFIED N00014-79-C-0983 F/G 8/10 NL

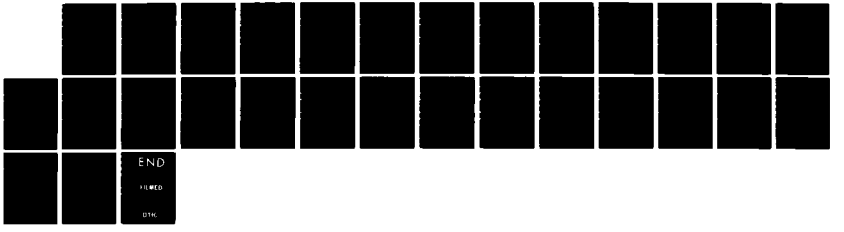

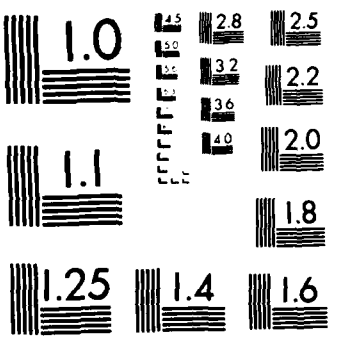

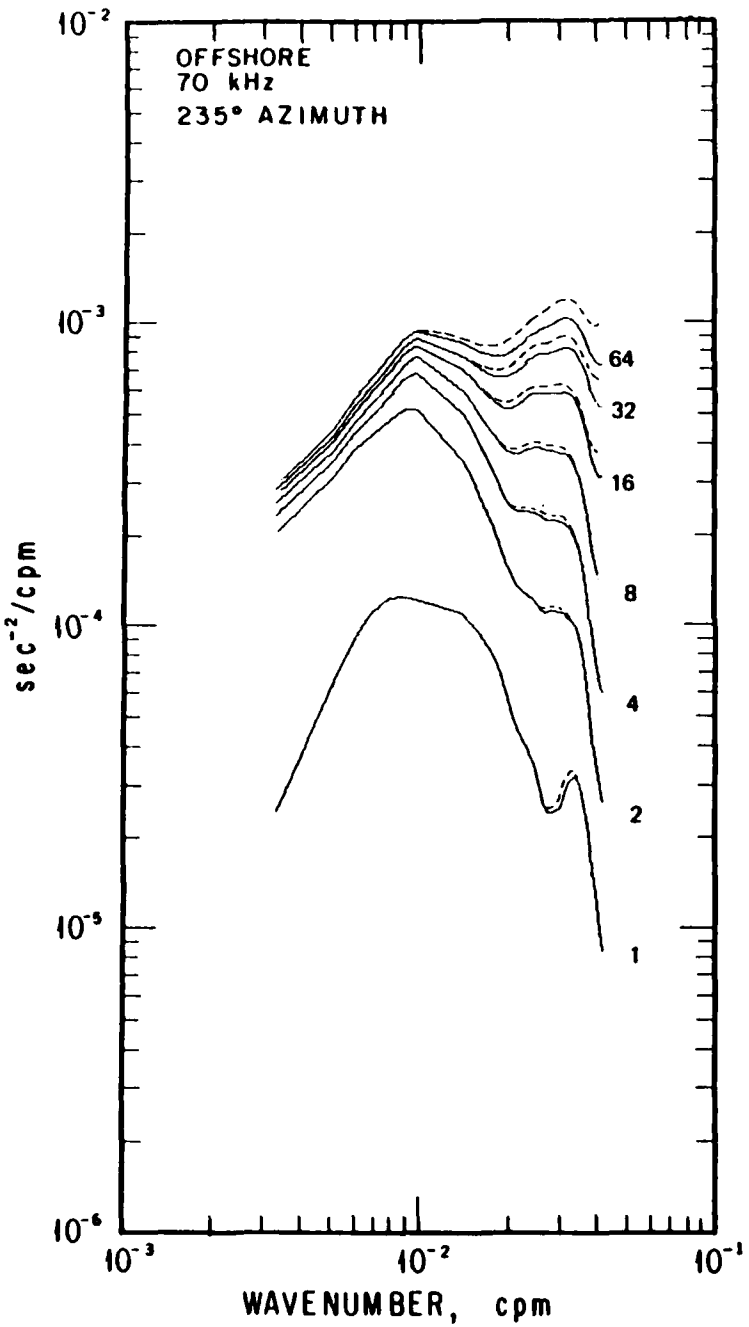
OFFSHORE
70 kHz
235° AZIMUTH
10^{-2}
10^{-3}
10^{-4}
10^{-5}
10^{-6}
sec^{-2}/cpm
64
32
16
8
4
2
1
10^{-3}
10^{-2}
10^{-1}
WAVENUMBER, cpm

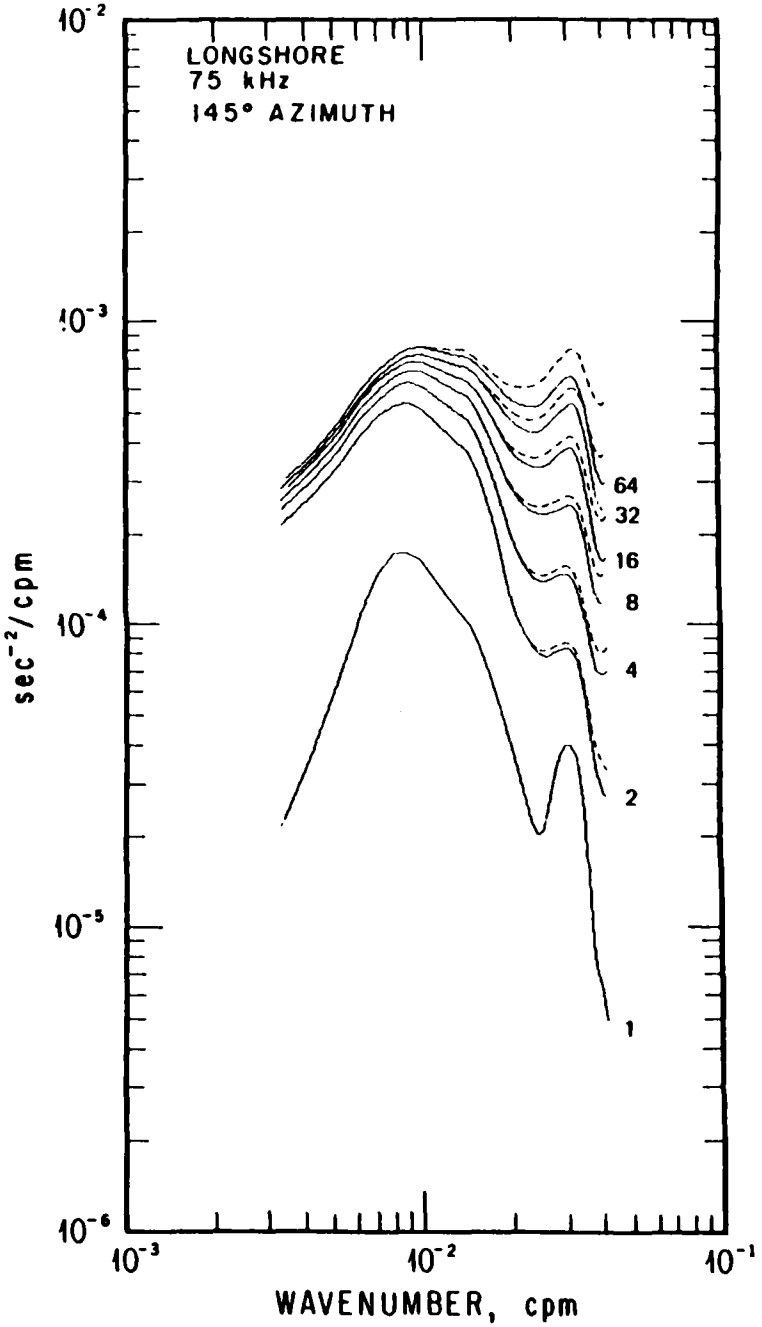
LONGSHORE
75 kHz
145° AZIMUTH
10^{-2}
10^{-3}
10^{-4}
10^{-5}
10^{-6}
sec^{-2}/cpm
64
32
16
8
4
2
1
10^{-3}
10^{-2}
10^{-1}
WAVENUMBER, cpm

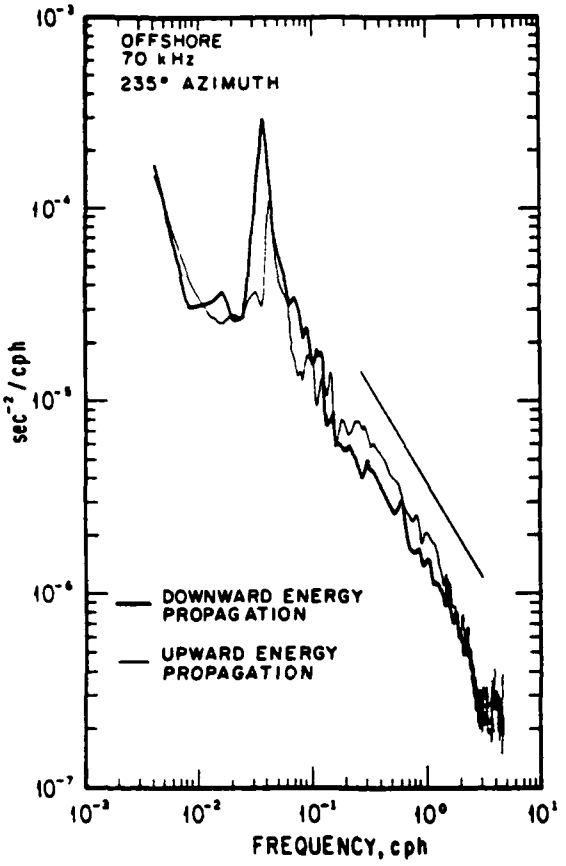
OFFSHORE
70 kHz
235° AZIMUTH
DOWNWARD ENERGY PROPAGATION
UPWARD ENERGY PROPAGATION
sec⁻²/cph
FREQUENCY, cph

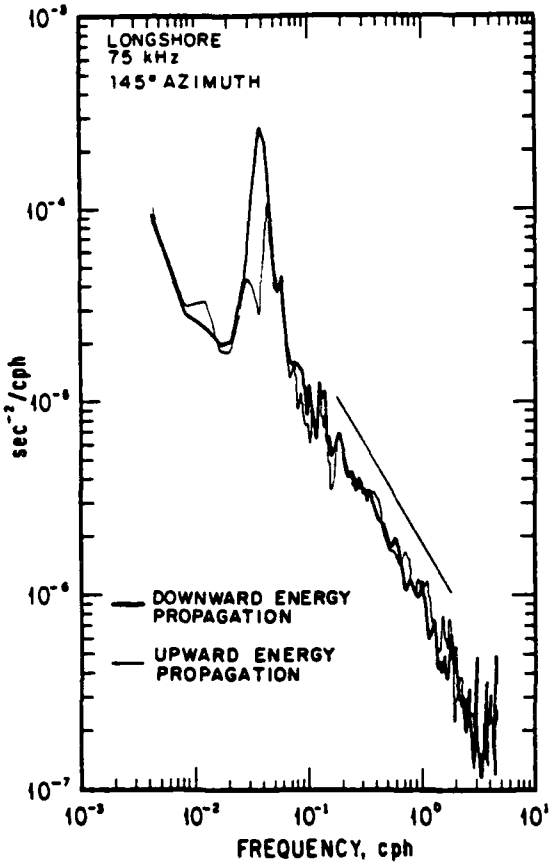
LONGSHORE
75 kHz
145° AZIMUTH
DOWNWARD ENERGY PROPAGATION
UPWARD ENERGY PROPAGATION
sec⁻²/cph
FREQUENCY, cph

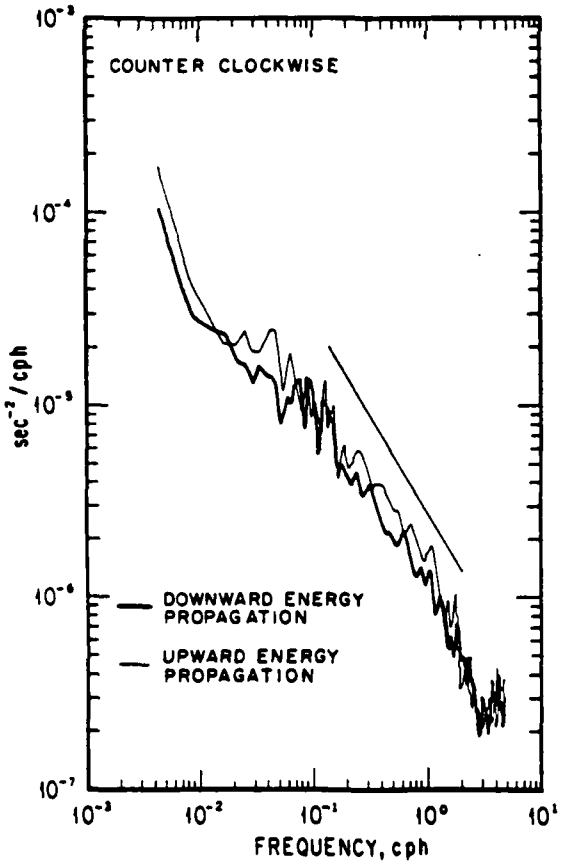
COUNTER CLOCKWISE
DOWNWARD ENERGY PROPAGATION
UPWARD ENERGY PROPAGATION
sec⁻²/cph
FREQUENCY, cph

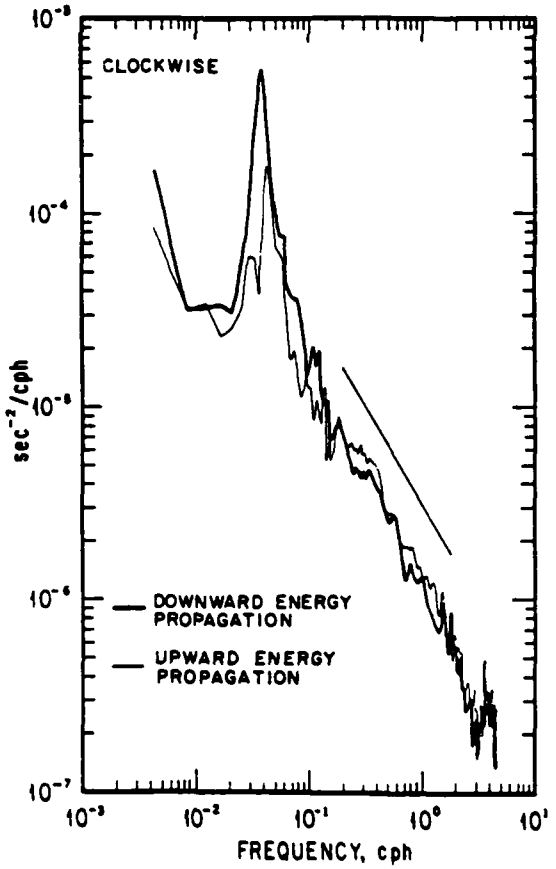
CLOCKWISE
DOWNWARD ENERGY PROPAGATION
UPWARD ENERGY PROPAGATION
sec⁻²/cph
FREQUENCY, cph

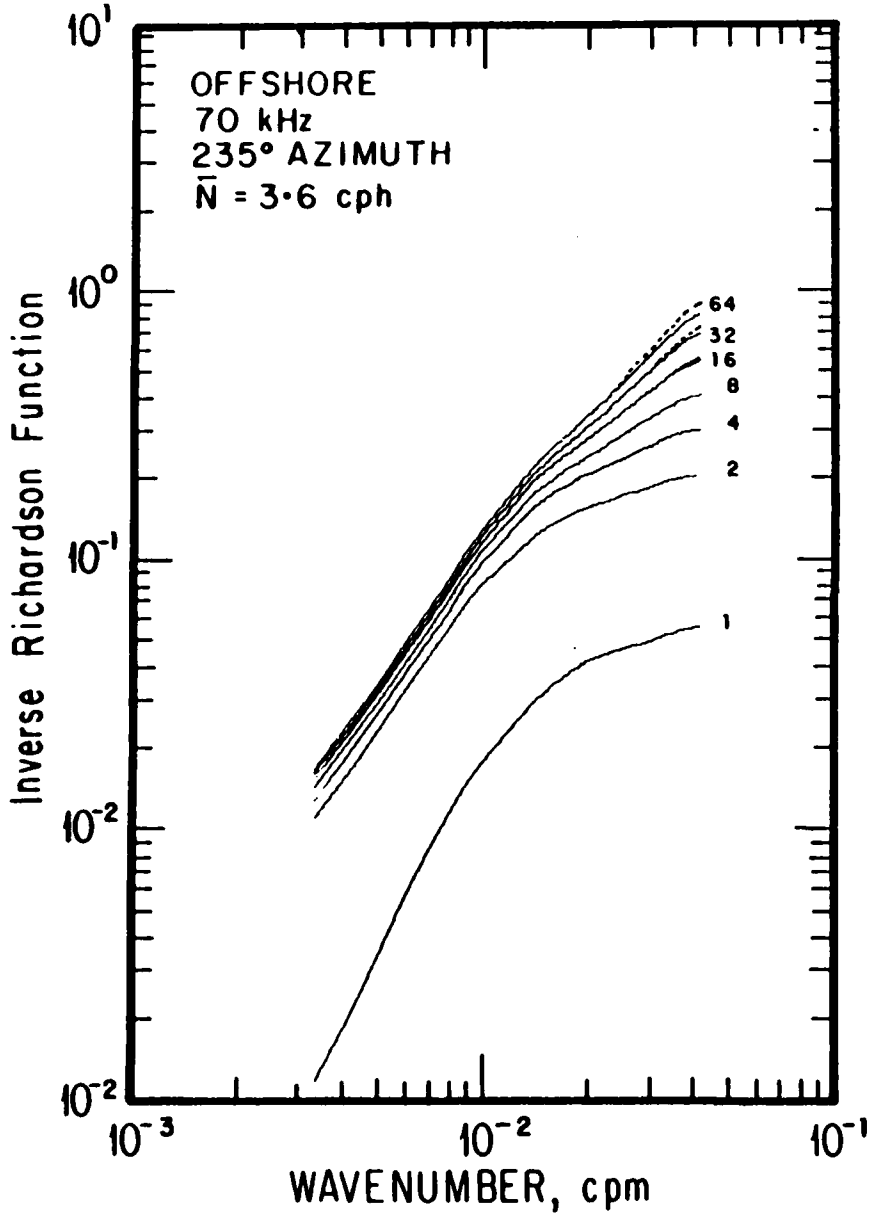
OFFSHORE
70 kHz
235° AZIMUTH
$\bar{N}$ = 3·6 cph
Inverse Richardson Function
WAVENUMBER, cpm
64
32
16
8
4
2
1

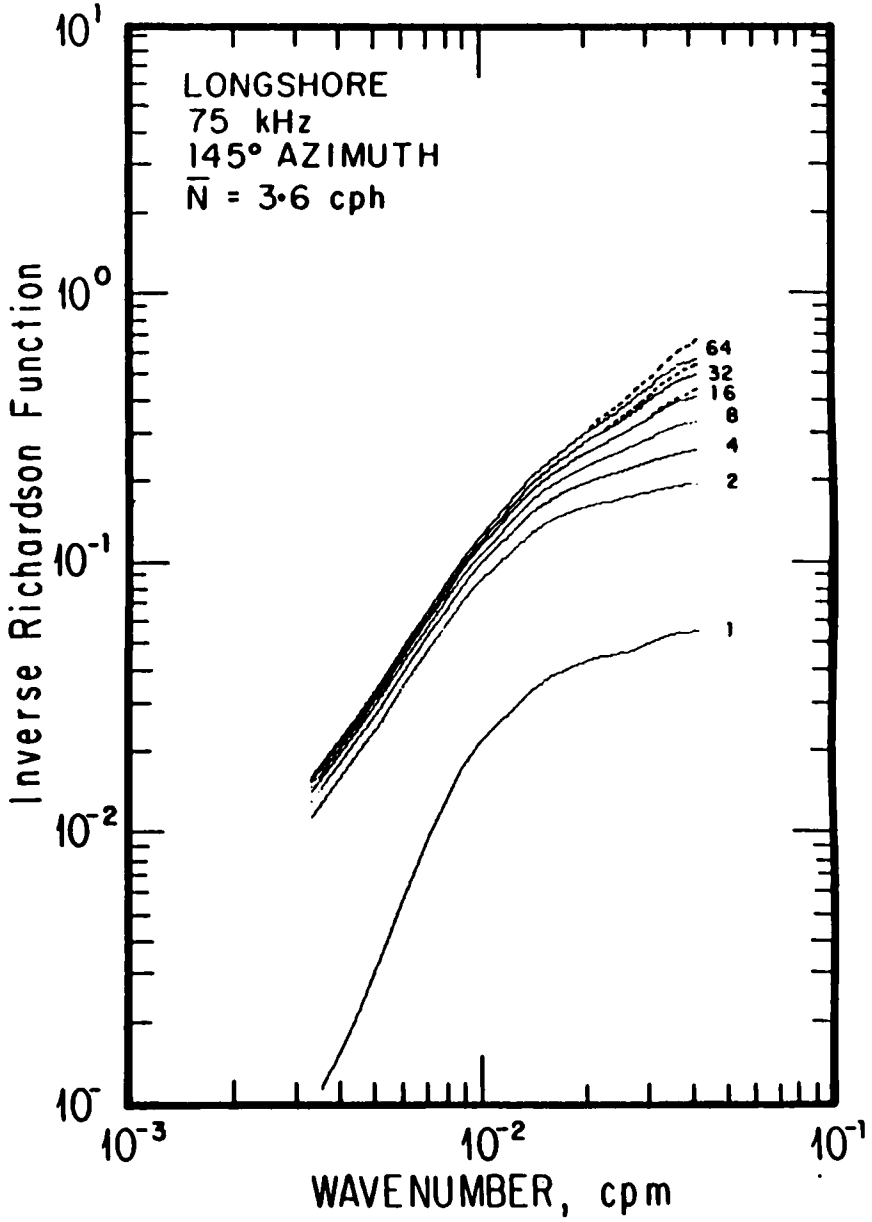
LONGSHORE
75 kHz
145° AZIMUTH
$\bar{N}$ = 3·6 cph
Inverse Richardson Function
WAVENUMBER, cpm
64
32
16
8
4
2
1

II. DESIGN OF A SEA FLOOR WORK SYSTEM

Principal Investigator: Victor C. Anderson
Total Amount of Award: $190,000

Appendix A

APPENDIX A

MPL TECHNICAL MEMORANDUM 364

RUM III

VEHICLE CONTROL SYSTEM DESCRIPTION

Richard E. Currier

Marine Physical Laboratory

Scripps Institution of Oceanography
University of California, San Diego

January 30, 1984

ABSTRACT

The hardware and software design of a control system for the RUM III vehicle project is described. The functional requirements, design constraints, and system configuration are first examined. A detailed description of the hardware systems and their corresponding software components follows.

MPL-U-15/84

1. INTRODUCTION

Rum III is a tethered, remotely operated submersible vehicle capable of operating in both a deep/towed and bottom crawling mode at depths of up to 6000 meters. This report describes the peripheral hardware currently scheduled for inclusion on the vehicle including a manipulator boom, camera and sonar systems, thrusters, and various sensors along with a description of the software necessary to allow full operator control over these systems and others that may be included. Also described is a shipboard software development system that may be used to aid both vehicle software development and any ancillary scientific projects.

2. OVERVIEW

2.1. FUNCTIONAL REQUIREMENTS

There are four functional requirements which are the basis for the RUM III Vehicle Control System Design. They are described in the following paragraphs.

1) **Format and Transmit Operator Commands to the Vehicle.**

This includes commands for the operation of the basic vehicle and its sensor systems, and for the operation of whatever mission related devices may be mounted on the vehicle during a particular operation.

In the present implementation all commands are entered via the Operator CRT. Eventually an Operator Console with joysticks and other dedicated control input devices will be provided.

2) **Format and Transmit Sensor Information to the Operator Displays.**

Sensors include video and sonar systems as well as transducers for vehicle status (positions, speeds, voltages, etc.), for environmental parameters, and for the mission related devices.

3) **Provide Fail-Soft Capability.**

This will allow reduced-capability operation in the event of partial system failures, with particular attention to the safe recovery of the vehicle and its scientific payload. Emphasis is on providing alternate data paths for critical command and sensor information, alternate microprocessor control of various functions, and on returning the vehicle controls to a safe state in the event of a loss of all command channels. This includes providing the capability of stowing the manipulator and experimental devices for safe vehicle recovery.

4) **Incorporate Computer-Aided Operator Control.**

Operator aids will include graphic displays to aid in navigation and manipulator control, automatic positioning of television cameras to follow manipulator actions, implementation of high level operator commands (e.g. move the manipulator to a specified position), automatic repetition of a stored sequence of commands executed once by the operator, etc. In the initial system, the Operator Console functions will be carried out by the Operator CRT. The Operator Console functions will be added as operating experience indicates what features and functions will be most useful. The system will be designed so that extented functions can be included through modular additions to the software and hardware.

2.2. DESIGN CONSTRAINTS AND GOALS

a) **Cable Bandwidth Limitation.**

Only a limited amount of information may be transmitted between the vehicle and the shipboard Console Telemetry Processor per unit time. This limitation is most important with respect to the video data and to a somewhat lesser extent to the sonar systems. The other sensor data to the shipboard system and command information to the vehicle do not require a large fraction of the available bandwidth and so are not limited in this way. Much of the design effort has been directed at making the best use of the available bandwidth by providing a flexible format for the video and sonar data, in order to allow tradeoffs based on particular operating conditions.

b) **Expandability and Modularity.**

The design approach separates the system into functional modules with carefully defined interfaces. This will facilitate the design and checkout of the first, minimal system and will allow an orderly inclusion of enhancements. It will also simplify the design of devices required for particular missions and experiments. This philosophy applies to both the hardware and software aspects of the system design.

2.3. SYSTEM CONFIGURATION

The RUM III vehicle control system consists of a network of several microcomputer sub-systems and telemetry links providing for transmission of command, status, and other data between the microcomputers in the vehicle and those on board the ship. (see Fig 1.) Each computer fills a particular role in the organization of the system. The major components of the system are described in the following paragraphs.

a) **The Software Development Computer(SDC)**

The primary purpose of the software development computer is to provide an efficient environment for the software design and implementation of the RUM III control system. In order to achieve this goal the system must be able to support high level and assembly language program development along with the support functions necessary to compile, assemble, link and download the resulting products to the target systems. It may also be used for data analysis, navigation and engineering support, and as a general computational tool for any scientific tasks that may arise during a mission in the field.

b) **The Console Telemetry Processor(CTP)**

The CTP interfaces the Operator Console and Operator CRT to the system along with providing a bi-directional path from the SDC to the Telemetry Link and the vehicle, which is needed for program downloading, video and sonar uploading and similar functions. The control software that corresponds to each Vehicle Peripheral Processor will reside here along with all system software necessary to interface with the telemetry interface to the vehicle data node, the operator console, and the monitor system.

c) **The Command and Status Link(CSL)**

This bi-directional link carries commands from the shipboard CTP system to the Vehicle Data Node on the vehicle to be distributed to the VPP's and carries data up the link in the reverse direction.

d) **The Vehicle Data Node(VDN)**

The VDN is a central switching point for communications between the CTP, the VPP's and the VTP. It is responsible for coordinating the bi-directional data flow between vehicle systems and the shipboard systems.

e) **The Vehicle Peripheral Processors(VPP's).**

The actual control of the various physical devices of the RUM III control system is done by the VPP's. Here commands received from the shipboard system are translated into the outputs necessary to control the manipulator, thrusters, TV and sonar systems, TV scanner, the tracks , and the on-board VTP processor.

f) **The Vehicle Telemetry Processor(VTP)**

The VTP serves a dual purpose. First, it may be used to pre-process wide-band data such as video and sonar signals for more efficient uploading to the CTP over the limited bandwidth High Speed Telemetry Link. In addition, it may be used as a more powerful on-board processor for the VPP control functions. This latter function gives the system some built in redundancy as the VTP may contain the software to take over the functions of the VDN if a hardware failure is encountered.

g) **The High Speed Data Link(HSDL)**

The High Speed Data Link carries information from the vehicle video and sonar systems to the shipboard CTP system.

3. COMPUTER SYSTEMS

3.1. SOFTWARE DEVELOPMENT COMPUTER (SDC)

3.1.1. CPU

An LSI 11/23 computer is used as the development system. The Digital Equipment Corporation's LSI-11 series of microcomputers is based on the PDP-11 minicomputer system that preceded it. The LSI-11 is very much like a PDP-11 in its register and memory operational formats. One half megabyte of RAM parity memory is provided. The MSV11-PL memory has parity generation and checking and read and write access times of 250ns and 90ns respectively. (see Fig. 2)

3.1.2. BUS STRUCTURE

The LSI-11, or "Q" bus structure is used to interface all hardware system modules in the SDC. The LSI-11 bus is an asynchronous, 16-bit transfer-oriented bus. Data transfer is based on handshaking between devices and no master clock lines are used. This feature allows a wide range of different-speed peripherals to be placed on the bus. The bus also has a number of sophisticated features not normally found in a microcomputer. A power available (BPOK H) and dc power available (BDCOK H) line from the power supply are meant to automatically reset the processor as power is applied and to initiate a power failure routine that saves registers in nonvolatile memory when the power gets too low. This power fail-restart is a standard feature on most large mainframes.

The choice of the LSI-11 bus was motivated by the large variety of peripherals available and the support of full 22 bit addressing. All LSI-11 modules connected to this common bi-directional bus structure receive the same

interface signal lines. With bi-directional and asynchronous communications on the LSI-11 bus, devices can send, receive, and exchange data at their own rates. The bi-directional nature of the bus allows the use of common bus interfaces for different devices and simplifies the interface design.

3.1.3. SDC PERIPHERALS

3.1.3.1. WINCHESTER DISK

A Winchester hard disk is supported. The Cynthia D 160 is a moving head, fixed media disk drive with a data capacity of 120 megabytes. The DTC-2101 Disk Drive Controller is a bi-polar microprocessor-based controller that is able to control one radial interface type disk drive. Due to the micro-programmed approach utilized in the controller, extensive diagnostic capabilities are implemented. This methodology increases fault isolation efficiency and reduces system down time.

Commands are issued to the controller through a DTC-11-1 Host Adapter that fits into a single, dual-wide LSI-11 Bus slot in the STP host computer. The Host Adapter and the Disk Drive Controller together comprise one part of a disk storage subsystem. The controller accepts data from the host adapter and transfers the data to the correct location on the disk. In addition, the controller will detect/correct burst errors from the fixed disk drive before data is transferred to the computer.

3.1.3.2. CIPHER TAPE

A Western Peripherals tape coupler interfaces a Cipher magnetic tape drive and formatter to the LSI-11 bus. The Cipher tape is used for disk backup, software storage, and to load external software such as the Unix operating system.

3.1.3.3. DLV11-J SERIAL INTERFACE

The DLV11-J is a 4-channel asynchronous serial line unit used to interface peripheral equipment to the LSI-11 bus. The interface transmits and receives data from the peripheral device over EAI RS-232C data lines. Each of the four serial ports on this module are separate and independent from the others. Each port has its own CSR's, data buffer, interrupt vectors, baud rate, UART, etc. and may be independently configured.

In this application the device is configured to support two VT-100 CRT's, one serial link to the Console Telemetry Processor, and an Okidata serial printer.

3.1.4. SOFTWARE

The principal software development tool is the Berkeley version 2.9 UNIX operating system. UNIX provides a powerful program development environment which includes many utilities useful for software design and implementation and document preparation.

Two utilities are also supported to produce code for the MC68000 and 6502 microprocessors:

A cross-compiler for the MC68000 from Alcyon Inc. supports the "C" programming language as well as an assembler, linker-loader, and down-loader. The principal use of this cross-compiler is the development of applications programs and the user interfaces necessary to provide control over the software that will reside in the two MC68000 based sub-systems: the CTP and the VTP.

A Fortran cross-assembler for the 6502 is used to generate software for the VDN and the various VPP's.

3.2. CONSOLE TELEMETRY PROCESSOR (CTP)

3.2.1. CPU

An Integrated Solutions IS-68K, LSI-11 Bus compatible MC68000-based CPU board is used as the CTP.

The IS-68K card allows the use of the Motorola MC68000 processor with the large variety of peripherals available on the LSI-11 bus. It combines up to 1 megabyte of parity memory, up to 32k bytes of EPROM, and two high speed serial ports with programmable baud rates on a single Quad form factor card.

256k on-board memory are provided. The board chosen will operate at 10 MHz with no wait states out of the on-board and local bus expansion memory. Dual porting the on-board and local bus memory permits all on-board and local bus memory to be accessed by DMA devices on the LSI-11 bus and also permits the MC68000 to continue operating while DMA transfers are underway. The MC68000 continues executing at full speed while DMA transfers are occurring to LSI-11 bus memory. It continues executing at reduced speed if DMA accesses to on-board/local bus memory are made, while memory accesses are automatically arbitrated between the MC68000 and the DMA bus master.

3.2.2. BUS STRUCTURE

The system bus of the IS-68K is LSI-11 compatible. It meets all requirements of DEC STD 160 with 22-bit addressing. The use of this bus structure for both the SDC and the CTP provides great flexibility in system configuration as *various peripherals, memory, etc. can be attached to either system.*

3.2.3. MEMORY MANAGEMENT

The IS-68K board contains two levels of memory management, a segmentation front end and a paging back end. Each software process can have from 1 to 64 segments associated with it. Segments contain from 1 to 16 4k byte pages. Support for demand paging through page accessed and page modified bits is associated with each page. These bits are automatically updated by hardware on each page reference. This scheme is similar to one used by several large mainframe computer systems.

3.2.4. LOCAL MEMORY BUS

The on-board memory is expandable to 4 Mbytes over the local memory bus. Local memory, as well as on-board memory, runs with no wait states. All local memory is accessible from the LSI-11 bus through the two port memory arbitrator.

3.2.5. CTP PERIPHERALS

3.2.5.1. OPERATOR CRT

The Operator CRT is the primary interface between the Operator and the Rum III Control System. From this device, the operator is able to control all hardware and software systems. In addition, the operator may choose from a selection of formatted displays that provide information on the status of all systems.

3.2.5.2. OPERATOR CONSOLE

The Operator Console accepts operator inputs from pushbuttons, joysticks, etc., and formats commands to the vehicle. Status information from the vehicle is interpreted and the console's displays are updated as required.

In the initial configuration, the Operator Console will be simulated in software. The inputs and outputs will be controlled by the Operator through the Operator CRT. This will allow early testing of the system without a major hardware effort being undertaken before the actual needs of the system are known. When the requirements of the Operator Console are adequately defined, the console hardware will be built. The simulations will then be available as a backup console if ever needed due to a hardware breakdown.

3.2.5.3. SERIAL PORTS

The two serial ports on the board support both either RS-232/C compatible asynchronous communication or RS-422 balanced synchronous communication with external clocking. Both channels offer full modem control support while in asynchronous mode and limited modem control support in synchronous mode. The channels can be independently configured for synchronous or asynchronous communications. In the present configuration, one serial port will be used to down-load software from the CTP and the other for an Operator CRT.

3.2.6. SOFTWARE

3.2.6.1. OPERATING SYSTEM

The CTP is provided with a VRTX/68000 "Versatile Real-Time Executive", a silicon software component for embedded microprocessors donated to the Regents of the University of California by Hunter and Ready Inc. of Palo Alto California. A silicon software component is an executable version of a microprocessor program that can operate on all board-level microcomputers that use the same type of microprocessor. Because the code has built in hooks to make it work with custom board designs, the component can be delivered in Read-Only memory (ROM). For the RUM III application, the VRTX will be copied onto a pair of 2764 EPROMs along with the MACSBUG monitor provided with the IS-68K board. This will allow the use of the down-loading, I/O, initialization, and debugging features of the monitor while the VRTX executive may be engaged by a simple MACSBUG command.

The VRTX executive provides a set of mechanisms necessary to support real-time systems. These mechanisms may be used as building blocks which can be connected to other pieces of software in a variety of designs tailored to the RUM III application.

The features include:

a) **Multitasking support.**

VRTX is designed to support real-time systems by providing a set of basic mechanisms for implementing multitasking.

Real-time systems are designed to perform seemingly unrelated functions in a nonsequential manner, thereby utilizing the processor and I/O devices more efficiently. Examples of common processing situations that lend themselves to this sort of control philosophy include listening for input from several devices at the same time, reading or writing a block of data while simultaneously performing arithmetic computations, and implementing sophisticated communications applications. The RUM III control system contains a number of such situations

and benefits greatly from existing in a multitasking environment. The Operator CRT and Operator Console must be serviced quickly to provide adequate operator control over the system, but this may be done efficiently in parallel with the transfer of data over the telemetry links. The physical operation of various devices such as the focusing of a TV camera, the moving of the manipulator boom, and activation of the sonar system may proceed without host CPU time while being adequately serviced on an interrupt basis.

b) **Interrupt-driven, priority-based scheduling.**

VRTX is an event driven operating system in that interrupt driven events from the real-world environment may initiate rescheduling by raising or lowering the priorities of various tasks. The Operator CRT for example may be serviced by a high priority task so that characters will not be lost from the keyboard, while the downloading of a command to the manipulator boom will not be adversely affected by a few msec wait possibly produced by running at a lower priority than the keyboard.

c) **Intertask communication and synchronization.**

Even though tasks operate asynchronously, it is often desirable for one task to pass information to another task. VRTX provides the mechanisms for sending and receiving long-word, non-zero messages in agreed-upon memory locations. The messages may contain the information in themselves or they may be pointers to larger messages in agreed upon buffer areas.

Synchronization between tasks can also be implemented by causing tasks to pend and unpend at a specified location while waiting for a message from another task or device.

d) **Dynamic memory allocation.**

A task's demand for memory varies over the course of its execution, and different tasks usually have different requirements. Consequently, a memory allocation policy must be established, and mechanisms in the operating system must exist to implement that policy. VRTX treats RAM memory as a resource and allocates that resource among competing tasks, just as it allocates control of the CPU among competing tasks. VRTX gives every task a fixed-size stack and dynamically allocates the rest of user RAM in blocks. Users are able to dynamically create memory partitions to mirror the often discontiguous chunks that make up the actual physical organization of memory. The block size of the original partition and the user stack size are set by the user at initialization time.

e) **Real-time clock control, with optional time-slicing.**

In order to make use of these features, the user provides a hardware-dependent interrupt service routine for each device supported. VRTX, in turn, manages all the logical operations needed to provide user application tasks with a full repertoire of associated clock management and character I/O commands.

f) **Character I/O support.**

VRTX provides the basic system calls to support a single front panel like character I/O device. The RUM III control system will use these to service the Operator CRT. Further, the user may implement multi-port I/O via user-defined system calls.

g) **Real-time responsiveness.**

A real-time system must be able to respond quickly to externally generated interrupts. VRTX provides the means by which user-supplied interrupt service routines can influence the scheduling of critical tasks.

With these features, VRTX/68000 provides a strong foundation for real-time, multitasking application systems. It relieves designers and programmers of the problems of synchronizing multiple real-time tasks, thus allowing them to focus their efforts on the applications software itself.

3.2.6.2. APPLICATIONS SOFTWARE

The Rum III Control System attempts to integrate a large number of activities to produce a desired result. In one case, a supervisory computer may coordinate the various parts of the system by monitoring and controlling the actions of many small computers doing local data acquisition or control tasks. The CTP , as supervisory computer uses commands to the local systems to make changes in the activities of those systems and request data from them. It may use the retrieved information to start, stop, and modify a process, detect malfunctions, implement adaptive control, etc. In another situation, the operator may wish to exercise some control over the supervisory computer or take over its functions entirely.

In order to facilitate this schema, the CTP applications software is organized as a set of processes operating in a multitasking environment for efficiency of operation and ease of control. This environment itself may be thought of as containing two separate and distinct environments: Foreground, or Interrupt Environment, and Background, or Non-interrupt environment. Since a real-time system must respond immediately to events occurring in the real-world, the basic function of the foreground program is to send and receive buffered data, while the background program processes the data. Each task that communicates on an interrupt basis is supplied with its own input and output buffers for each channel of communication and the interrupt service routines necessary to process them. Depending on the nature of the information being transmitted, a message can be a single character, a single line, or a string of characters terminated by some special code to indicate end-of-message. The major background tasks may then take advantage of the multitasking facilities available to them, including various scheduling methods, inter-task communication schemes, etc. (see Fig 3.)

The usual method of handling task scheduling involves a time-sliced round-robin scheme combined with some provision for priority for real-time sensitive processes. All tasks remain pended until they are called upon do perform some processing. During this time, various buffers belonging to different channels are being filled on an interrupt basis from external devices or other tasks. When a message is noted as complete, or ready to be sent, the buffer is flagged as ready to be serviced and the task associated with that channel is activated. The task then reads the buffer and processes the data. When the task completes its function it pends itself until another buffer is found to be ready for processing. Using a double buffering scheme, a second buffer associated with that same channel that has been flagged empty may now be filled while the first buffer is being processed.

If a particular process is real-time sensitive, say one that must continually poll a device for output, it may be allowed to run at a higher priority. The effect created is such that the higher priority task is allowed to run continually but must share time with other tasks when they become active.

When more than one task is running at the same time, they share CPU time on a time-sliced basis. This has the effect of smoothing out the appearance of sequential processing.

The basic tasks are:

a) **The Console Command Interpreter. (CCI)**

The CCI is the user-interface between the operator and the Rum III Control System. It accepts input from the Operator CRT and displays formatted output on the screen. As Each line of input is decoded, various functions are performed. The CCI may format and send a message command to a device directly, or it may fill a channel buffer belonging to another task and activate the selected task to do the processing. The CCI is menu driven and will prompt the user at all levels for the proper response. Information about each command and its use is available interactively on line. The user is protected against potentially destructive input, warned, and re-prompted for a selection of proper inputs. In this way, the new user is led by the system to a full understanding of what functions are available to him and their proper use while the more experienced operator has at his disposal a fast memory aid. These functions are especially useful in the field under difficult working conditions where it may not be possible to make effective use of written documentation.

A list of available commands may be found in *Appendix I.*

b) **The Operator Console Task.**

There are two Operator Console Tasks that may be implemented depending on the hardware used in the Operator Console. For those devices that are read on an interrupt basis, the method used for the Operator CRT is used. That is, the task is activated when a buffer related to it is flagged as ready to be processed and is pended when the processing is completed. For those devices that must be continually polled for output, their task is given a higher priority than all other tasks and allowed to run continuously. When other tasks of a lower priority need to be activated, their priorities are raised to that of the Operator Console Task, causing them to run in parallel with it on a time-sliced basis.

Both types of tasks must format the information read from the hardware devices in a way that can be transmitted to both the Operator CRT to provide feedback to the operator on the status of the Operator Console outputs and to the Command and Status Telemetry link for downloading to the VDN.

c) **The Manipulator System Task.**

The Manipulator System includes the Manipulator itself and the Manipulator Boom.

This task is responsible for processing the operators command to, and reading and processing sensor information from the Manipulator System. The processing done by the task is determined by which of five basic control modes for driving the manipulator system is engaged.

The five control modes are:

1) **Operator control of the boom end position.**

In this mode, the operator supplies control input by means of a joystick on the Operator Console or by keyed input at the Operator CRT. The input determines the direction and rate of movement of the manipulator boom tip in r, z, theta coordinates. The desired rate and direction in r and z

coordinates of the command is converted into rates for the three boom joint angles by the boom VPP. An approximate conversion is carried out by use of a stored matrix of conversion vectors, one vector for each of the one foot square access cells. The conversion algorithm constrains the arm in a least mean square error sense to the stored preferred shape defined at the center of each access cell while transitioning along the trajectory.

2) **Operator control of each boom actuator's rate of change.**

In the second control mode, the operator supplies control input by means of The Operator CRT or four rate control switches on the Operator Console which individually control the rates of the manipulator boom hydraulic actuators. In this mode there is no preferred configuration constraint. This mode is useful for moving the boom in unusual ways.

3) **Operator control of each pilot valve.**

This is the "emergency" mode. The operator controls on-off switches which actuate the hydraulic pilot valves. This is the most primative mode useful only for emergency movements should some component malfunction.

4) **Computer control of a pre-programmed movement.**

This control mode is very useful for repetitive tasks. Here, pre-programmed or learned movement sequences are stored in the ship-board computer memory and recalled with a single command by the operator.

5) **Computer control to a given boom end destination.**

Finally, this control mode is a ship-board computer controlled movement in which the operator inputs a command to move to a particular location and the computer calculates and executes the best boom movement to complete the command. The "best boom movement" is software definable.

In all control modes, the computer system is programmed to:

1) Warn or prohibit intended movements into inaccessible or restricted areas.
2) Limit movement of the actuators if necessary to keep movement rates in the proper requested proportion.
3) Stop all movement if unable to move any component as requested.
4) Stop all movement if other RUM III subsystems request it.

d) **The Command and Status Telemetry Link Task.**

This task activates when a buffer sent from the VDN is ready to be processed and when a buffer is ready to be sent to the VDN. It is responsible for distributing the received data to the proper channels and setting up the downloading buffer and initiating interrupt driven output.

e) **The High Speed Telemetry Link Task.**

This task is responsible for sending, receiving, and buffering TV and sonar data being transmitted over the data link.

f) **The Sonar Task.**

The Sonar Task processes input and output buffers in the normal way. It also converts sonar data read to a form that can be displayed and understood more easily by the operator.

g) **The TV Task.**

The operator may select individual TV cameras and may change the following settings:

1) **Focus:** Near, Far.
2) **Zoom:** In, Out.
3) **Pan:** Left, right.
4) **Tilt:** Up, Down.
5) **Scan:** 512, 256, 128 line resolution.

i) **The Thruster System Task.**

This task also treats buffered information in the standard way described above. There are four basic modes of addressing the Thruster System as described below:

1) **Auto Heading.**

The Auto Heading mode may be engaged in parallel with the other modes of operation. The operator instructs the Thruster System to maintain a selected magnetic heading. The task reads the compass status, calculates the needed thruster pitch for each of the two thrusters and sends a formatted command to the Thruster System.

2) **Directional Control.**

The operator selects one of eight directional commands and a power. The calculations are done to produce the proper thruster instructions to create the desired effect and the command is sent to the Thruster System.

The commands are:

a) **Forward.**
b) **Backward.**
c) **Slide Right.**
d) **Slide Left.**
e) **Rotate Right.**
f) **Rotate Left.**

3) **Individual Thruster Control.**

The operator may select an individual thruster and set the direction and power of its thrust.

4) **Individual Rod Control.**

The operator may individually power each of the three Pitch Rods for each of the two Thrusters.

3.3. TELEMETRY INTERFACES

As the RUM III vehicle is designed for a maximum operating depth of 3,300 fathoms, the power and telemetry signal transmission systems must be capable of operating over a 30,000 ft. length of MPL Deep-Tow cable. Two Telemetry systems are provided.

The Command and Status Link provides a two way interprocessor communications link, ship to vehicle and vehicle to ship, capable of accommodating simultaneous two way transmission of binary coded signals at a bit rate of 20 Kbps up cable and 10 Kbps or greater down cable. In addition, a High Speed Data Link transmission system at the highest bit rate consistent with the limited cable bandwidth is provided. Most of the usable cable bandwidth will be occupied by the high speed data transmission signal (approximately 200 Khz to 1.25 Mhz) using a delayed modulation - mark, or "Miller" coded waveform. The down-cable interprocessor link will be a frequency shift modulated (FSM) signal centered at 1.5 Mhz.

In addition to servicing all of the operating-vehicle control and sensor readout requirements, the telemetry systems, through the vehicle and shipboard processors, will provide for controls and sensor readout, processing and data transmission for vehicle user's special instrumentation packages.

3.4. VEHICLE DATA NODE (VDN)

The VDN is a 6502 based microprocessor system dedicated to transferring data between the shipboard CTP through the Command And Status Telemetry Link and the ADLC of each of the VPP's and the VTP contained in the vehicle. As this communications link is vital to the operation of the vehicle, some redundancy is built in to the system. First, two 6502 microprocessors will be used. Each time the system is powered up, a different 6502 is hardware selected. This method has several beneficial effects. Each of the two 6502 systems will be certain to get approximately the same amount of use on a day to day basis bringing any problems to either system quickly to light. Further, if a system failure occurs during a mission, a power down, power up sequence will swap in the second 6502 system without having to abort the mission. In addition, the MC68000 based VTP will contain the necessary software to take over the responsibilities of the VDN in addition to its own functions. This redundancy is useful not only to compensate for complete VDN system failure but, also, to make use of the superior power of the MC68000 if it is found that the 6502 based system is unable to handle the load placed on it.

3.5. VEHICLE PERIPHERAL PROCESSOR'S (VPP'S)

Each VPP will be used to control an electronic or mechanical sub-system and will consist of a 6502 microprocessor, sockets for up to four memory chips, an "Advanced Data Link Controller" (ADLC) for communication with the central control system, and two "Versatile Interface Adaptors" (VIA's) for interfacing to the application-specific hardware.

Most VPP's are housed in cylindrical pressure cases. The case provides room for the VPP circuit board, and for an additional board which can contain circuits required for the specific application. The end cap of the pressure case will accommodate a number of electrical signal penetrators. This will be enough for all the VIA input and output signals, as well as the ADLC and other connections to the central control system. Alternatively, the PIA I/O pins may be connected inside the case to the application board, which would in turn be connected through the endcap to external devices. In a few instances, VPP's will be housed in the larger pressure cases along with other electronics.

The pressure housings are made of high strength 7075-T6 aluminum to reduce weight by minimizing the required wall thickness. The cases are then contained in oil-filled junction boxes or other protective environments to resist sea water corrosion.

Details of the memory configuration for a particular VPP will depend on the application. In every case, a random-access memory (RAM) must be installed in low memory (locations 0000 to 0800 hex) to accommodate the page zero and stack areas required by the 6502 architecture. Similarly, the highest memory (locations F800 to FFFF hex) must be read-only memory (ROM) to include the reset and interrupt vectors (FFFA to FFFF). This ROM also contains the VPP monitor program. The two remaining memory chips may be either RAM or ROM as required by the application.

3.5.1. THRUSTER SYSTEM

The Thruster System is a constant speed, two thruster underwater device that provides for variable thrust in either direction along its axis of rotation and/or variable torque around any line perpendicular to its axis of rotation.

The two thrusters are mounted on the Rum III vehicle turret at an angle of 90 degrees to each other. The turret rotates on ball bearings and is connected to the vehicle by the base. In each thruster, four symmetrical thrust blades are attached to four blade shafts that rotate with the turret. The pitch of the blades is varied by rotating the blade shafts. The positions of three control rods determine the position of a circular follower plate whose orientation determines the thruster blade pitch.

Moving all three control rods together causes translation of the follower plate along the axis of rotation. That, in turn, causes the pitch of the blades to change resulting in thrust. Moving the control rods separately causes the follower plate to tilt, providing a changing pitch of the blades as they rotate. This produces a torque rather than an axial thrust.

By varying the pitch of of each of the four blades of the two thrusters, various combinations of directional thrust and torque may be produced.

3.5.2. MANIPULATOR BOOM

The RUM III manipulator boom and its hydraulic systems are mounted on a rotating turret which provides for azimuthal movement. The boom consists of three articulated arms with the joints rotated by hydraulic linear actuators acting on compound linkage mechanisms.

Movement of the manipulator boom is accomplished by controlling the flow of sea water to one side of a set of hydraulic linear actuators. The actuators are designed to provide push-pull action by either supplying fluid from the 100 psi supply to one side of the cylinder or venting fluid from the same side to the 0 psi sump. The control of the fluid is done by two pilot operated 1 in. control valves. The control valves are actuated with a microprocessor controlled servo loop using flowmeters as sensing elements thereby eliminating any non-linear effects. Solenoid valves supply the pilot fluid to the control valves by metering small amounts of fluid at a relatively rapid rate.

One 6502 microprocessor is dedicated solely to managing the servo loop consisting of flowrate input, flowmeter measurement, and pilot valve control for the four hydraulic linear actuators. A VPP is used to interface with the main RUM III control system.

Control of the boom is initiated at a shipboard control console by the operator. Control signals are transmitted down the tether cable to the vehicle

computer system which in turn sends them to one of the boom microprocessors. Boom sensor information is transmitted back to the shipboard computer by the same system.

The use of microcomputer systems to control the manipulator boom also has the advantage of being able to easily adjust the the control functions to match the complex dynamics of the mechanical system.

3.5.3. SONAR

Four basic sonar systems are considered essential for the initial Rum III Control System:

1) **Top echo, up-looking**: Used to measure depth below surface.
2) **Bottom echo, down-looking**: Used to measure height above bottom.
3) **Side-looking**: Mounted on vehicle turret.
4) **Transponder, navigation**: Take ranges and compute position.

Each system will be controlled by a single VPP and their outputs made available to the ship-board CTP through the data links.

3.5.4. TELEVISION SYSTEM

Two or more TV cameras will be provided. However, only one video signal transmission link will be available. Cameras will be operator selected through the Operator Console or Operator CRT. If the simultaneous viewing of two cameras should be required, a time sharing scheme will be implemented where alternate sweeps, alternate fields or alternate frames are used.

Because standard television scan rates and resolution require a video bandwidth of 3.5 MHz or more, and because the total usable cable bandwidth available to all RUM III signal transmissions is less then 1.5 MHz, considerable compromise must be made in the TV system design.

The transmission scheme involves digitization of the video signal amplitude for each pixel before sending it via the High Speed Telemetry Link. This method allows the transmission of other high-rate data, on a time shared basis, over the same link.

Four bit quantization (16 levels) of the video signal will be performed. This will allow picture cells to be scanned at a 310 KHz maximum rate. It is believed that a picture resolution comparable to RTMA standards (5245 lines/275,625 picture cells) should be available. 512 lines has been chosen. This would allow the generation of a maximum of 262,144 pixels. At the scan rate of 310,000 pixels per second, it will take 0.8456 seconds to complete a full picture scan. This is an extremely low frame rate for viewing anything in motion, but it should be useful for the examination of stationary objects. The system design provides for sacrifice of resolution as a trade-off for more rapid update. The operator will have a choice of three scan modes:

1) **High resolution,slow scan.**

   This will provide 512 line resolution at approximately 1.17 frames/sec.

2) **Medium resolution,medium scan.**

   256 line resolution at 4.69 frames/sec.

3) **Low resolution, fast scan.**

128 line resolution at 18.77 frames/sec.

A scheme called pseudo-random scan will be used to reduce the apparent flicker rate or waterfall effect that one sees when the total picture is simply generated in a sequential series of horizontal sweeps from top to bottom. This method does, however, introduce the appearance of smearing or de-focusing of subjects which are in motion.

There are three paths for data transmission for the TV system. The normal path is a DMA transfer of data to the VTP. In the VTP, information may be processed for more efficient transfer up the High Speed Data Link. The backup mode sends the TV data directly to the High Speed Telemetry Transmitter, bypassing the VTP. A third alternate path involves the use of the Command and Status Link to upload data at a greatly reduced data rate.

The camera design is based around an RCA type 4514 Vidicon. The Vidicon has a 1" diameter envelope and utilizes electrostatic deflection. These two features have made it feasible to package the camera in a 1-1/2 inch inside diameter pressure housing. In addition, this camera features high sensitivity for good low light level performance.

The received picture would be displayed on a medium-to-long, or variable, persistence scope.

3.5.5. ACOUSTIC SENSOR

An acoustic sensor is provided to monitor environmental and mechanical system noise in the immediate vicinity of the Rum III vehicle.

3.6. VEHICLE TELEMETRY PROCESSOR (VTP)

The VTP is a MC68000 microprocessor based system provided with the VRTX real-time executive. It serves several purposes. First, it may be used to implement a bandwidth compression scheme to process video and sonar data for fast transfer up the high speed telemetry link to the CTP. Secondly, it may provide more powerful processing capabilities for various VPP's that may be overloaded in their tasks. This will allow a reduction in the number of messages sent over the data link. Further, it can provide for some system redundancy by serving as a back-up processor for the VDN should it fail.

4. SENSOR SYSTEMS

All sensor outputs will be 50 mv standard level. They will be multiplexed differential amplifier input. Power will be measured by voltage and current shunts. There will be 64 sensor signal channels and sensor information will be updated at a 60 Hz rate.

The following sensors are considered essential to the Rum III control system:

1) **Navigation:**
   a) **Compass**: A gimbaled Digicourse.
   b) **Transponder**: For range taking and navigation.

2) **Search and Object Location:**
   a) **Side-looking sonar**: Mounted on turret.

b) **TV**: Two cameras provided.

3) **Handling**:
   a) **Vertical echo sounder**: Up-looking for depth below surface.
   b) **Vertical echo sounder**: Down-looking for height above bottom.

4) **Vehicle Status**:
   a) **Pitch**: Measured by pots.
   b) **Roll**: Measured by pots.
   c) **Thruster pitch**: Measured by pots.
   d) **Manipulator angle sensors**: Measured by internal acoustics or pots.
   e) **Accumulator extension**: A multiturn pot.
   f) **Cable side force**: Strain gages.
   g) **Environmental noise**: Acoustic sensor.
   h) **Electrical voltage and power** (2):Appropriate devices.

ACKNOWLEDGEMENTS

This work was sponsored by the Naval Ocean Research and Development Activity Contract N00014-79-C-0983 and the Naval Ocean Systems Center.

APPENDIX I

Summary of Rum III System Commands

1) <"help">	<"help">				Print this menu.
	<"thrust">				Print thruster menu.
	<"tv">				Print TV menu.
	<"manip">				Print manipulator menu.
	<"tele">				Print telemetry menu.
	<"console">				Print console menu.
	<"sonar">				Print sonar menu.
	<"sensor">				Print sensor menu.
2) <"boom">	<"manu">	<#>			Execute pre-programmed maneuver "#".
	<"switch">	<#>	<rate>		Set control rate switch "#" "0-MAX".
	<"valve">	<#>	<"on">		Pilot valve "#" on.
			<"off">		Pilot valve "#" off.
	<"move">	<r>	<z>	<Θ>	Move boom to position "r,z,Θ".
	<"stop">				Stop all manipulator boom motion.
3) <"head">	<deg>				Maintain heading "0-360 deg".
4) <"veh">	<"for">	<pwr>			Vehicle forward "0-MAX".
	<"bac">	<pwr>			Vehicle backward "0-MAX".
	<"sta">	<pwr>			Vehicle slide starboard "0-MAX".
	<"prt">	<pwr>			Vehicle slide port "0-MAX".
	<"lft">	<pwr>			Vehicle rotate left "0-MAX".
	<"rht">	<pwr>			Vehicle rotate right "0-MAX".
	<"stop">				Stop thrusters.
5) <"thrus">	<#>	<"f">	<pwr>		Set thruster "#" forward "0-MAX".
		<"b">	<pwr>		Set thruster "#" back "0-MAX"
		<"s">			Stop thruster "#"
6) <"rod">	<#>	<"i">			Move pitch rod "#" in.
		<"o">			Move pitch rod "#" out.
		<"s">			Stop pitch rod "#".
7) <"tv">	<#>	<"on">			Turn camera "#" on.
		<"off">			Turn camera "#" off.
		<"focus">	<"i">		Focus in.
			<"o">		Focus out.
		<"zoom">	<"i">		Zoom in.
			<"o">		Zoom out.
		<"pan">	<"r">		Pan right.
			<"l">		pan left.
		<"tilt">	<"d">		Tilt down.
			<"u">		Tilt up.
		<"scan">	<n>		Scanrate at "512", "256", "128"..
8) <"acc">	<"on">				Turn acoustic sensor on.
	<"off">				Turn acoustic sensor off.

RUM III Control System

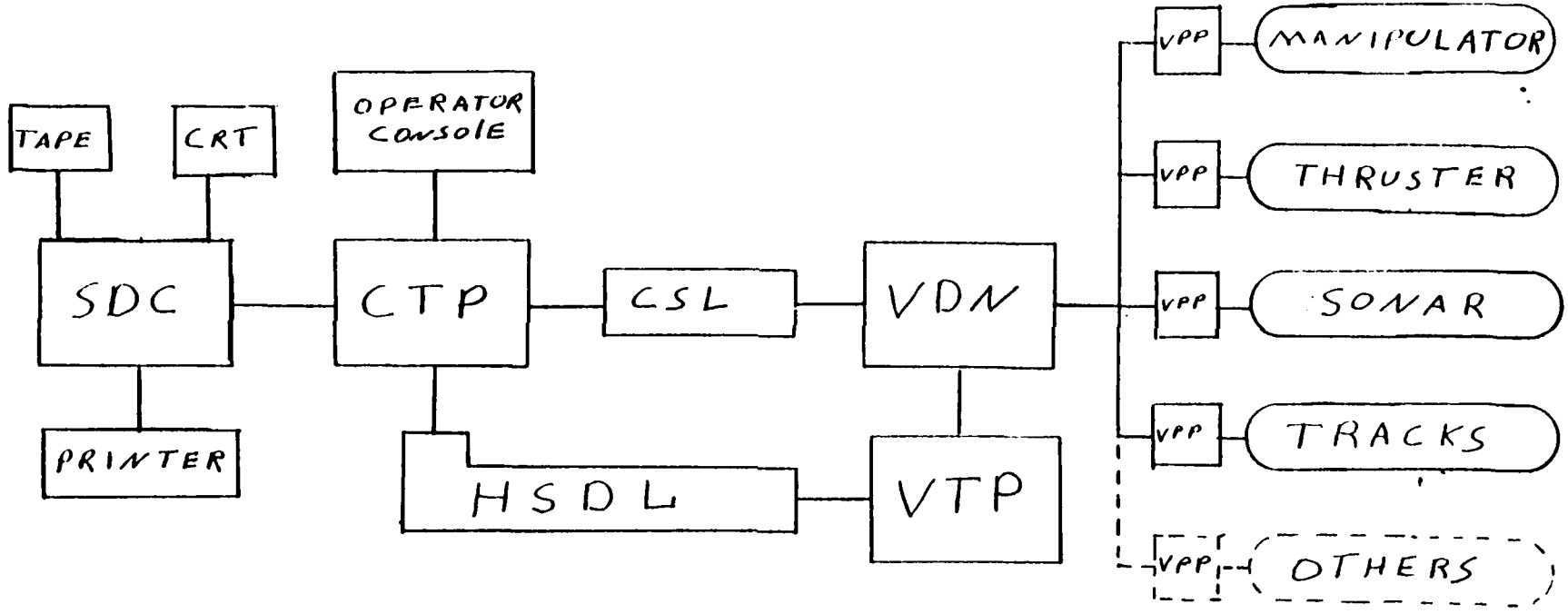

Fig 1

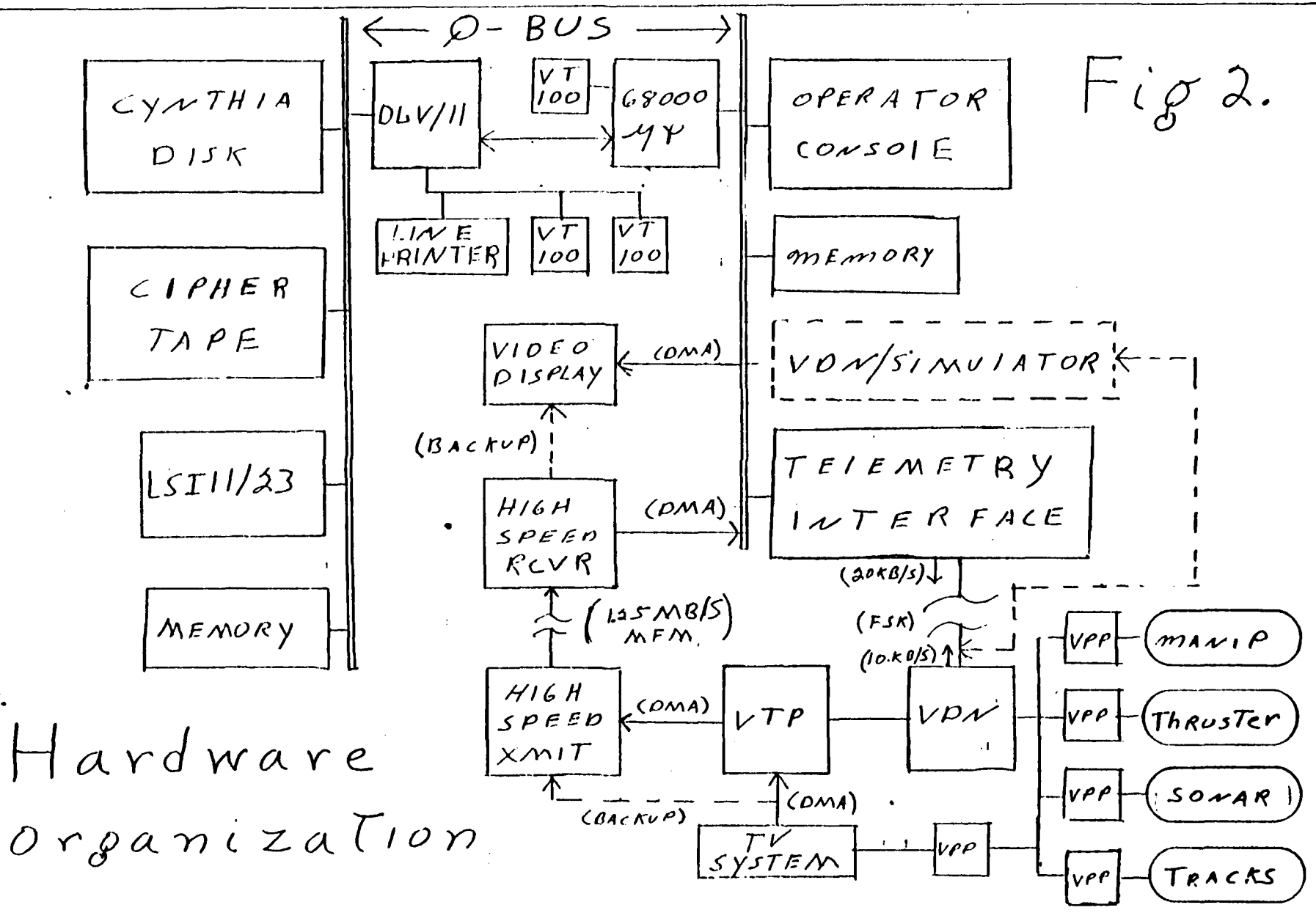

Fig 2.

Hardware Organization

CTP
SOFTWARE
SYSTEM

Fig 3

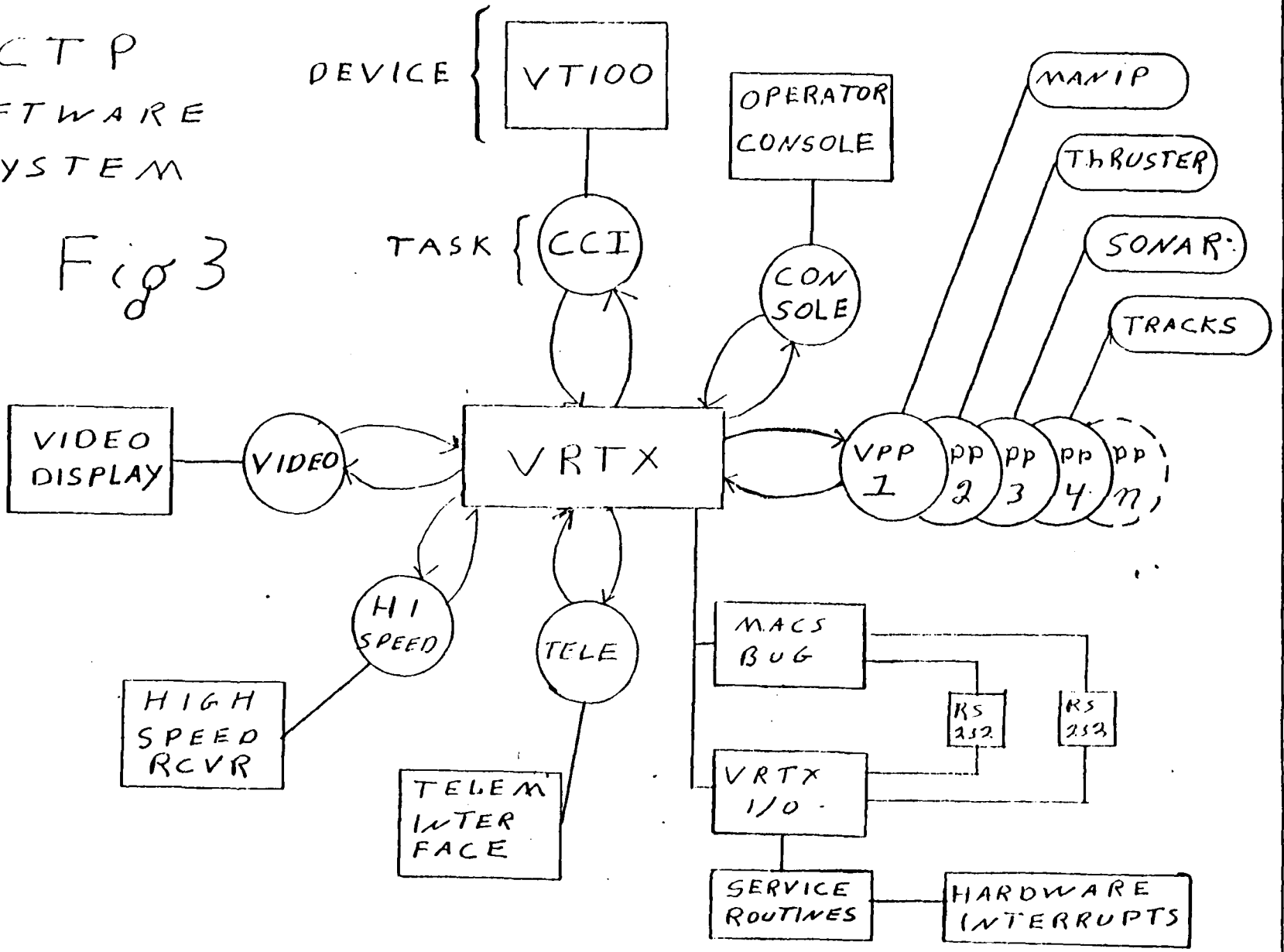

III. SIDE LOOKING SONAR FOR AUSS

Principal Investigator: Robert C. Tyce
Total Amount of Award: $126,000

1. In July 1982, an RCP was written to amend the above referenced contract for a task to the Marine Physics Laboratory of Scripps Institute of Oceanography (MPL/SIO) for providing a sonar system for use on the Advanced Unmanned Search System (AUSS) Testbed Program. The principal investigator at MPL/SIO was Dr. Bob Tyce, and Ken Collins was the primary contact at NOSC because he was the project engineer on the AUSS vehicle program. The AUSS program had recently added the requirement for a high resolution side looking sonar system; so, it seemed logical to draw upon the search sonar expertise that had been developed at MPL/SIO under the guidance of Dr. Fred Speiss. The total commitment of $120,000.00 was to pay for engineering, procurement, assembly, checkout, and testing of a pair of side looking sonars to be integrated into the AUSS Testbed.

2. Many meetings were held with Dr. Tyce, Mr. Collins, and others. After comparing many alternatives, including the possibility of building our own narrow beam transducers, a hybrid system was agreed upon and pursued. The system that was finally delivered to NOSC uses 2 ea. 3/4 degree beam 100 KHz. transducers and transmit/receive electronics which were manufactured by Edo Western Corporation. NOSC built the digitizing electronics which interfaced them to our vehicle computers and acoustic communication link. The surface display screens were incorporated into the existing hardware of our control consoles with the software being done by Systems Exploration Inc. who had done all of our other surface display software development. We are pleased with how the sonar system integrated together with the rest of the vehicle and some prelimianry testing has been completed. Delays in other phases of the AUSS program have prevented us from using the MPL/SIO sonar system in the search mode, but we plan to do that this fiscal year. NOSC is satisfied with the work completed and the hardware delivered under this task.

IV. BOOM SUPPORT

Principal Investigator: Kenneth M. Watson
Total Amount of Award: $48,100

In support of an ocean optics measurement project conducted by NOSC personnel aboard the research platform FLIP, MPL modified and installed two aluminum truss booms (60 ft and 75 feet) from which the oceanographic instrumentation was suspended, resulting in successful data acquisition.

DISTRIBUTION LIST

OPERATIONS RESEARCH, INC
ATTN: DR. THOMAS BELL
1375 PICCARD DR
ROCKVILLE, MD 20850

COMMANDING OFFICER
NAVAL OCEAN RESEARCH AND DEVELOPMENT ACTIVITY
CODE 331 (ATTN: DR. RUDOLPH HOLLMAN)
NATIONAL SPACE TECHNOLOGY LABORATORIES
NSTL, MS 39529

COMMANDING OFFICER
NAVAL OCEAN RESEARCH AND DEVELOPMENT ACTIVITY
CODE 342 (ATTN: MR. K. M. FERER)
NATIONAL SPACE TECHNOLOGY LABORATORIES
NSTL, MS 39529

DIRECTOR
OFFICE OF NAVAL RESEARCH
CODE 422PO (ATTN: DR. T. SPENCE)
800 NORTH QUINCY STREET
ARLINGTON, VA 22217

DIRECTOR
OFFICE OF NAVAL RESEARCH
OCEAN SCIENCE AND TECHNOLOGY DIVISION
CODE 422PO (ATTN: LCDR ROBERT WILLEMS)
NATIONAL SPACE TECHNOLOGY LABORATORIES
NSTL, MS 39529

COMMANDING OFFICER
NAVAL RESEARCH LABORATORY
CODE 5810 (ATTN: MR. E. RUDD)
4555 OVERLOOK AVENUE, SW
WASHINGTON, DC 20375

APPLIED PHYSICS LABORATORY
UNIVERSITY OF WASHINGTON
ATTN: DR. MICHAEL C. GREGG
1013 NORTHEAST 40TH STREET
SEATTLE, WA 98195

JOHNS HOPKINS UNIVERSITY
DEPARTMENT OF CHEMICAL ENGINEERING
ATTN: MR. MICHAEL KARWEIT
34TH AND CHARLES STREETS
BALTIMORE, MD 21218

CHIEF OF NAVAL OPERATIONS
OP-21T3 (MR. RICHARD LAUER)
DEPARTMENT OF THE NAVY
WASHINGTON, DC 20350

COMMANDING OFFICER
NAVAL OCEAN RESEARCH & DEVELOPMENT ACTIVITY
CODE 500 (ATTEN: DR. MIKE STANLEY)
NATIONAL SPACE TECHNOLOGIES LABORATORIES
NSTL, MS 39529

ONR BRANCH OFFICE
1030 EAST GREEN STREET
PASADENA, CA 91106

NAVAL RESEARCH LABORATORY
DEPARTMENT OF THE NAVY
CODE 2627
WASHINGTON, D.C. 20375

DEFENSE DOCUMENTATION CENTER
BLDG. 5
CAMERON STATION
ALEXANDRIA, VA 22314

END

FILMED

6-85

DTIC